Investigation of Spectral Baseline Properties of the Green Bank Telescope
Electronics Division Internal Report No. 312

J. R. Fisher, R. D. Norrod, D. S. Balser

September 2, 2003

Contents

1 Introduction

One of the primary motivations for the off-axis design of the Green Bank Telescope (GBT) was to reduce the effects of multi-path interference, often referred to as standing waves, between the feed, subreflector, and main reflector of the antenna. This interference causes low-level ripples in the frequency dependence of the gain of the antenna, which can mask weak spectral lines in the presence of continuum radiation from the spectral line source. Reflections in the antenna structure can also introduce frequency dependence of the total system noise which may not completely cancel in on-source/off-source spectral differences or may show up as second-order effects in the calibration arithmetic. With an off-axis paraboloid the specular reflection areas that cause the strongest gain and noise ripple are at the inner edge of the dish and subreflector where feed illumination is relatively low. Hence, the effects of these reflections should be correspondingly lower.

As will be shown in this report, reflections within the antenna are not the only source of spectral baseline distortions. To realize the full potential of the GBT design care must be taken to minimize the effects of transmission line and waveguide reflections, amplifier and filter instability, data sampling quantization, and other more subtle sources of spectrum distortion. The investigation described here focused on separating the various effects as a guide to engineering improvements and calibration techniques that will follow.

Because of the claims of better baselines with an off-axis telescope it is natural to compare GBT results with spectra from symmetric antennas. Since we do not have much directly corresponding data from other telescopes, these comparisons must be largely anecdotal. In making these mental comparisons from your own experience keep in mind a few factors. First, the bandwidths of most of the spectra shown here are considerably wider than have been used at centimeter wavelengths in the past. Second, the reflection distances in a 100-meter antenna makes the corresponding ripple periods of multi-path interference smaller than have been seen on smaller telescopes. Third, the spectra shown here were specifically designed to emphasize spectral baseline distortions so they are not necessarily representative of spectra that one would experience under typical observing conditions.

Most of the spectra to follow are $(on - off)/off$ vector differences and quotients, where the normal assumptions are that the only difference between the on and off spectra is the effect being measured and that the frequency dependence of the system gain is normalized by dividing by the system noise spectrum. Spectral baseline distortions are largely due to one or both of these assumptions being incorrect. Equation 1 is a partial separation of the gain and noise terms in the $(on - off)/off$ vector, keeping the assumption that the only difference between the on and off spectra is the injection of the continuum radio source power, $P_{src}(f)$.

$$\frac{on - off}{off} = \frac{G_{src}(f)P_{src}(f)}{G_1(f)P_{bknd}(f) + G_2(f)P_{spill}(f) + G_3(f)P_{wg}(f) + G_4(f)P_{LNA}(f)} \tag{1}$$

The noise spectra of the radio source, $P_{src}(f)$, background, $P_{bknd}(f)$, and spillover, $P_{spill}(f)$, are only weakly frequency dependent, but the waveguide ohmic loss noise, $P_{wg}(f)$, and amplifier noise, $P_{LNA}(f)$, probably have a moderate to strong frequency dependence. Likewise, the gains of the system to the radio source and background noise, $G_{src}(f)$ and $G_1(f)$, are probably nearly equal, but the frequency dependence of the gains to spillover, $G_2(f)$, waveguide, $G_3(f)$, and amplifier, $G_4(f)$, noise are significantly different since they only partially share signal paths. Hence, the off spectrum, which is the denominator of Equation 1, will not be simply proportional to the system gain to the radio source, $G_{src}(f)$.

1.1 System Description

Typically, five to nine cryogenic receiver front-ends are installed on the GBT and available for use. All of the current front-ends are built around HFET amplifiers cooled to 15 Kelvin by closed-cycle refrigerators, and, depending on the frequency range, have one, two, or four feed horns. Each feed horn is followed by a dual-polarized receiver with two independent channels, so the existing front-ends have two to eight channels. A common IF system has eight channels and microwave switches to handle the changes in connections required when a particular receiver is selected and facilities to frequency convert the front-end signals to appropriate ranges for digitization. Figure 1 shows a very simplified block diagram of a receiver channel and critical portions of the common IF system. In this figure, components to the left of the fiber are located on the GBT feed arm; items to the right are located in the Equipment Room in the Jansky Lab. Following is a brief description of each component of this diagram.

Feed Horn Above 600MHz all the GBT feed horns are circular corrugated horns. Below 4GHz these feeds are fabricated using a "hoop-and-washer" technique. The corrugations are formed by stacking hoops and washers under pressure and then spot-welds are used to hold the assembly together followed by the addition of a fiberglass shell for stiffness. Above 4GHz the feed horns are machined from aluminum in sections eight to ten inches long containing several corrugations per section.

Front-end Electronics Following the cryogenic amplifiers, each channel is frequency converted to a first IF center frequency of 1080, 3000, or 6000MHz. The first LO (LO1) is used for doppler tracking and frequency switching if desired. The mixer is followed by IF amplifiers and filters.

IF Router The switch symbol between the front-end and the Optical Driver Module in Figure 1 represents a group of microwave PIN diode switches that select one of several possible inputs to each common IF channel.

Noise Source The IF Rack Noise Source consists of a solid-state diode noise source, amplifier, and filters and may be selected by the IF Router as an input to any of the eight Optical Driver Modules. The Noise Source Module includes a four-way splitter that allows the source to drive four IF channels simultaneously.

Optical Driver The Optical Driver Module (ODM) includes amplifiers, a filter bank for selection of the IF bandwidth, an equalizer, and a total-power detector and V/F converter with fiber connection (not shown) to the Digital Continuum Back-End (DCR). The ODM's cover 1-8GHz, but the user may select one of several more narrow bandwidths centered at either 3000 or 6000MHz.

Laser Modulator The ODM IF coaxial output is connected to a Laser Modulator which intensity modulates a laser output connected to a single-mode optical fiber.

IF Fiber The IF single-mode optical fiber is approximately 2.3km long, connecting the feed arm Receiver Room to the Equipment Room in the Jansky Lab. Fusion splices are used throughout to eliminate instabilities typically seen with fiber connectors.

Optical Receiver In the Optical Receiver Module, the laser signal is demodulated using a photodiode detector. A microwave amplifier and four-way power splitter follow the photodiode providing four identical outputs of the first IF signal in the Equipment Room.

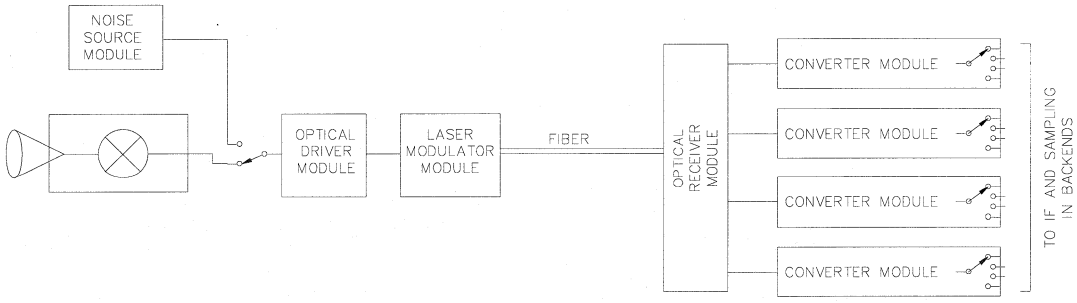

Figure 1: A simplified block diagram of one GBT receiver channel and associated IF electronics.

Converter Module Each Optical Receiver output is connected to a Converter Module (CM) which uses a two-step conversion scheme to supply signals with high image rejection to any of several back-ends. The input 1-8GHz IF signal is up-converted to the 9.0-10.35GHz range, and then down-converted to the 150-1600MHz range. The various CM outputs connect to the IF input systems of the Spectral Processor, VLBI Data Acquisition Rack, Autocorrelation Spectrometer, or other back-ends.

2 Antenna Noise

2.1 L-band (1.4 GHz) measurements

Early in our investigations we were puzzled by a baseline ripple in frequency-switched data near 1.4 GHz with a ripple period of about 1.6 MHz. It evidently had something to do with the antenna because the phase of the ripple changed with subreflector position, and the phase changed by half of a period with an 1/8-wavelength shift in the subreflector toward the main dish. This ripple period showed up again in later total power measurements where the blank sky *on* and off spectra differed only by a displacement of the subreflector.

Figure 2 shows 50-MHz bandwidth difference spectra near 1.4 GHz for the two linear receiver polarizations at 1/8- and 1/4-wavelength subreflector displacements between the *on* and off spectra. Several notable features can be seen in these spectra. First, there are quasi-sinusoidal ripples with periods of about 1.6 and 9 MHz. Second, the 1.6-MHz amplitude is strongest in the 1/8-wavelength subreflector displacement spectra, and the 9-MHz amplitude is strongest in the

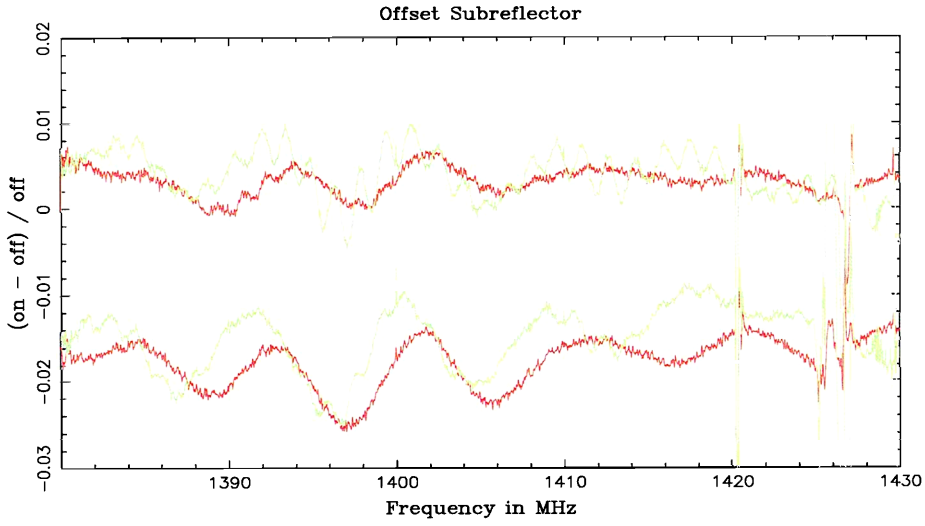

Figure 2: Cold sky (on - off) / off spectra at an elevation of 80 degrees, where 'off' is with the subreflector in its nominal focus position and 'on' is with the subreflector displaced in the +Y direction (roughly toward the center of the main reflector). The red or darker curves are for receiver channel X and the green, lighter curves are for channel Y. The top curves are with 1/8-wavelength (26.7mm) displacement and the bottom curves are with 1/4-wavelength (53.3mm) displacement. The bottom curves are offset by -0.02 in the vertical direction to separate the plots.

1/4-wavelength displacement spectra. Third, the 1.6-MHz ripple amplitude is highest in the Y linear polarization whose E-vector is parallel of the plane of symmetry of the telescope.

The waviness in the spectra in Figure 2 is a frequency dependence in the noise power entering the receiver feed and has something to do with the position of the subreflector with respect to the rest of the optics. Another clue to the origins of the spectral ripples can be found in Figure 3, which shows periodograms generated by taking the Fourier transform of the spectra in Figure 2 after removing the RFI and 1420.4–MHz radiation from Galactic hydrogen. The period of the 1.6-MHz ripple is spread over a range of periods from about 1.3 to 1.8 MHz. If we assume that this ripple is due to multipath interference, the path length difference ranges from about 165 to 220 meters (300 meters divided by the ripple period in MHz), which is roughly the range of twice the distance from the Gregorian feed to the main reflector via the subreflector. The GBT reflector geometry is shown in Figure 4. This leads us to the conclusion that part of the noise in the telescope system (cosmic background, atmosphere, spillover, or receiver/waveguide noise) enters the receiver through two paths: directly and after emission or reflection from the feed area and then scattered from the circumferential gaps between the surface panels. Since these gaps run along lines of constant phase as seen from the feed, their scattered waves are coherent at the feed. We expect the scattering to be strongest in the linear polarization perpendicular to the gap length (channel Y), which is what is observed. Also, since this multipath involves two extra reflections from the subreflector, the ripple amplitude measured with this techniques should be strongest for odd multiples of 1/8-wavelength. This, too is consistent with the measurements.

The strongest periodogram features in Figure 3 at about 9 MHz period are suggestive of a multipath distance difference of about 30 meters, which is twice the distance from the feed to the

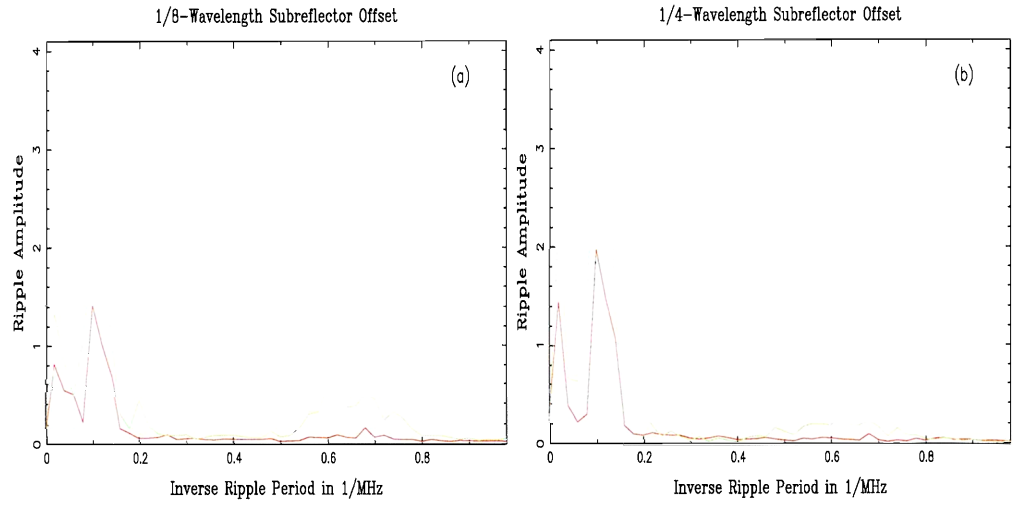

Figure 3: Averaged periodograms of several 1/8-wavelength displacement spectra like those in Figure 2. The red or darker lines are receiver channel X, and the green, lighter lines are channel Y. The vertical scale is roughly the ripple rms amplitude in units of 0.001 of the system noise power density (fraction of Tsys).

Table 1: Periodogram integrals in the inverse ripple period ranges of 0.6 to 0.84 and 0.1 to 0.12 for the 1.4 GHz data.

			Periodogram Integrals		
Elevation	sec(z)	Total Power	1.6-MHz(Y)	9-MHz(X)	9-MHz(Y)
80.0	1.02	1.00	4.59	4.09	5.53
14.5	4.00	1.25	4.44	6.93	10.56
9.5	6.06	1.46	5.48	4.11	13.23

subreflector. (See Figure 4.) Some of the noise in the antenna system is returned directly to the feed after one reflection off the subreflector. This is consistent with the 9-MHz ripple component being strongest in the 1/4-wavelength subreflector offset spectra. There is a hint in Figure 3 that this reflection is partially resolved into more than one path-length component, which will be shown in more detail in measurements with wider bandwidths described below.

To determine whether the noise that is causing the 9- and 1.6-MHz ripples is entering the system in the vicinity of the main beam (cosmic background and atmosphere) we measured the ripple amplitudes at three telescope elevations of 80, 14.5, and 9.5 degrees to vary the amount of atmospheric noise seen by the main beam and near sidelobes. These elevations correspond to air masses of 1, 4, and 6, which would add about 1.5, 6, and 9 Kelvins of noise to the system, respectively. Table 1 shows these measurement results, which are the periodogram integrals in the inverse ripple period ranges of 0.6 to 0.84 and 0.1 to 0.12 (distance ranges of 87 to 123 and 15 to 18 meters) as a function of telescope elevation. The integrals are corrected for rising system temperature with sec(z) so that the values are proportional to temperature, not the ratio to system noise power. The 1.6-MHz ripple amplitude does not appear to be dependent on

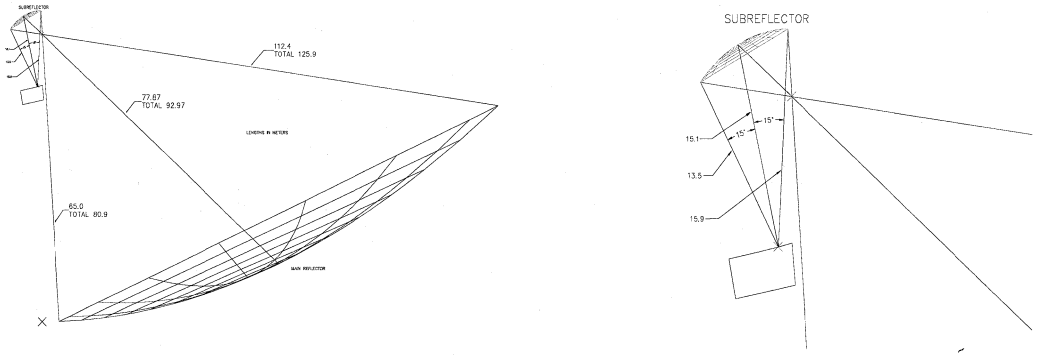

Figure 4: GBT reflector geometry. The distances from the feed phase center to the main reflector via the subreflector are 80.9 and 125.9 meters for the inner and outer edges, respectively. The distances to the inner and outer edges of the subreflector from the feed phase center are 15.9 and 13.5 meters, respectively.

elevation so we tentatively conclude that the noise engaged in this multipath interference is not entering through the the forward direction of the GBT. Channel Y (polarization perpendicular to plane of symmetry) shows a strong elevation dependence in the 9-MHz ripple, but channel X does not. These measurements may be confused by the superposition of several multipaths that are only partially resolved at the distance of 15 meters. The distance between the feed and subreflector changes on the order of 15 centimeters due to focus tracking as the telescope moves from zenith to horizon so the multipath interference patterns are expected to change somewhat.

Noise components in the antenna system that are not expected to change significantly with telescope elevation are due to thermal losses in the feed/OMT/LNA and rearward main reflector spillover. Each of these is estimated to be about 5 K as seen by the LNA, but the edges of the feed and surrounding structure is bathed in noise at somewhat higher temperature due to spillover. The feed is designed to reject most of this noise, but it is there, nevertheless. It is this off-center spillover noise radiation that is reflected back into the GBT optics and interferes with the directly-received spillover noise in the feed. Hence, when computing the return loss required to produce the ripple amplitude observed one may need to assume a somewhat higher reflected spillover noise component. Without a physical optics analysis of the spillover radiation we can only guess at the amplitude of this component, but some rough calculations are instructive.

To estimate the magnitude of the reflection coefficient from the panel gaps required to produce the measured 1.6-MHz ripple, let P_0 be the power directly entering the feed and P_R be the coherent power transmitted or reflected into the optics. Since we will be computing power ratios we can normalize to an impedance of one ohm and take the electric field amplitudes as

$$V_0 = \sqrt{P_0}, \quad V_R = \sqrt{P_R} \tag{2}$$

Let L, in dB, be the return loss of the power, P_R, scattered back into the feed, and let ρ be the equivalent voltage reflection coefficient.

$$L = -10\ log_{10}\ (\rho^2) \tag{3}$$

The measured relative powers at the peak and trough of the baseline ripple will then be

$$\frac{P_+}{P_0} = \frac{(V_0 + \rho V_R)^2}{{V_0}^2} \approx 1 + \frac{2\rho V_R}{V_0} \tag{4}$$

and

$$\frac{P_-}{P_0} = \frac{(V_0 - \rho V_R)^2}{{V_0}^2} \approx 1 - \frac{2\rho V_R}{V_0} \tag{5}$$

The relative peak-to-peak and rms ripple amplitudes will then be

$$\frac{P_{p-p}}{P_0} = \frac{P_+ - P_-}{P_0} = \frac{4\rho V_R}{V_0} \tag{6}$$

and

$$\frac{P_{rms}}{P_0} = \frac{P_{p-p}}{2\sqrt{2}\ P_0} = \frac{\sqrt{2}\ \rho\ V_R}{V_0} \tag{7}$$

Let's assume that the noise due to ohmic losses in the feed and waveguide components is transmitted coherently in both directions, toward the LNA and toward the antenna reflectors. Assume, too, that its temperature is 5 K and that the system temperature is 20 K. In the notation of the equations above, $P_{sys} = 4\ P_R = 4\ P_0$ and $V_R = V_0 = \sqrt{P_0}$. Then, from Equation 7

$$\rho = 2\sqrt{2}\frac{P_{rms}}{P_{sys}} \tag{8}$$

From Figure 3a we see that the highest 1.6-MHz ripple component for the polarization perpendicular to the circumferential panel gaps is about $0.001 \times P_{sys}$, but this is twice the value of P_{rms}/P_{sys} given in Equation 8 since two ripple patterns with a 1/2-wavelength shift were subtracted. Hence,

$$\rho \approx 2\sqrt{2} \times 0.0005 = 1.4 \times 10^{-3} \tag{9}$$

and

$$L = 57dB \tag{10}$$

For the linear polarization that is largely parallel to the panel gaps the highest rms ripple amplitude shown in Figure 3a is only about $0.0001 \times P_{sys}$, which corresponds to a return loss of about 77 dB. The return losses computed from the highest 9-MHz ripple amplitudes seen in Figure 3b are about 45 and 51 dB for the polarizations parallel and perpendicular to the telescope's plane of symmetry, respectively.

In a memo dated February 6, 2001 Norrod and Stennes report on reflectometry measurements of the GBT through the L-band feed. At the distance of the subreflector they measured return losses of about 57 and 60 dB for the linear polarizations parallel and perpendicular to the plane of symmetry, respectively. These values are 12 and 9 dB higher than derived in the calculations above, which would indicate that there is more noise being injected into the multipath interference than the 5 K assumed. This may argue that spillover has a significant role in producing the 9-MHz baseline ripple. The reflectometry measurements resolved the returned power into two or three components separated by as much as 1.6 meters in one-way distance. This and the partial resolution of the 0.1/MHz feature in the periodograms suggest that several reflections from the subreflector are mixed together in the 9-MHz period baseline ripples.

At the distance range of the main reflector Norrod and Stennes measured a return loss lower limit of 83 dB for the perpendicular polarization, which is close to the value of 77 dB from the ripple amplitude calculations. Unfortunately, they did not make a measurement in the polarization parallel to the plane of symmetry, which, in retrospect, would make a better comparison with the 1.6-MHz ripple results.

Table 2: Periodogram integrals in the inverse ripple period ranges of 0.56 to 0.75 and 0.095 to 0.115 for the 5-GHz data.

			Periodogram Integrals		
Elevation	sec(z)	Total Power	1.6-MHz(Y)	9-MHz(X)	9-MHz(Y)
65	1.1	1.00	1.08	0.24	1.16
11	5.2	1.32	0.42	0.65	0.72
6	9.6	1.65	0.83	0.95	1.18

2.2 C-band (5 GHz) measurements

Figure 5 shows wider, 200-MHz bandwidth spectra taken at 5 GHz with the same displaced subreflector differencing technique used to generate the 50-MHz bandwidth spectra at 1.4 GHz in Figure 2. The Y channel, whose linear polarization is parallel to the telescope plane of symmetry, in Figure 5 again shows the stronger 9- and 1.6-MHz ripples. The periodograms of these spectra are shown in Figure 6. The highest ripple components in the periodograms have P_{rms}/P_{sys} values of about 0.0005 and 0.0001 (which are twice the actual values because of the subtraction technique) at inverse periods near 0.11 and 0.6/MHz, respectively. Using the same assumptions of $P_{sys} = 4\ P_R = 4\ P_0$ that we used at L-band and Equations 8 and 3 we compute return losses of 63 and 77 dB, respectively, for channel Y. These losses are 18 and 26 dB higher than the corresponding values found at 1.4 GHz.

The reflection from the subreflector that causes the 9-MHz ripple period is a combination of an edge diffraction and a near-specular reflection from the area of the subreflector close to the parent ellipsoid's primary axis where the surface is almost normal to the line of sight from the feed. The return loss from specular reflection is expected to change roughly as wavelength squared, or about 11 dB from 1.4 to 5 GHz. A more detailed physical optics computation would be required to account for the full 18 dB difference.

The 26 dB difference in the panel gap return loss between the two frequencies is more complicated. One might expect the effective scattering area of the gaps to change roughly linearly with wavelength since the current interruption is in one dimension. This would suggest only a 5 dB difference. We are left to speculate that the rest of the difference may be due to the fact that the gap reflections are more resolved in distance with the larger bandwidth used at 5 GHz (hence, the reflected power is spread over more components), and that the coherence of the reflections over the full circumferential gap extents may be partially reduced by optics misalignments, which would have a larger effect at the shorter wavelength. Part of the difference might also be attributed to lower subreflector diffraction at the higher frequency which would inject less spillover noise into the multipath interference.

One notable feature of the periodogram in Figure 6b is that the longer period ripple at an inverse period near 0.1/MHz has clearly been resolved into a number of components. Channel Y appears to have one strongest component which channel X does not.

Table 2 shows the results of integrating the reflected power over the two ranges of the periodograms that show strong ripple amplitudes. This time the 9-MHz ripple in channel X shows an increase in amplitude with decreasing telescope elevation, but the other two integral ranges do not show this trend. In the 1.4-GHz data it was channel Y that showed the increase in 9-MHz ripple amplitude at lower elevation. It seems likely that the changes in integrated ripple amplitudes are largely due to factors other than the amount of noise entering the system in the forward direction of the GBT.

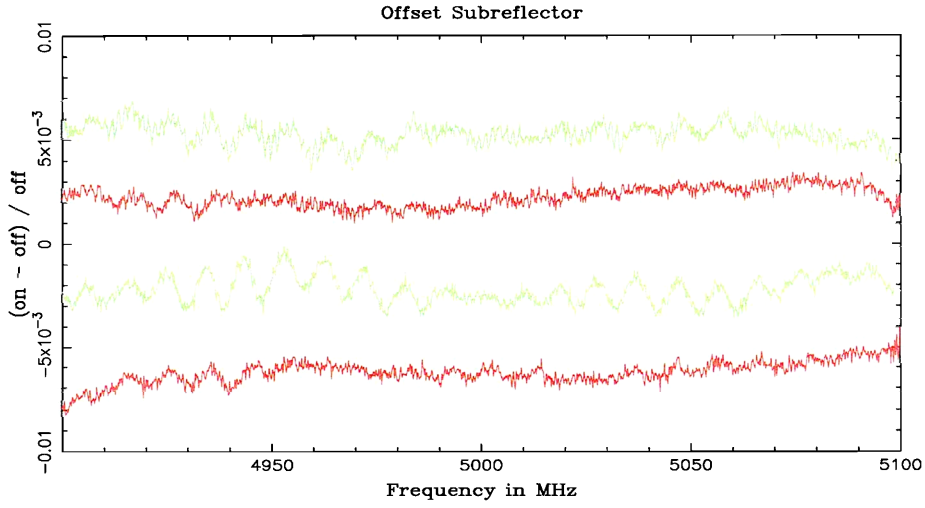

Figure 5: Cold sky (on - off) / off spectra at an elevation of 65 degrees, where 'off' is with the subreflector in its nominal focus position and 'on' is with the subreflector displaced in the +Y direction. The red or darker curves are for receiver channel X and the green, lighter curves are for channel Y. The top curves are with 1/8-wavelength (7.62mm) displacement and the bottom curves are with 1/4-wavelength (15.2mm) displacement.

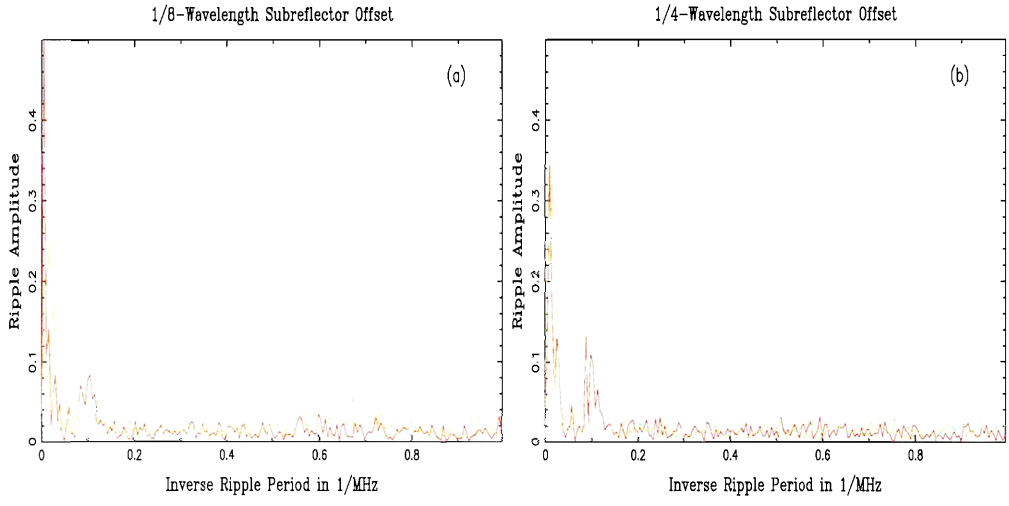

Figure 6: Periodograms of the 1/8-wavelength (a) and 1/4-wavelength (b) displacement spectra like those in Figure 5. The red or darker lines are receiver channel X, and the green, lighter lines are channel Y. The vertical scale is roughly the ripple rms amplitude in units of 0.001 of the system noise power density (fraction of Tsys).

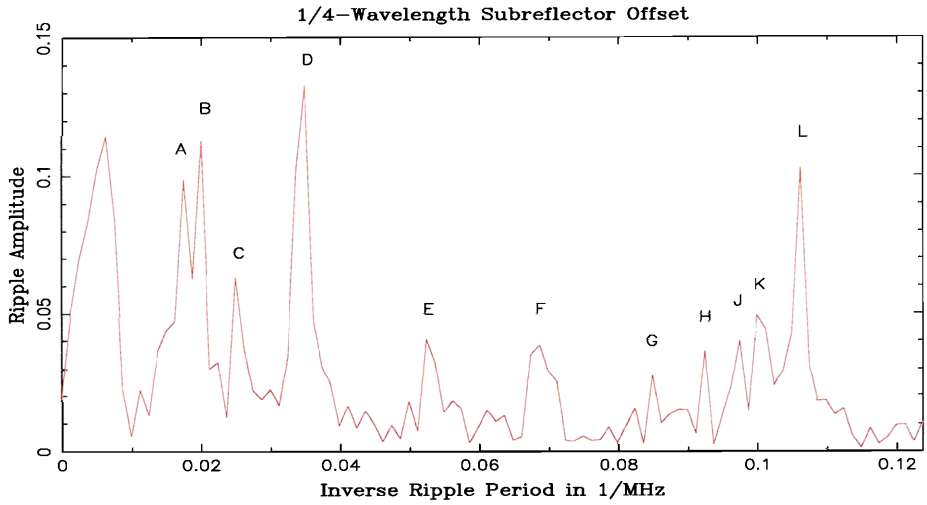

Figure 7: Periodogram of the 1/4-wavelength displacement spectra on cold sky at 9 GHz with an 800-MHz bandwidth. The vertical scale is roughly the ripple rms amplitude in units of 0.001 of the system noise power density (fraction of Tsys).

2.3 X-band (9 GHz) measurements

The same displaced-subreflector measurements were made at 9 GHz with a spectrometer bandwidth of 800 MHz. At this frequency the 1.6-MHz ripple was too weak to make useful measurements, but the wider bandwidth provided very good resolution on the reflections at the distance of the subreflector. Figure 7 shows the periodogram of the 1/4-wavelength displacement $(on - off)/off$ spectrum from circularly polarized channel X for ripple periods greater than about 8.2 MHz. Quite a few sharp features can be seen with this higher ripple period resolution.

Table 3 lists the periodogram features labeled in Figure 7 with their measured location and corresponding ripple period and the path length difference required in multipath interference to cause that ripple period. Figure 8 shows the Gregorian subreflector and feed geometry at the orientation that it has with the telescope pointed near the horizon. The X-band feed is shown at the secondary focus used in the measurement of the periodogram of Figure 7. The L-band feed seems to shadow the X-band feed in this drawing, but this is only the appearance in profile. F1 and F2 are the prime and secondary focus locations, respectively. Ray path F2-A-OA goes to the far edge of the main reflector, and F2-B-IB goes to the edge of the main reflector nearest the axis of the parent paraboloid. Lines B-OB and A-IA are parallel to the F2-A-OA and F2-B-IB rays. The lateral displacement of the subreflector in making these ripple measurements was roughly along the direction of a 45-degree angle down and to the left in this figure. F2 is in the plane of the Receiver Room roof. The distance F2-B is 15.9 meters, F2-A is 13.5 meters, and the L-, S-, and C-band feeds extend about 1.4, 0.9, and 0.9 meters above the Receiver Room roof, respectively.

Periodogram features L, K, and J are almost certainly due to reflections from the Receiver Room roof and the tops of the L-, S-, and C-band feeds sending a small portion of the antenna noise signal on an extra path distance to subreflector edge B and back. Periodogram features E through H could be due to reflections off the structure of the prime focus receiver boom located to the top left of Figure 8. Spillover noise in a given direction could interfere with itself and cause

Table 3: Tentative identifications of multipath interference features in the periodogram of Figure 7. See Figure 8 for subreflector/feed geometry references.

Feature	Inverse Period (MHz^{-1})	Period MHz	Path Length Diff from Period (m)	Remarks or possible cause
A	0.0175	57	5.25	
B	0.0200	50	6.00	interf. of rays IA-A-F2 & IB-B-F2 ??
C	0.0250	40	7.49	
D	0.0350	28.6	10.49	
E	0.0525	19.0	15.74	
F	0.0688	14.5	20.61	
G	0.0850	11.8	25.48	
H	0.0925	10.8	27.73	
J	0.0975	10.3	29.23	S.R. edge B to L-band feed (29.0m)
K	0.1000	10.0	29.98	S.R. edge B to S or C-band feed (30.0m)
L	0.1062	9.4	31.85	S.R. edge B to rcvr room roof (31.8m)

baseline ripple, if it has two ray paths to the feed. For example, spillover noise from the inner edge of the dish enters most strongly through ray path IB-B-F2, but it can also scatter from subreflector edge A and enter through path IA-A-F2. The difference in these two path lengths is about 5.9 meters, which might account for periodogram feature B. Positive identification of all of the observed ripple periods would require further measurements. Whatever the explanations, most of these features must depend on changes in relative lengths of interfering paths with subreflector displacement. All of the peaks in Figure 7 are stronger with a 1/4-wavelength subreflector displacement than with an 1/8-wavelength displacement.

2.4 Antenna noise effects on observations

In total power, position switching observations, where the *on* and *off* positions are taken by tracking the antenna over the same hour angle or elevation track, the antenna noise ripples should cancel in the $on - off$ difference spectrum. Changes in antenna elevation will cause both changes in the amount of antenna noise due to the atmosphere and spillover and the geometry of the telescope due to gravitational deformations and compensating focus tracking of the subreflector. Both of these will affect the antenna noise ripple pattern. If $on - off$ are done by tilting the subreflector or switching between two feed horns, then the antenna noise ripple cancellation will be incomplete.

Frequency switching is much more problematic since the whole antenna noise ripple pattern will shift between the *on* and *off* spectra. If the frequency switching interval is equal to half of one of the ripple characteristic periods its amplitude will be doubled in the $on - off$ difference spectrum.

One might try intentionally displacing the subreflector or frequency switching by a full ripple period between the *on* and *off* or between two $on - off$ pairs in a way that cancels the antenna noise ripple. The problem with this is that it works well for only one period or usually only one multipath route. The panel gap reflections cause ripple periods from about 1.2 to 1.8 MHz, and these reflections arrive from different directions relative to any subreflector displacement axis. The same period and direction of arrival spread is true for the longer ripple periods due to feed area reflections. One also needs to be aware that the phases of the panel gap ripples move

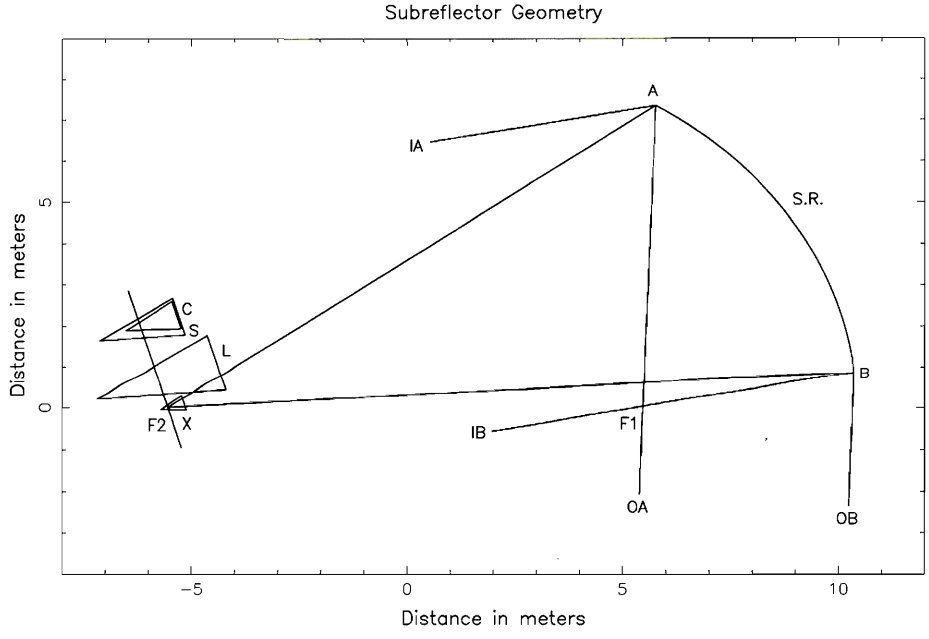

Figure 8: Subreflector and Gregorian feed geometry with telescope pointed near horizon and X-band feed in position. B-IB and A-OA are ray lines to the edges of the main reflector.

twice as fast with subreflector displacement as do the ripples due to multipaths that involve only one additional subreflector reflection. A few simple experiments with subreflector displacement indicate that the limit on the amount of ripple amplitude reduction to be expected is on the order of a factor of three and often considerably less. At a specific frequency and bandwidth one might be able to find a particular frequency switching subreflector displacement pattern that does better, but it will require some experimentation. There may also be some merit in using a much wider bandwidth than the astronomical spectrum requires to model the antenna noise baseline ripples over the part of the spectrum without spectral lines in hopes that the model will provide a good interpolation in the spectral line region of the spectrum.

A more subtle effect to watch out for is that the antenna noise portion of T_{sys} will have a frequency dependence. As mentioned in connection with Equation 1, this will show up in the $(on - off) \,/\, off$ spectrum of a source with significant continuum radiation.

Finally, a rough estimate of the amplitude of the antenna noise ripple to be expected from the GBT ranges from about 5 to 40 mK rms at 1.4 GHz to about 2 to 8 mK at 9 GHz, with the 9-MHz ripple being roughly three times stronger than the 1.6-MHz ripple. More detailed values can be found in the figures in this section. Careful total power, position switching can reduce these amplitudes by a factor of 30 or better.

One antenna noise source of baseline ripples that we did not investigate is the sun. This adds the additional parameter of the position of the sun with respect to the telescope pointing direction, and it was more than we had time for in this investigation. It is certainly an aspect of the telescope that needs better quantification.

3 Antenna and receiver response to a continuum radio source

For a good understanding of the spectral characteristics of the antenna, feed, and receiver front-ends of the GBT we need to separate the frequency dependencies of gain and noise power. These two quantities must then be characterized for different parts of the antenna/front-end system to the extent possible. The previous section described the far-off-axis antenna gain effects on environmental noise power entering the system. This section deals with the main beam system characteristics and the signal path through the feed and low-noise amplifiers.

There is no laboratory or absorber-type noise source that can be fed into the receiver or feed input and assumed to be spectrally flat to the levels of interest to radio astronomy. Return-loss mismatches smaller than -60 dB can be significant, and it is impractical to construct test noise sources to this accuracy for the wide variety of receivers and test points in the GBT. Hence, we are left to tease apart the various gain and noise spectrum effects beginning with the assumption that the spectrum of a continuum noise source in the main beam of the telescope is smooth and varies with a something like a simple power of frequency across the measured passband.

As was done in the investigation of antenna noise, the antenna optics geometry can be varied to uncover the effect of the antenna's gain on the radio source's signal. The major reflector antenna gain effect that we expect is multipath interference, so the periodograms of $on - off$ spectra are again useful.

For each receiver the antenna response to a continuum radio source was investigated by performing $on - off$ observations toward continuum sources with varying intensities. Typically, 5-minutes were spent on and then 5-minutes off the continuum source. Figure 9 shows 200-MHz bandwidth observations toward the 5.7 Jy continuum source 2232+1143 at S-band (1990 MHz). Three, 5-minute $on - off$ pairs have been averaged together. The secondary reflector was positioned at the nominal focus for both the on and off observations. Note the quasi-periodic, large scale ripple with a period of $\sim$ 100 MHz and an amplitude of $\sim$ 3% of the system temperature. Similar baseline structures are observed in all the Gregorian receivers and will be discussed below. Also present in the channel Y data is the 9-MHz ripple thought to be caused by reflections from the sub-reflector and Gregorian feeds and the 1.6-MHz ripple caused by reflections from circumferential gaps between surface panels.

A new feature at 0.435 MHz^{-1} (1/2.3 MHz) is also visible in both X and Y channels of the $on - off$ spectra. This ripple is clearly detected in the periodogram shown in Figure 10. This frequency is close to the 2.4-MHz ripple detected from the optical fiber modulators (see Section 4.1). However, the ripple phase changes by half of a period when the sub-reflector is shifted by $\lambda/4$, indicating a single reflection involving the sub-reflector. The 2.3-MHz ripple period corresponds to a one-way distance of $\sim$ 65 meters which is the distance between the sub-reflector and the primary reflector near the axis of the parent paraboloid (see Figure 4). This ripple has also been detected at L-band (1400 MHz) and C-band (5000 MHz). The relative power of the ripple increases as λ^2.

3.1 Quasi-periodic ripples in continuum source noise

When observing strong continuum sources with the GBT Gregorian receivers, quasi-periodic ripples are detected that appear to reside upstream of the first LO mixer and downstream of the optics. The phase of the ripples are fixed to sky frequency and do not change when the optical elements are adjusted: thus these features appear to reside in the feed, waveguide components and LNA components.

Figure 11 plots $on - off$ spectra for three continuum sources at L-band. Because of significant RFI only 50-MHz bandwidths were used. Two curves are shown for each source corresponding to

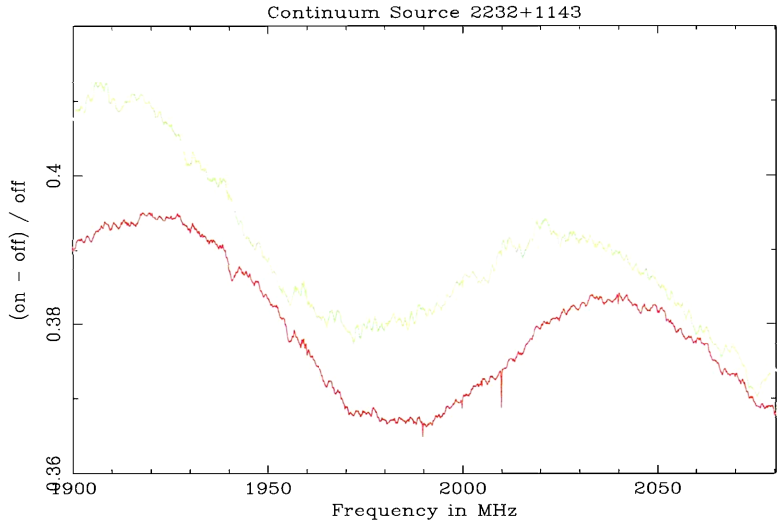

Figure 9: (on – off) / off spectra toward the continuum source 2232+1143, centered at a sky frequency of 1990 MHz. Three $on - off$ pairs have been averaged. The red or darker curve is for receiver channel X and the green, lighter curve is for channel Y. The channel Y data have been offset by −0.1. The spectra have been smoothed by truncating the autocorrelation functions to 2048 lags and Hanning convolved.

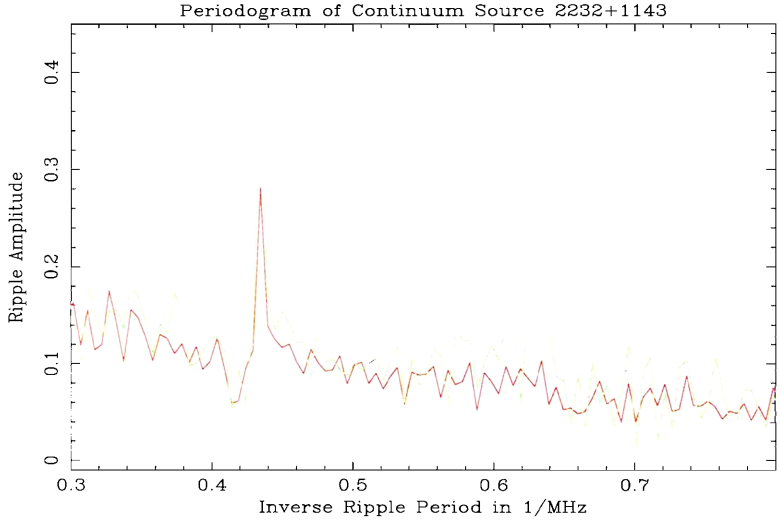

Figure 10: Periodograms of the spectra in Figure 9. The red or darker line is receiver channel X, and the green, lighter line is channel Y. The spike at 0.435 MHz^{-1} corresponds to a ripple period of 2.3 MHz and a one-way reflection distance of 65 meters.

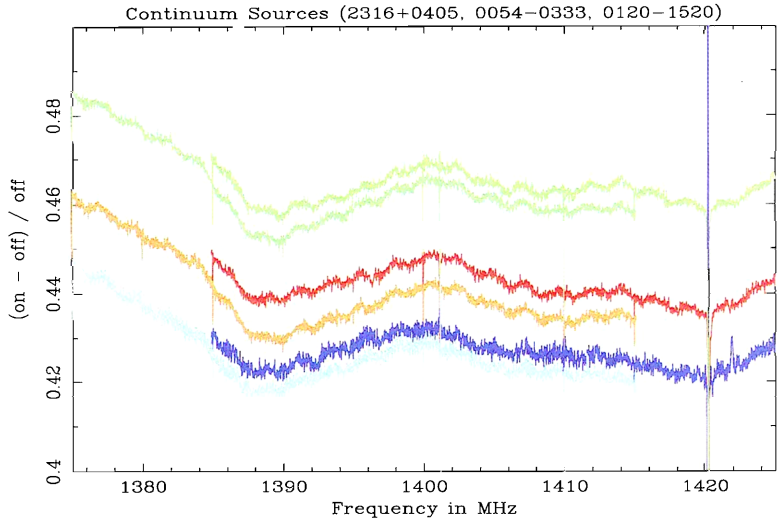

Figure 11: (on - off) / off spectra toward the continuum source 2316+0405 (4.68 Jy, red and orange curves in the middle), 0054-0333 (2.21 Jy, dark blue and blue-green curves at the bottom), and 0120-1520 (5.08 Jy, green and green-cyan at the top). The intensity scale of 0054-0333 and 0120-1520 were scaled by 1.9 and 0.98, respectively to put their spectra close to that of the first source, 2316+0405, for easy comparison. All spectra have been smoothed by truncating the autocorrelation functions to 4096 lags and Hanning convolved.

Table 4: Front-end Ripple Periods.

	Receiver Band			
	L	S	C	X
Frequency (GHz)	1.4	2	5	9
Ripple Period (MHz)	30	100	65	—

center frequencies of 1395 and 1405 MHz. Note the ~ 30-MHz ripple in all spectra that are fixed in sky frequency and closely scale with source continuum intensity. Larger bandwidths can be synthesized by concatenating several 50-MHz pass-bands. Figure 12 illustrates such a composite spectrum toward 2316+0405 that spans 190 MHz. Each 50-MHz pass-band has been overlapped by 10 MHz. Unless the system temperature has significantly changed between successive spectra it is puzzling why the spectra do not match up in the overlapped region (this is discussed in more detail below). The vertical lines correspond to RFI. There is a hint of a ~ 85-MHz ripple in these spectra.

At S-band (1990 MHz) a wider bandwidth of 200-MHz can be used. Figure 9 shows $on - off$ spectra toward 2232+1143 as discussed above. The largest wavelength ripple detected is at ~ 100 MHz. These features are fixed to sky frequency, they do not involve multi-path reflections from the telescope structure, and the results are generally repeatable.

Similar observations were made at C-band (5000 MHz) and X-band (9000 MHz) using the largest available Spectrometer bandwidth of 800-MHz. These receivers also have large-scale spectral baseline structure that appears to be located in the front-end. The character of the

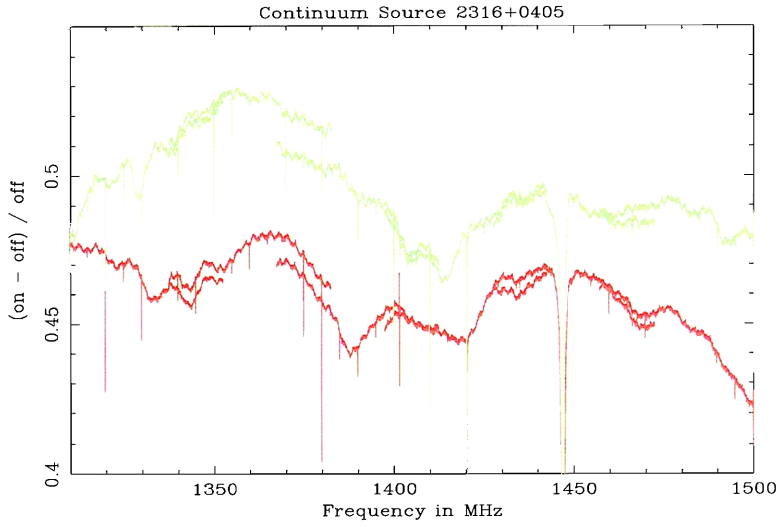

Figure 12: (on - off) / off composite spectra toward the continuum source 2316+0405 that has a flux density of 4.68 Jy at a frequency of 1400 MHz. The red or darker line is receiver channel X, and the green, lighter line is channel Y. The spectra have been corrected for a source spectral index of −1.006 derived from the NVSS (Condon *et al, 1998, AJ, 115, 1693) flux densities at 1.4 and 5 GHz.*

baseline structure is somewhat different, however. Figure 13 shows $on - off$ spectra toward 0137+3309 at C-band. A 65-MHz ripple is clearly present with an amplitude of a few percent of the total system temperature. The baseline structure appears more sinusoidal than the L or S-band structure. Additional investigation has revealed that these smooth features were at least in part due to water on the S-band feed. In contrast, the results of $on - off$ spectra toward 3C48 at X-band appears less sinusoidal (see Figure 14). The baseline structure is irregular with very sharp features. The character of these X-band spectra is not consistent with typical reflections between different front-end components (e.g., the feed and waveguide window). Such baseline structure has been observed before whereby weak cavity resonances are formed in the dewar resulting in significant structure in system temperature spectra. Possible locations for this radiation are irregularities in the waveguide joints or the thermal gap located in the dewar. Copper tape placed around the waveguide joints near the feed throat had essentially no effect on the baseline structure. Further investigation of the sharp features in the X-band spectrum are described in Section 3.3.

Each receiver appears to have unique baseline structure that is located in the front-end components. This has been confirmed by changing the first LO mixer and the telescope optics. The phase of these structures is fixed to sky frequency and is not affected by sub-reflector motion. In some cases the baseline structure appears quasi-sinusoidal, suggesting reflections between various components in the front-end such as the LNA, OMT, or feed horn. Table 4 summarizes the main ripple frequencies observed for each receiver band.

3.2 Feed/LNA noise model

We know that there are reflections within the feed and waveguide system of the GBT receivers due to small impedance mismatches with return losses in the -30 to -60 dB range. Also, the

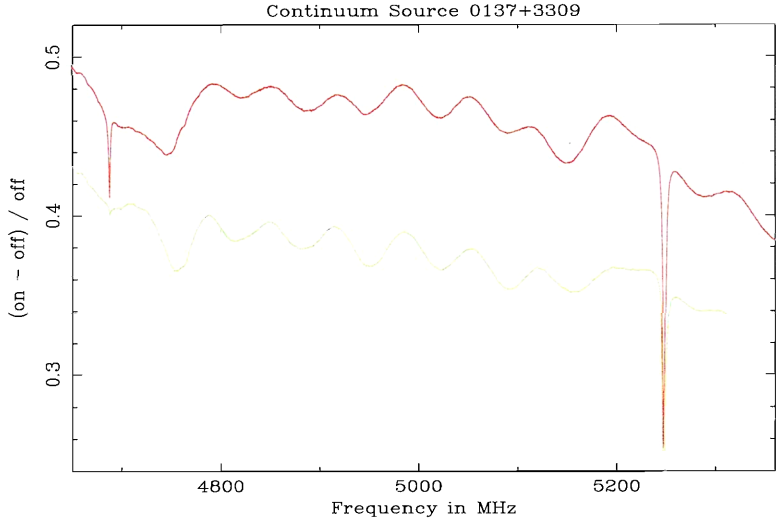

Figure 13: (on - off) / off spectra toward the continuum source 0137+3309 that has a flux density of 6.6 Jy at a frequency of 5000 MHz. The red or darker line is receiver channel X, and the green, lighter line is channel Y. The spectra have been corrected for a source spectral index of -0.81 derived from the NVSS flux densities at 1.4 and 5 GHz.

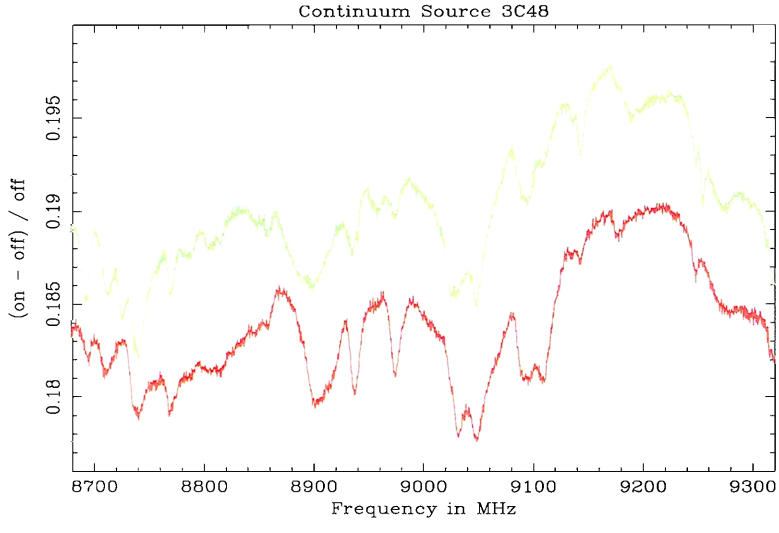

Figure 14: (on - off) / off spectra toward the continuum source 3C48 that has a flux density of 3.1 Jy at a frequency of 9000 MHz. The red or darker line is receiver channel X, and the green, lighter line is channel Y. The channel Y data have been offset by -0.022 for clarity. The spectra have been corrected for a source spectral index of -0.9 derived from Ott *et al, 1994, A&A, 284, 331*

optimum noise impedance of the LNA's is often at a point where its input return loss is on the order of -10 to -20 dB. These reflections can cause gain ripples in the feed and waveguide system in the same way as multipath interference in the antenna system.

We know, too, that noise is generated in the waveguide components due to ohmic losses and in the LNA input stage. These noise sources transmit coherently in both directions, in the intended signal flow direction toward later receiver stages and toward the feed aperture and reflector antenna. The backward-traveling noise components can be reflected by the small mismatches and returned to the LNA input where they interfere with their forward-traveling components. Again, the extra path length of the backward-traveling power introduces a ripple on the noise spectra. If more than one reflection and path length are significant, the spectrum can be fairly complex.

Figure 15 is a schematic representation of a receiver feed and waveguide system. Equations 3 and 6 can be used to compute the expected peak-to-peak ripple amplitude from a given reflection return loss in the feed-waveguide system by setting $V_R = V_0$ and P_0 equal to the noise component temperature. With 5 K of thermal noise traveling in both directions in the waveguide and return losses of 30, 40, and 60 dB, the peak-to-peak ripples will be 0.63, 0.2, and 0.02 K, respectively. If we assume a 20 K system temperature, these numbers would represent a peak-to-peak variation in system temperature ranging from 3.2 to 0.1%.

Noise from the LNA input stage is a bit more complicated because $V_R \neq V_0$, but the ratio of these two values is probably less than two, so the ripple amplitude from this source and the wave guide reflections should be comparable to or somewhat less than those of the ohmic loss noise sources.

Noise from the antenna (continuum radio source, cosmic background, atmosphere, and spillover) will also be modified by reflections in the LNA-waveguide-feed structure. Because this begins as forward-traveling noise the effective return loss to use in Equations 3 and 6 is the sum of the return loss that reverses its direction (typically at the LNA input) and the return loss where it is reflected to the forward direction again. If we assume a total antenna noise temperature of 10 K and an LNA return loss of 10 dB, then the expected peak-to-peak ripple amplitude from waveguide return losses of 30, 40, and 60 dB will be 0.4, 0.13, and 0.013 K, respectively. With a 20 K system temperature, these number correspond to a peak-to-peak variation in system temperature ranging from 2 to 0.06%. A radio source with a 10 K antenna temperature would have a peak-to-peak variation in its receiver power ranging from 4 to 0.13%.

The period of the noise spectrum ripples due to waveguide and feed reflections will depend on the effective distance between the noise sources and reflections or between two reflections. The longest component in the system is generally the feed. Table 5 lists the lengths of the GBT feeds and the corresponding ripple periods assuming a wave velocity equal to the speed of light. The total effective signal path length through the waveguide and coax line to the LNA may be on the order of 50% longer, and the ripple periods may be scaled down by about 30%. The largest reflections at the LNA, OMT, waveguide window, and feed throat are separated by smaller distances than the feed length so the highest ripple amplitudes would be expected at somewhat longer ripple periods.

— Tentative conclusion: From the ripple amplitude calculations above and the ripple periods given in Table 5 it seems unlikely that most of the observed variation in T_{src}/T_{sys}, such as in Figures 9, 12, 13, and 14, can be explained by feed-waveguide-LNA reflections alone. For a more detailed analysis of the noise and reflection properties of the system shown in Figure 15 see the attached memos by R. F. Bradley (January 30, 2003) and M. W. Pospieszalski (January 28, 2003).

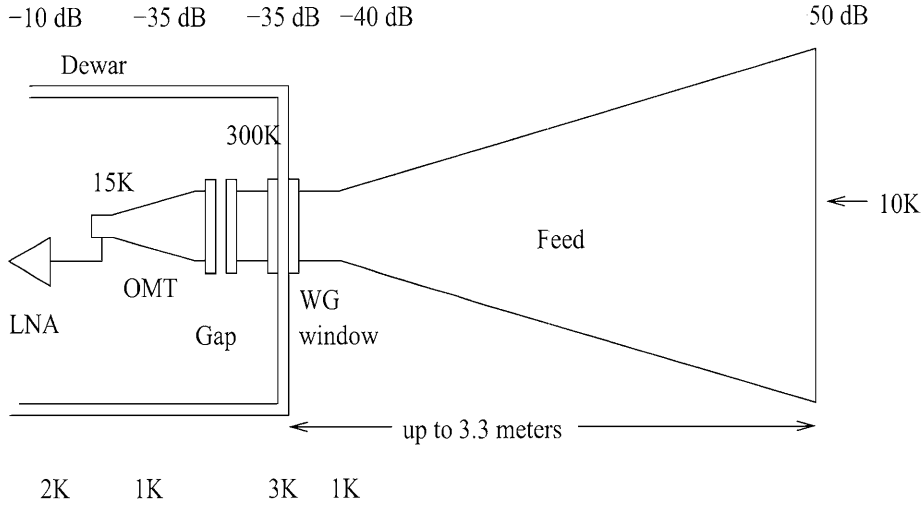

Figure 15: GBT receiver feed-waveguide-LNA diagram. Thermal noise sources and reflection points are labeled with typical temperatures and return losses, respectively.

Table 5: Feed lengths and corresponding ripple periods implied by reflections at this distance.

	Receiver Band					
	L	S	C	X	Ku	K
Frequency (GHz)	1.4	2	5	9	14	20
Feed Length (m)	3.3	2.2	1.2	0.56	0.37	0.25
Ripple Period (MHz)	45	68	125	268	405	600

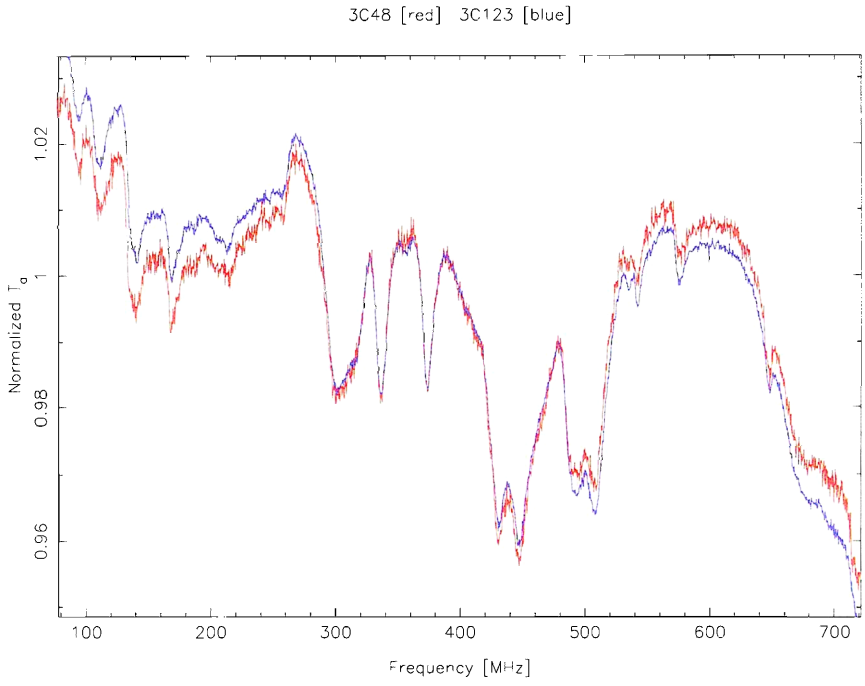

Figure 16: The normalized antenna temperature toward 3C48 (red) and 3C123 (blue). Each spectrum consists of one 5 minute on-off pair. The antenna temperature, in units of the system temperature, were divided by the median value in the spectrum. The spectra are centered at a sky frequency of 9000 MHz.

3.3 Fine scale structure due to cavity resonances

The baselines when observing strong continuum sources with the GBT tend to show objectionable structure, as mentioned elsewhere in this report. The X-band (8-10GHz) receiver in particular exhibited a great deal of relatively fine-grain structure that makes even narrow-band observations difficult.

Figure 14 shows the results of two 5 minute, on-off pair observations toward 3C48 (3.4 Jy at 8000 MHz). The very irregular structure is similar to what was reported earlier and appears in both polarizations. The amplitude of these features scales with source continuum intensity. Figure 16 show the normalized antenna temperature for 3C48 and 3C123 (10.6 Jy at 9000 MHz). The baseline structure is very similar.

These baseline features appear to be upstream of the first mixer. Figure 17 shows the antenna temperature versus sky frequency for two spectra centered at a sky frequency of 9000 MHz and 9010 MHz. Notice that most of the baseline structure is fixed with sky frequency. Similar to other Gregorian receivers there appears to be broad band frequency structure which is upstream of the first mixer but not related to the optics.

Independent analysis by Marian Pospieszalski and Richard Bradley showed that reflections between the cryogenic LNA (which has quite poor input return loss when matched for optimum noise), and other input components such as the feed horn aperture, can introduce ripple in the receiver noise. As shown earlier, the $(on - off)/off$ data processing causes any non-uniform receiver noise spectrum (as opposed to gain ripples) to show in the baseline spectrum. However,

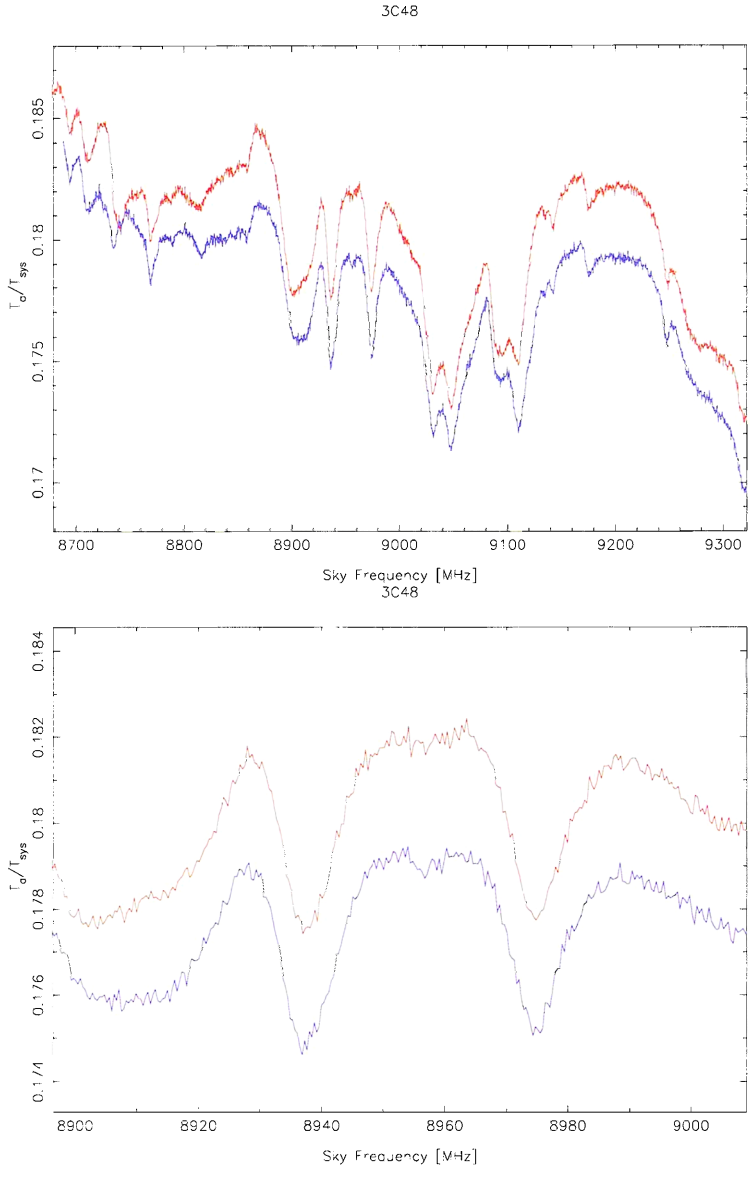

Figure 17: The antenna temperature toward 3C48, in units of the system temperature, centered at a sky frequency of 9000 MHz (red) and 9010 MHz (blue). The lower panel shows an expanded view.

the LNA-Feed Horn reflection should be quite well-defined and dependent on the path length, which does not fit the observed characteristics.

Figure 15 shows in some detail a typical GBT front-end in the area between the feed horn and the LNA. The circular waveguide throat section of the feed horn connects through a low-loss vacuum window to a thermal transition assembly, which provides high thermal impedance by a small gap in the circular waveguide wall, and thereby allows the following components to be cooled to cryogenic temperatures. Following the gap is a polarizer or OMT to separate the two polarizations, and then each channel connects to a LNA. Not shown are stripline cal couplers between the OMT and the LNA; some receivers also have cooled isolators before the LNA. Due to circumstances, the Ku-band (12-15.4GHz) front-end was first investigated in depth, to try to understand the baselines evidently due to fine-grain receiver noise structure. This receiver was placed in the Equipment Room and connected directly into two of the Converter Modules.

The Ku-band receiver is one that has cooled isolators in front of the LNA's, so a tight waveguide short over the dewar input waveguide acts like a cold load of about 20K (the isolator load physical temperature, plus the effective temperature of any input losses). Figure 18 shows the total power spectra for the receiver with the thermal gap as normal, and with the gap temporarily covered with copper tape. Based on these results, it is likely that the several large noise spikes seen in the normal state are due to resonances or leakage related to the thermal gap. This conclusion was strengthened by S. Srikanth using the EM modeling program Quickwave. The Ku-band thermal gap uses a simple choke ring to provide RF isolation, and A. Kerr suggested an alternative broadband choke design. A new gap using Kerr's suggestion has been designed and is now in fabrication to be evaluated.

Since the X-band baselines on continuum sources seemed to be particularly bad, when the telescope schedule allowed this front-end was removed and brought to the Equipment Room for similar testing. A shorting plate was placed over the input waveguide. The total power spectrum showed one spike near 9.7GHz that seemed similar to those seen in the Ku-band total power and were identified with the thermal gap. Nothing was seen that obviously would cause the structure seen in Figures 14, 16, and 17. In order to simulate a continuum source observation, we decided to try using the internal calibration noise sources. While the noise cal is injected after the polarizer, part of the injected noise will be reflected off the LNA isolators, travel back to the waveguide short, and back into the receiver. This excess noise should show the frequency structure seen on the telescope, if it is generated in the receiver. For this receiver the low cal is about 2.5K and the high cal is 15-30K.

A series of scans were taken while manually controlling the receiver noise sources. During the first scan pair, both the low cal and the high cal sources were off. During the second pair, the low cal was on. During the third pair, the high cal was on. During the fourth and final pair, both cals were again off. Figure 19 shows the resulting scan ratios for the LCP channel for this sequence of scans: the RCP channel results are similar. While there is large ripple when scan pairs with the noise sources on and off are ratioed (expected because of the standing wave due to the waveguide short), there is little evidence of extremely sharp frequency structure like that seen on the antenna.

The negative result led to a close inspection of the feed horn assembly. Several quality issues were identified with the assembly:

- One joint in circular waveguide between the feed horn and the vacuum window was found to have a mistake that resulted in a 0.015 inch gap in the waveguide wall. The joint was re-machined.
- Several (10-12) metal chips were found in the feed horn corrugations. These were evidently left from the feed fabrication process.

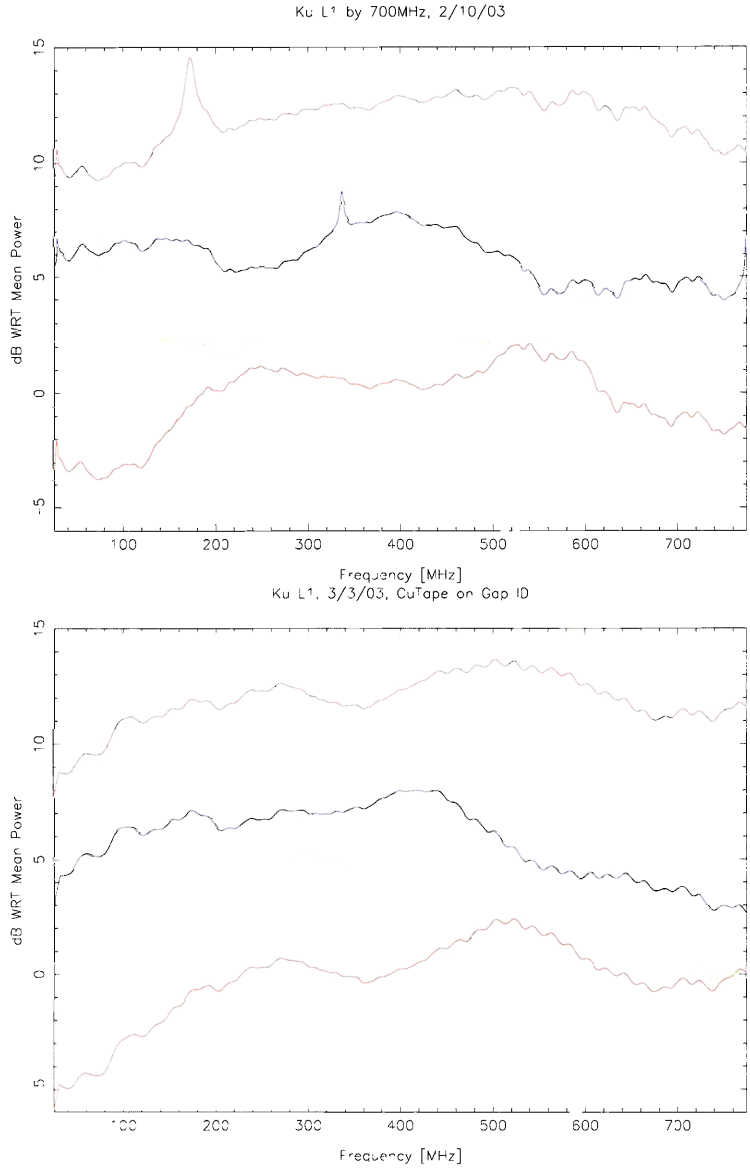

Figure 18: The total power spectra of the Ku-band receiver with a shorting plate over the dewar input waveguide. Each panel covers 11.7 (lower left) to 15.2 (upper right) GHz, by five traces offset vertically for clarity and in frequency by 700MHz. The upper panel has the waveguide thermal gap as normal: the lower panel has the gap temporarily covered by copper tape.

- The chromate surface finish on the aluminum feed horn is generally non-conductive, and we became concerned that this thin dielectric layer on the flange faces could be a detrimental factor. Hence, we mechanically removed the chromate coating from all the joint flange faces. (The horn is fabricated in four sections with bolted joints.)

- A second waveguide joint had a noticeable oily film between the flanges. An investigation concluded this was cutting oil from the installation of some helicoil threads when the receiver was off in December 2002, and obviously the joint was not properly cleaned.

After these items were corrected, the front-end was reinstalled and observations of continuum sources repeated to evaluate possible changes in the performance.

Figure 20 shows the results of an on-off observation of 3C218; compare with Figure 14, on 3C48. The vertical ranges of these two figures are the same, as a fraction of the source temperatures. The baselines after the lab work, while certainly not flat, are significantly smoother than earlier ones. Note also that there is little commonality between the spectra of the two polarizations, unlike what was seen before correcting the feed and waveguide defects. The most likely explanation for the improvement in continuum source baselines is that the clean-up of the waveguide joints eliminated highly irregular losses at these joints (or one could think of it as noise with lots of frequency structure leaking into the receiver). The $(on - off)/off$ calibration causes any irregularities (even at the fractional kelvin level is significant) in the system noise to appear in the baseline response. Since it is almost impossible to measure feed horn loss with the degree of precision needed to see these effects, there is no substitute for extreme care in fabrication, quality control, cleanliness, and assembly of the receiver input waveguide and feed horn.

3.4 Continuum source spectrum stability

One of the results of this investigation will be to improve the noise spectrum characteristics of the GBT receivers with modifications to current receivers and design considerations in new receivers. However, it is not practical to eliminate all of the distortions to continuum source spectra so the remaining effects must be calibrated. The best calibration technique is to measure the system response to a continuum source that is as much like the continuum source with expected spectral line radiation as possible, as is nicely described by Ghosh and Salter in the book "Single-Dish Radio Astronomy: Techniques and Applications," ASP Conference Series, Vol. 278, p521. Since this generally requires moving the telescope to a different direction in the sky and involves a time delay between calibration and observation of the source of interest, we need to know how far in time and angular distance one can carry the calibration. This section presents a number of measurements that address these questions.

Figure 21 shows the result of using one continuum radio source to calibrate the spectrum of another one using the C-band (5 GHz) receiver with a 200-MHz spectrometer bandwidth. The left-hand panel of this figure shows the (on - off) / off or T_{src}/T_{sys} spectra for NGC7027 for the two receiver channels. In the central 90% of the passband the variation in source to system temperature ratio is on the order of 5% on a frequency scale of about 50 MHz. Much smaller variations can be seen at smaller frequency scales. The blip near 5100 MHz is probably RFI. The integration time for each of the *on* and *off* spectra is five minutes.

The right-hand panel of Figure 21 shows the ratio of T_{src}/T_{sys} spectra for 3C48 and NGC7027 in the top red (dark) and green (light) curves. At this frequency the two sources have nearly the same flux density so the values in the curves are close to one. Aside from a difference in spectral index of the two continuum radio sources, the curve for receiver channel X is reasonably flat, which indicates that the continuum response of the receiver can be carried between two sources that are at least 45 degrees apart in telescope elevation. 3C48 was at 76 degrees elevation and

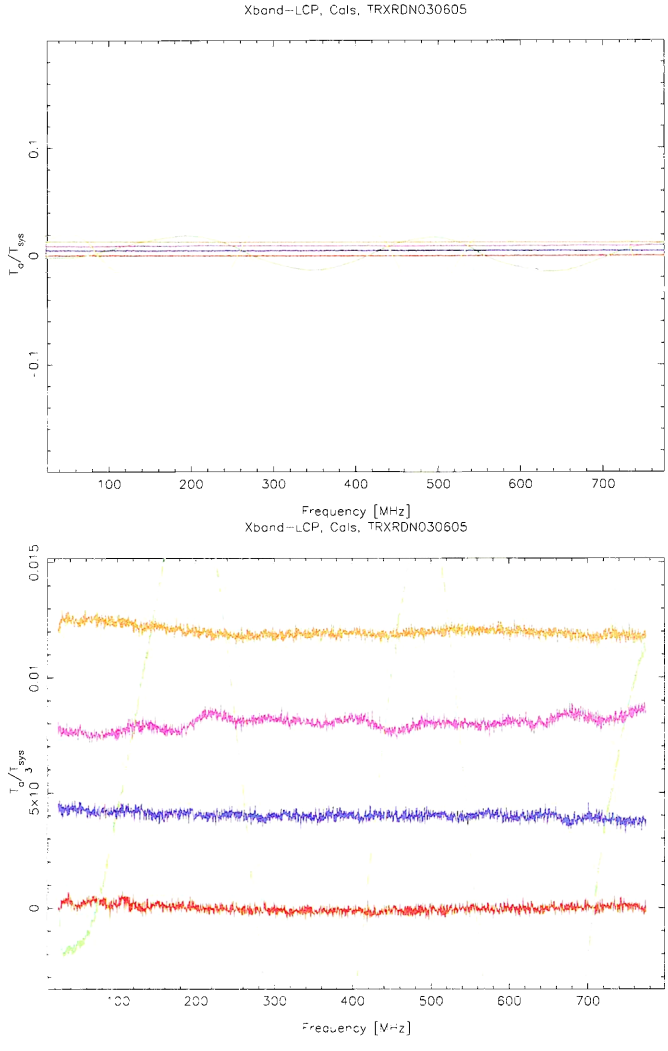

Figure 19: $(on - off)/off$ for the X-band LCP channel with the input waveguide shorted, for various states of the receiver noise cal sources. Cases are: Cals Off for both scans (red); Low cal off for 'off' and on for 'on' (green): Low cal on for both (blue); Low cal on for 'off' and high cal on for 'on' (cyan): high cal on for both (magenta): High cal on for 'off', and both cals off for 'on' (yellow): and both cals off for both 'off' and 'on' (orange - the top flat trace). The scan times were 300 seconds. The central portion of the upper panel is expanded in the lower panel.

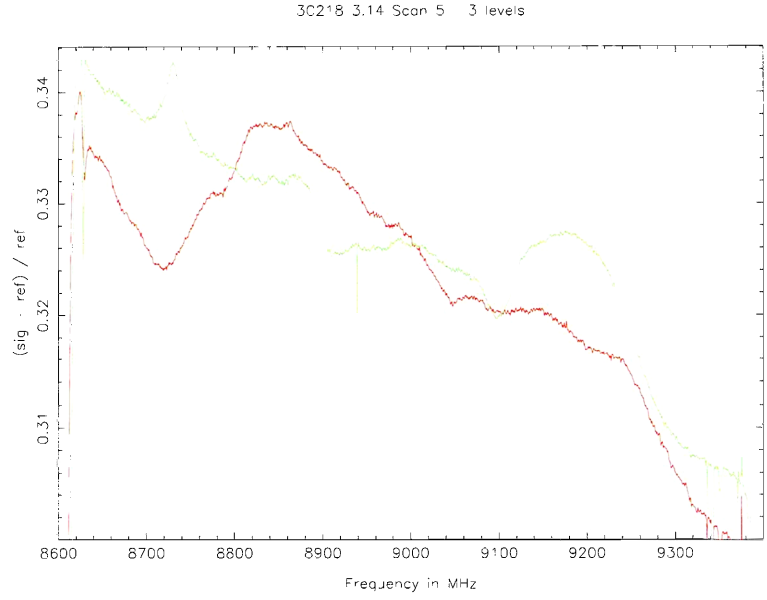

Figure 20: $(on - off)/off$, for the X-band LCP (red) and RCP (green) channels, measured on-off 3C218 after feed horn quality problems were corrected. Compare with Figure 14.

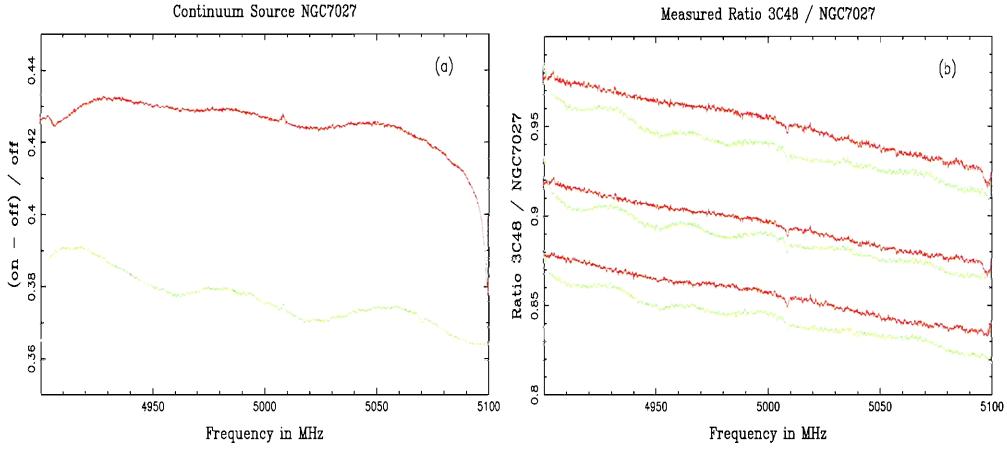

Figure 21: (on - off) / off spectra for NGC7027 (a) and the ratio of measured spectral power densities of 3C48 to NGC7027 (b) using a 200 MHz bandwidth. The vertical scale is the fraction of system noise power density. The red (dark) curve is for receiver channel X and the green (light) curve for channel Y. In panel (b) the top two spectra are ratio averages of (on - off) / off spectra: the middle two spectra are ratio averages of (on - off) raw spectra for same scan pairs; and the bottom two spectra are ratio averages of (on - off) raw spectra using a different scan pair for NGC7027 with the bottom two plots offset vertically by -0.05 for clarity.

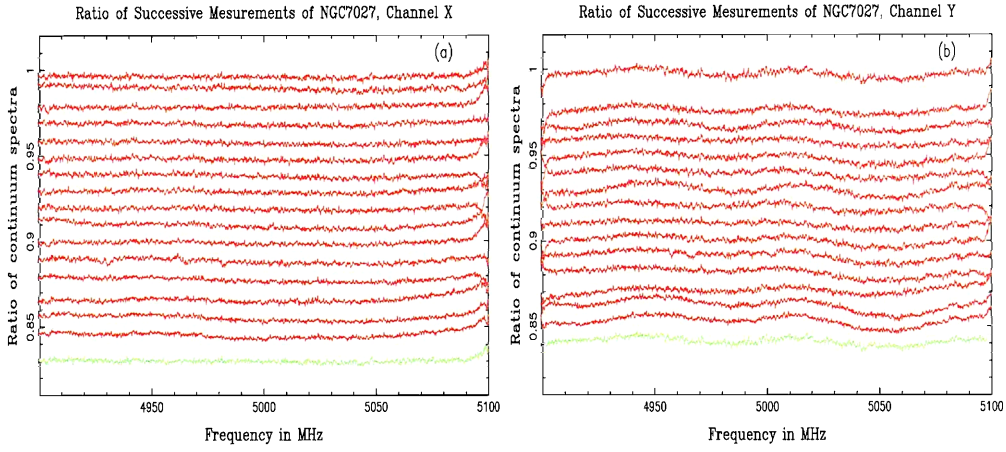

Figure 22: Ratio of NGC7027 continuum source (on - off) / off spectra at about 11-minute intervals extending to 3 hours 5 minutes. Panel (a) is receiver channel X and (b) is channel Y. The top plot is the ratio of the spectrum from the second scan pair to the first pair. The next plot down is the ratio of spectra for scan pairs 3 and 1, and so forth. The plots are assigned arbitrary offsets to create the time progression from top to bottom. The green plot at the bottom is a repeat of the first plot at the top for comparison of the first and last ratio spectrum.

NGC7027 at 31 degrees. The spectrum ratio for receiver channel Y varies by about 1% peak-to-peak on a scale of about 30 MHz. This ripple period is not characteristic of the discovered antenna multipaths or any IF system reflections so it requires further investigation.

The lower two pairs of curves in Figure 21b show the ratios of spectral powers from 3C48 and NGC7027 using only the $(on - off)$ difference spectra rather than T_{src}/T_{sys} spectra. The results are essentially the same. This is a bit remarkable since T_{sys} is expected to be a somewhat higher at lower elevation. The vertical offset of the top pair of curves from the middle pair is due to this difference in T_{sys} at lower elevation for NGC7027, but the shape of the spectral power ratio appears to be unaffected. The receiver is sufficiently stable between the measurements of the two sources to permit the ratio of uncorrected spectrum values to be computed directly.

Figure 22 shows the results of a test of system stability of the two channels of the C-band (5 GHz) receiver with a 200-MHz bandwidth over a three hour period. In this figure are plotted the ratios of the (on - off) / off spectra of NGC7027 for the two receiver channels at 11-minute intervals to the first (on - off) / off spectrum at the beginning of the three hours. The spectra for channel X show very little change over the three-hour period, but channel Y shows structure at roughly 9- and 60-MHz ripple periods. These periods are characteristic of multipath interference from reflection from the receiver room and IF system instabilities, respectively, as explained elsewhere in this report. Even the ratio of the first two (on - off) / off spectra show these ripples so these changes happen on times scales of 10 minutes or less. Work is in progress to improve the IF stability, and the changes in the 9-MHz ripple period from the optics needs further investigation.

One of the questions that needs to be answered in connection with continuum source response calibration is whether the telescope has a different response to an extended source than to a source that is small compared to the beam size. Figure 23 shows a test to determine the telescope response near the half-power points of the beam compared to the center of the beam. There is a bit of structure in the ratios of the east and west offset spectra to the beam center spectrum, but generally the ratios are what is expected from the decrease in beam size with increasing frequency.

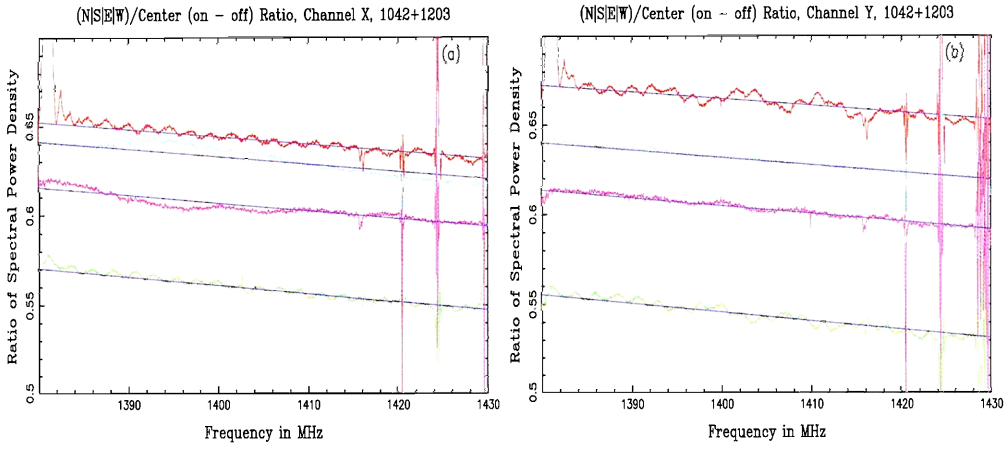

Figure 23: Ratios of (on - off) spectra of 1042+1203 taken with the telescope pointed about 4 arcminutes off beam center and at the beam center. Panel (a) is for receiver channel X and panel (b) is for channel Y. The red, green, blue-green, and violet lines correspond to 4-arcminute north, south, east, and west beam offsets. The blue lines show the expected ratio slope due to changing beam size with frequency.

However, the north and south offset spectrum ratios show a significant amount of ripple with a period of 2.3 MHz, which is the ripple period associated with the multipath reflection between the edges of the main reflector and subreflector nearest the axis of the parent paraboloid. Channel Y also shows some 9-MHz ripple associated with multipath reflections between the receiver room roof and the subreflector.

The data displayed in Figure 23 were taken near the meridian so the north-south offsets were nearly in the directions of increasing and decreasing elevation. Hence, the area around the specular reflection from the two surfaces moved onto or off the edges of the two reflectors with the north and south offsets so one would expect the intensity of the multipath interference to change most in these directions. If a reasonably symmetric extended source is centered in the beam one might expect the ripples from the two offset direction to partially cancel, but these measurements do make the point that some caution must be exercised when calibrating the telescope's response to extended continuum sources.

Not all continuum source spectra were as stable as those shown in Figures 22 and 23, and even the best of these calibrated spectral baselines are not perfectly flat. More extensive measurements with longer integration times need to be done in connection with specific astronomical problems to more fully explore the limits of this calibration technique. We know, for example, that the geometry of the GBT changes with elevation due to gravitational deformations and intentional motion of the subreflector to track the best focus position. Hence, we expect the pattern of the multipath interference connected with optics reflections to change with telescope elevation. This is not evident in the 5-GHz data in Figure 22, but it can be seen in similar tests, shown in Figure 24, at 1.4 GHz where the reflections are generally stronger. During the two hours of this scan series the radio source, 2316+0405, went from an elevation of 47 degrees to 27 degrees. The main feature that appears after some time is the 2.3-MHz ripple period from the subreflector to main reflector multipath. The wave in the middle spectrum of Figure 24b may have been caused by a drift in the electronics, but this remains to be tracked down.

Because of the vagaries of the weather and IF electronics baseline problems that tend to

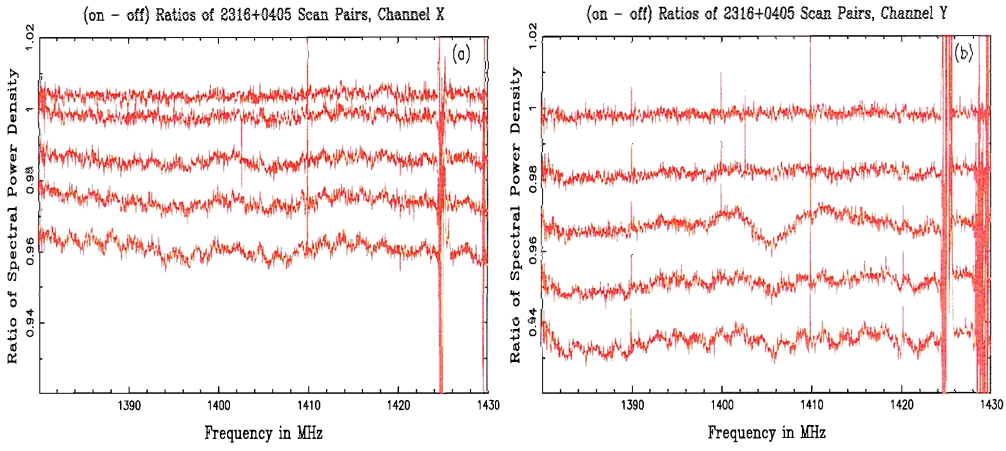

Figure 24: Ratio of 2316+0405 continuum source (on - off) spectra at intervals of 23, 47, 70, 93, and 116 minutes. Panel (a) is receiver channel X and (b) is channel Y. The plots are assigned arbitrary offsets to create the time progression from top to bottom.

dominate the spectra using wide bandwidths we were unable to make a useful assessment of continuum calibration stability in the higher frequency receivers. This is something that needs to be revisited after improvements have been made to the IF electronics.

3.5 Cal spectrum ripples

During most observations a calibration noise diode (CAL) injects noise into the system with a period on the order of a second. The goal is to provide a rough flux calibration and to remove electronic drift. The CAL signal does contain frequency structure, however, and currently the intensity scale is only known to an accuracy of about 10% with a sampling in frequency of $\sim 1\%$ of the front-end bandwidth. When spectra are generated using the CAL signal the frequency structure from the CAL itself will be folded into the final spectrum. It is difficult to decouple frequency structure arising from the CAL and other components generating system noise.

Examples of $T_{\rm cal}/T_{\rm sys}$ ratios are shown in Figure 25 toward cold sky at L (top left), S (top right), C (bottom left), and X-band (bottom right). Note that the bandwidth varies depending on the frequency. Each of these plots can be compared to $(on - off)/off$ spectra shown in Section 3.1. In general the spectral baseline structures are similar.

Although the CAL was firing during all of the observations discussed thus far, because both the on and off phases are stored separately, the CAL can effectively be removed by only using the CAL off data when processing spectra (e.g., producing $(on - off)/off$ spectra). Figure 26 shows $on - off$ spectra toward 0137+3309 at C-band (5000 MHz) that have been produced using both on and off CAL phases (panel a) and only the off CAL phase (panel b). Plotted in both cases are $(on - off)$ and $(on - off)/off$ spectra. General inspection of these plots indicates that the baseline structure is not dominated by structure in the CAL as both figures are very similar. The structure in the $(on - off)$ spectra comes primarily from the gain frequency dependence (see Figure 27). This is typically why these data are divided by the off spectrum. Also plotted is the antenna temperature, $T_{\rm a}$, in units of the CAL (effectively $(on - off)/off$ times the off system temperature evaluated per channel). This spectrum is noisier since we are dividing by a noisy $T_{\rm cal}$ spectrum.

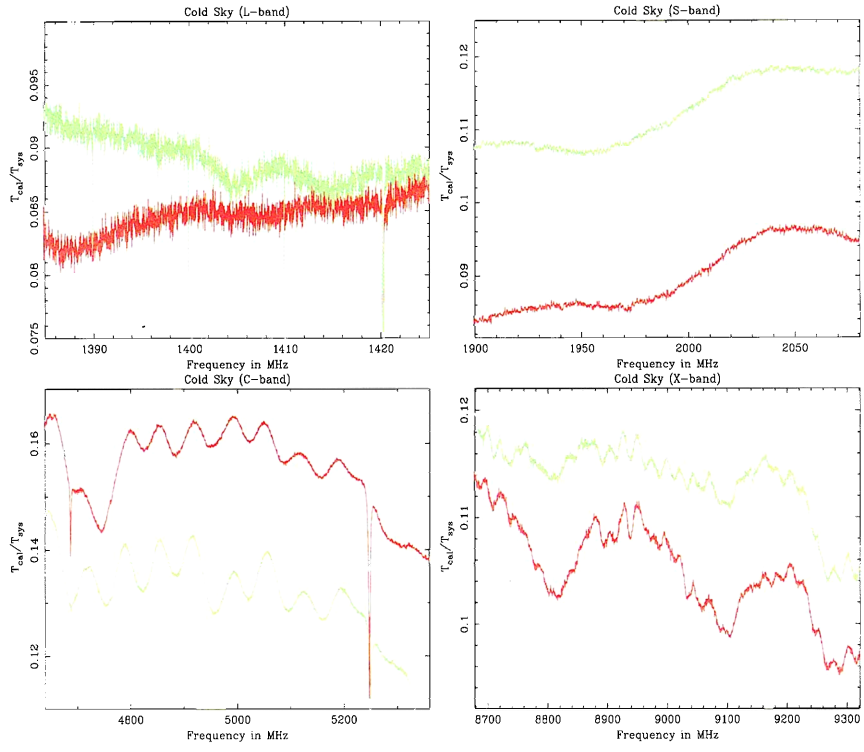

Figure 25: $T_{\rm cal}/T_{\rm sys}$ ratios toward cold sky for L, S, C, and X band. The red or darker line is receiver channel X, and the green, lighter line is channel Y. The L and S-band spectra have been smoothed by truncating the autocorrelation functions to 2048 lags and Hanning convolved.

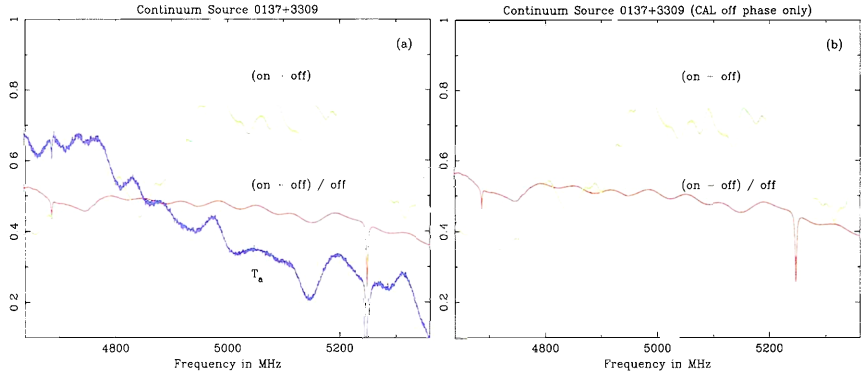

Figure 26: Total power spectra toward the continuum source 0137+3309 for channel X at C-band (5000 MHz). Panel (a): $(on - off)$. $(on - off)/off$. and the antenna temperature ($T_{\rm a}$) in units of the CAL. For the *on* and off data the CAL phases have been averaged. The $T_{\rm a}$ spectrum has been offset by -2.5 for clarity. Panel (b): $(on - off)$ and $(on - off)/off$ where only the off CAL phase has been used.

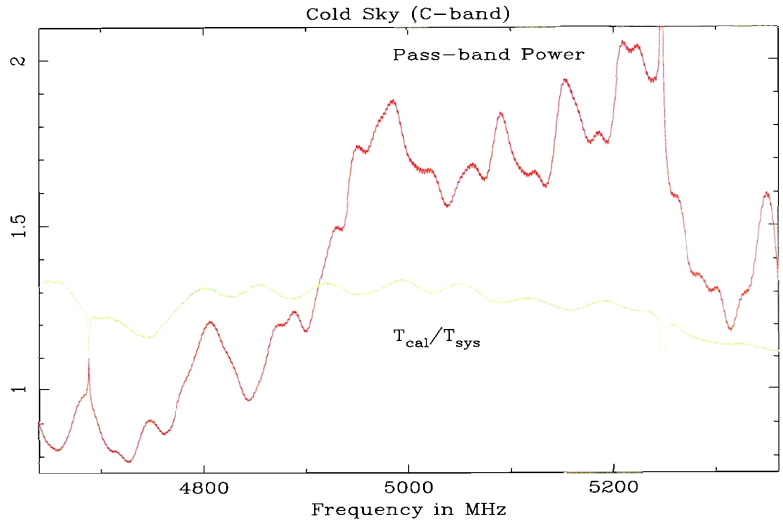

Figure 27: Total power spectra toward cold sky at C-band (5000 MHz). Plotted in red or the darker line is the pass-band power. Plotted in green or the lighter line is the $T_{\rm cal}/T_{\rm sys}$ ratio. Only channel X is shown.

4 IF system

4.1 2.4-MHz ripple from optical modulators

The GBT IF signal is routed from the front-end to the back-end via optical fiber. There is a total of 8 optical driver modules (ODM's) located at the front-end and an equivalent number of optical receiver modules (ORM's) at the back-end.

Measurements of fiber transmission stability early in GBT construction showed that twisting or bending of the fiber changes the polarization of the laser light (which is almost linearly polarized) at the detector end. Since all of the photodetectors are polarization sensitive (the "gain" depends on the light polarization). Hence, the polarization rotation gets converted to a amplitude modulation so the effective gain of the optical link is unstable. A servo system for stabilizing gain of the fiber link was developed which required the use of externally modulated lasers whose intensity can be controlled through feedback of the detected optical power at the receive end of the fiber.

Unfortunately, a 2.4-MHz period gain ripple is produced by these external modulators. Figure 28 plots the total power and the autocorrelation function for observations using the external modulator located in ODM 6. The IF noise source located in the IF rack at the GBT Receiver Room on the feed arm was used. The 2.4-MHz ripple is clear in both plots. The spike near lag 667 corresponds to a ripple period of 2.3988 MHz. The spikes near lags 1333 and 1999 are harmonics and indicate that the ripple is not purely sinusoidal.

An approximate quantitative measure of the amplitude of the gain ripple relative to the total noise spectral density was computed by summing the three highest absolute values of the ACF near each ACF ripple spike and taking its ratio to the zero-lag ACF value. Figure 29 plots the results using only the fundamental. ODM's 1, 2, 3, 5, and 6 correspond to different external modulators. ODM's 4 and 7 were out of service. ODM 8 used a direct modulator which is known to not have any gain ripple: therefore it provides a measure of the detection limit of this

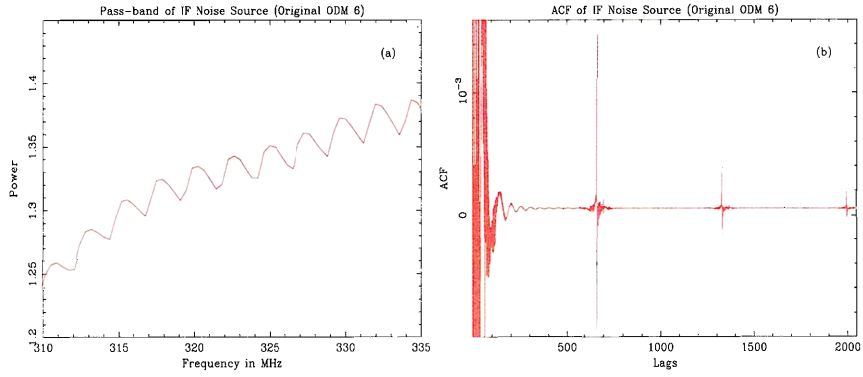

Figure 28: IF noise source spectra of an original external modulator. Panel (a): total power pass-band averaging over 60, 30-second records. Panel (b): the autocorrelation function.

algorithm. Three different IF frequencies were explored: 1500, 3000, and 6000 MHz. The spread in ripple amplitude for the five external modulators is about 5 dB, and the amplitude is about 8 dB higher at an IF of 1500 MHz than at 6000 MHz. The first and second harmonics are about 6 and 10 dB weaker than the fundamental.

The manufacturer has since modified the external modulators and claims to have reduced the amplitude of the gain ripple. Figure 30 summarizes the results of similar tests using the IF noise source for the new unit. The 2.4-MHz ripple is now not visible in the total power spectrum. The ACF plot does reveal the fundamental and the first two harmonics, but the amplitude of the gain ripple is down by ~ 17 dB. Figure 31 shows a comparison between the original and new external modulators.

Although the 2.4-MHz gain ripple has been significantly reduced it may appear above the noise level for very sensitive spectral line experiments. The ripple frequency of 2.4 MHz corresponds to $24\,\lambda$ km s^{-1}, where λ is the observing wavelength in centimeters. Unfortunately, this is similar to the line widths of many astronomical source transitions. (For example, at K-band (1.5 cm) this corresponds to 36 km s^{-1}). The magnitude of this problem will depend on the amplitude of the gain ripple in raw spectra and the stability of the ripple in time. If the gain ripple is very stable then it should cancel when processing the data.

Tests were performed to quantitatively measure the stability of the optical fiber ripple. Three different ODM's were used consisting of an original external modulator, a new modified external modulator, and a direct modulator. The IF noise source was used to simulate 5 minute $on - off$ total power pairs by calculating $(on - off)/off$ for consecutive groups of data records. A total of 400, 30-second records (200 minutes) were generated with the IF noise source. The data were divided into four groups of 100 records (50 minutes), each consisting of five $on - off$ pairs.

Figures 32, 33, 34 summarize the results for the original external modulator, the new modified external modulator, and the direct modulator, respectively. For each plot the $(on - off)/off$ spectra are shown along with the periodogram. Notice that a ~ 60-MHz ripple is quite strong in some spectra and is related to other sections of the IF system (see Section 4.2). The 2.4-MHz ripple is only detected for the original external modulator. In fact, additional averaging of the data decreases the amplitude of the ripple for this unit. Based on these results, eight modified external modulators have been ordered.

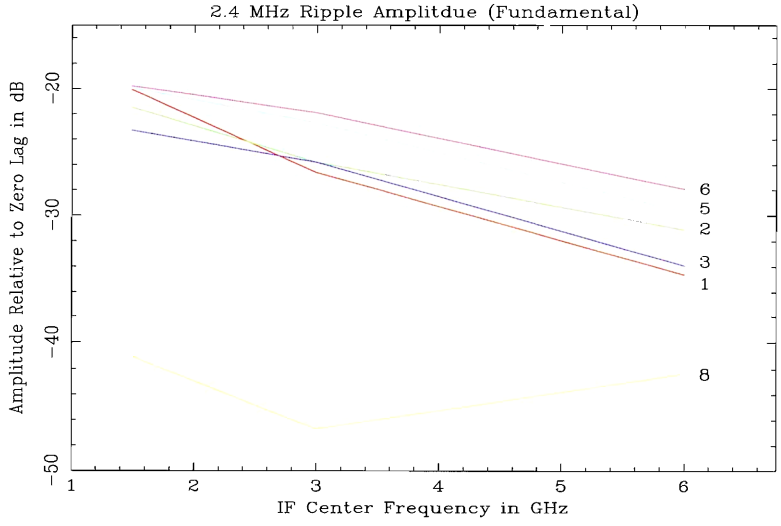

Figure 29: Approximate amplitude of fundamental periodicity component of the 2.4-MHz gain ripple measured at IF center frequencies 1.5, 3.0, and 6.0 GHz. The amplitude is relative to the zero-lag ACF value. The red, green, dark-blue, blue-green, violet, and yellow lines correspond to fibers 1, 2, 3, 5, 6, and 8, respectively. ODM 8 uses a directly modulated laser, which is known to not have any gain ripple.

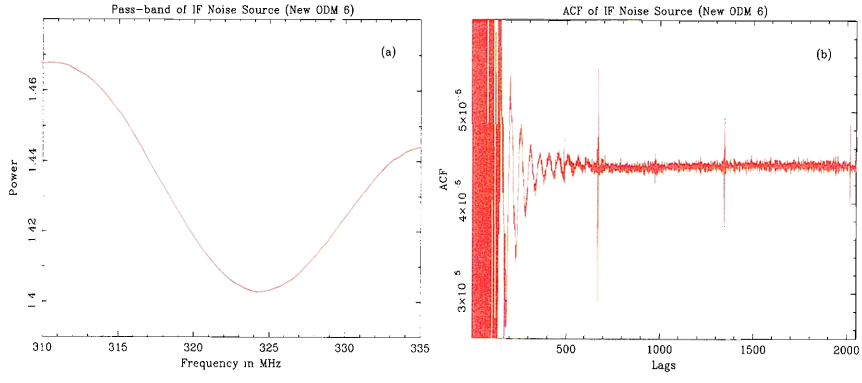

Figure 30: IF noise source spectra of the new external modulator. Panel (a): total power pass-band averaging over 60. 30-second records. Panel (b): the autocorrelation function. Compare with Figure 28

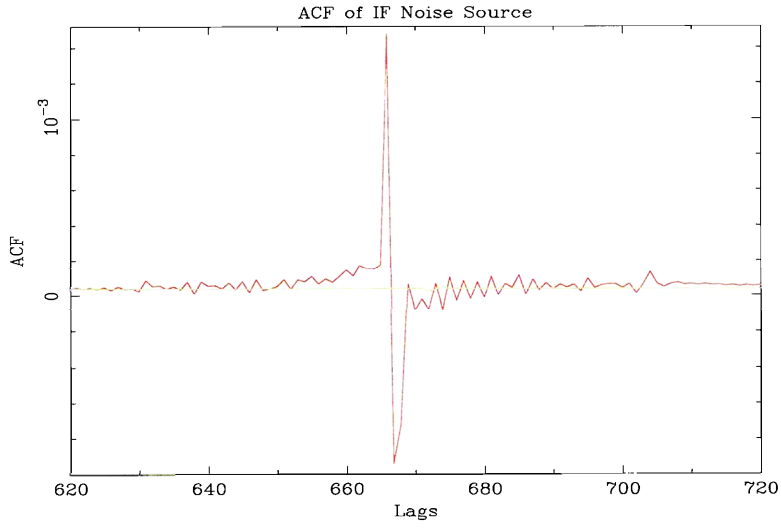

Figure 31: Autocorrelation function of the IF noise source. The red or darker line is the result for the original external modulator, while the green, or lighter line is the result for the new external modulator. A total of 60, 30-second records have been averaged.

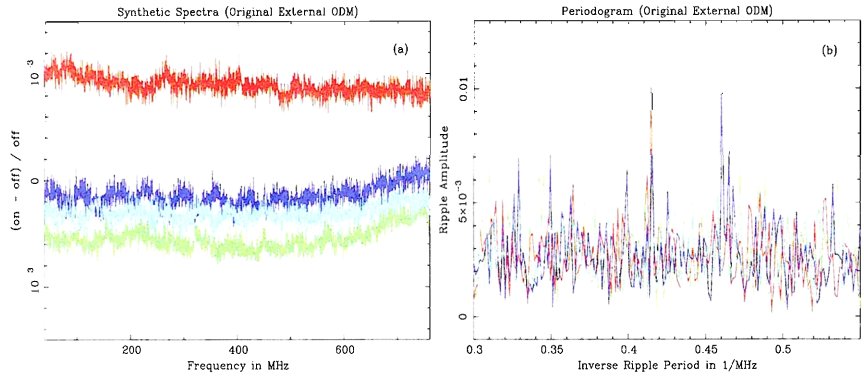

Figure 32: Synthetic spectra using the IF noise source and an original externally modulated laser. Panel (a): (on - off) / off spectra using 5-minute scan lengths. Each spectrum consists of 5 pairs (50 minutes). Panel (b): Periodogram for each spectrum.

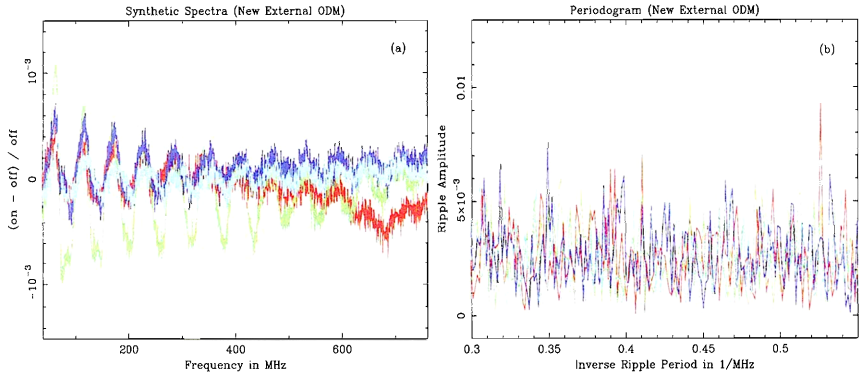

Figure 33: Synthetic spectra using the IF noise source and a new externally modulated laser. Panel (a): (on - off) / off spectra using 5-minute scan lengths. Each spectrum consists of 5 pairs (50 minutes). Panel (b): Periodogram for each spectrum.

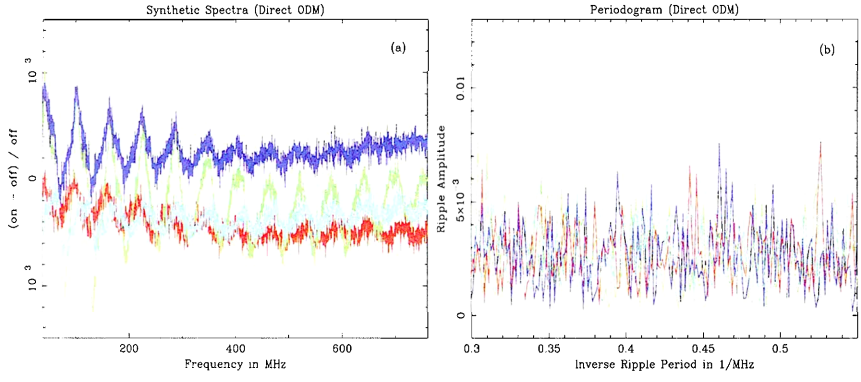

Figure 34: Synthetic spectra using the IF noise source and a directly modulated laser. Panel (a): (on - off) / off spectra using 5-minute scan lengths. Each spectrum consists of 5 pairs (50 minutes). Panel (b): Periodogram for each spectrum.

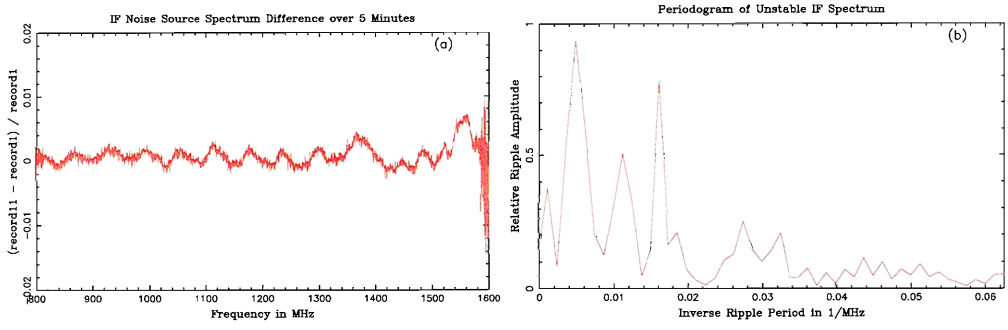

Figure 35: Difference spectrum, (spectrum2 − spectrum1) / spectrum1, of two 30-second integrations on the IF noise source taken 5 minutes apart (a) and its periodogram (b).

4.2 Baseline Periodicities Produced in the IF Electronics

In the process of disentangling the various baseline distortion effects we frequently saw a ripple with a period in the range of 60 to 80 MHz when using the 800 MHz spectrometer bandwidth. The amplitude of this ripple varied irregularly on time scales of minutes, and it was eventually correlated with small temperature changes in the GBT control room where much of the IF electronics is housed. As of this writing the major cause of the problem has been traced to electronic components in one or two of the IF conversion and filter modules, but it appears that there is more than one temperature-sensitive component in the IF chain contributing to baseline instability. Here is what we know thus far.

Figure 35a shows an example of an 800-MHz spectrum when the IF baseline instability is quite prominent. The noise power in this spectrum is from the IF noise source substituted for the GBT receiver's IF output in the GBT Receiver Room. The frequency scale in this figure refers to the IF passband at the input to the spectrometer sampler. The periodogram of this spectrum is shown in Figure 35b. The most notable feature in the periodogram is the spike at 0.016 MHz^{-1} (62-MHz ripple period), but there are other significant periodicities in this spectrum. The largest spike at 0.005 MHz^{-1} (200-MHz ripple period) is hard to interpret since it is a substantial fraction of the total spectrum width.

The correlation of the amplitude of ripples, such as those in Figure 35, with GBT equipment room temperature can be illustrated by plotting the strength of the dominant spike in a spectrum's periodogram as a function of time along with a plot of the measured temperatures in the room and in the rack containing many of the IF electronics modules. This is shown in Figure 36. There is a clear correlation of 62-MHz ripple amplitude with the temperature of the rack containing some of the IF electronics used in this measurement. However, the correlation between temperature and ripple amplitude for other periods seen in the periodograms and between amplitudes of different ripple periods is not always obvious. This indicates that there is more than one cause of the baseline instabilities in the IF system.

Figure 37 shows a summary of the various ripple periods found in the periodograms of $(recordN - record1)$ / $record1$ spectra over roughly a five-hour period, where $recordN$ is the Nth 30-second record in the run. The open boxes in this figure refer to periodogram features that occurred occasionally or weakly, and the filled boxes are for strong features that were present much of the time. Most of the IF channels showed a dominant ripple period around 0.016 MHz^{-1} (63 MHz), but there was significant variation in this period from channel to channel, and these periodogram features tended to be composed of several closely spaced periods whose

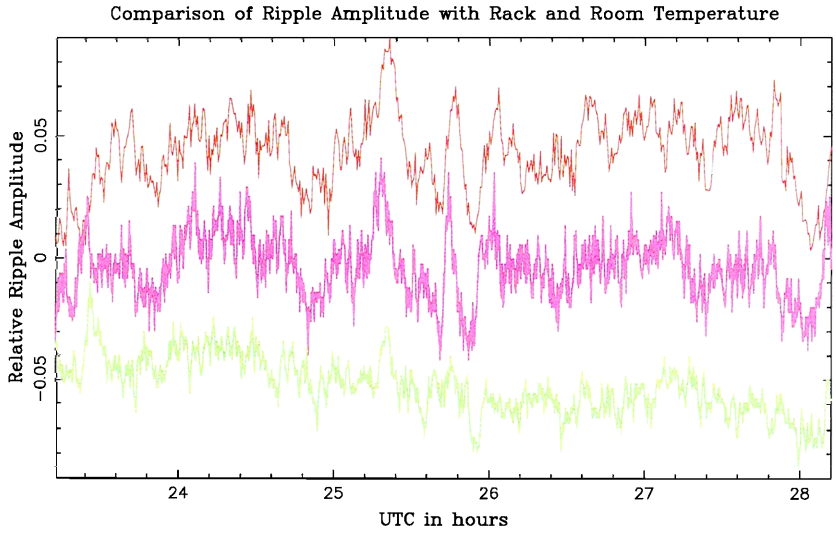

Figure 36: Correlation of the 62-MHz ripple period amplitude in IF channel A1 (top curve) with converter rack A internal air temperature (middle) and GBT equipment room air temperature (bottom). The temperature values have been multiplied by 0.2 and given an arbitrary zero offset to allow easier visual comparison with the ripple amplitude curve.

amplitudes were not necessarily well correlated in time. Channels A2 and C2 were considerably more stable than the others. Most channels had quite a variety of periodicities that came and went with time with only partial correlation. This, too, indicates that there is more than one cause of baseline ripple in each IF channel.

The three rows at the bottom of Figure 37 are the equivalent periodogram distributions for the spectra obtained by differencing spectra taken before and after intentional changes to IF cable lengths at three different places in the IF system. Figure 38 is a schematic diagram of the GBT IF system between the front-end and the spectrometer. There are four cables with lengths between 2.4 and 7.1 meters between the different IF modules. As will be explained in the next section, if there are mismatches at the ends of these cables that cause part of the signal to traverse the lengths of the cables twice again, the multipath interference will cause frequency-dependent gain ripples. Very small changes in the electrical lengths of these cables will cause the gain ripples to change in phase, which can manifest themselves as temperature-dependent gain ripples in the system noise spectrum.

The gain ripple periods corresponding to the 2.4-, 6.5-, and 7.1-meter cable lengths are shown at the bottom of Figure 37 as measured with the cable length change experiment. There may be a strong effect associated with the 2.4-meter cable corresponding to a ripple near 0.016 MHz^{-1} (63 MHz) as seen by the period correlation in Figure 37, but there are no periods evident in the IF noise periodograms corresponding to the other two cable lengths, even though one might expect a comparable or larger temperature sensitivity of the longer cables. As of this writing it is not clear how large a role the temperature dependence of the electrical lengths of these cables plays in the observed IF baseline instability. It is likely that this effect is a significant problem so the procurement of more stable coax is under way.

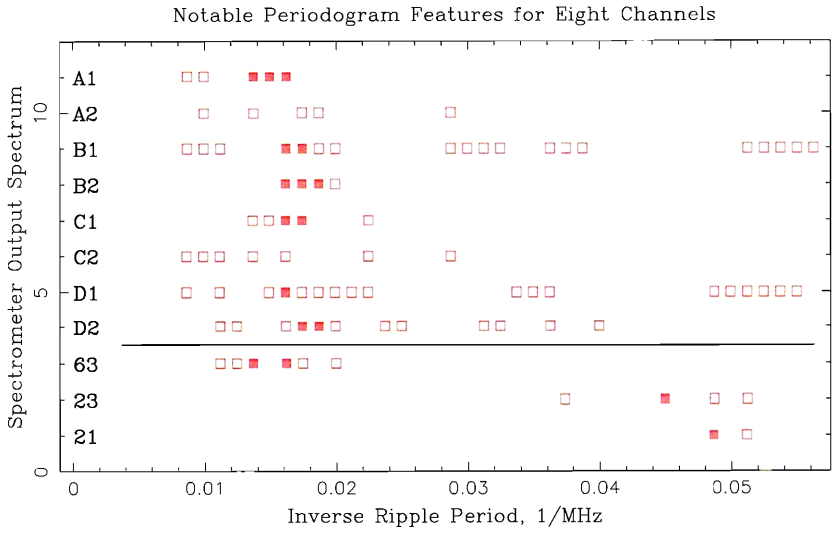

Figure 37: Ripple periods found in the periodograms of eight of the sixteen GBT IF channels for the five-hour run used in Figure 36. The rows are for different IF channels labeled by spectrometer output channel. The bottom three rows show equivalent results for the FFT's of spectra obtained by changing IF cable lengths as reported below. Rows "63", "23", and "21" refer to the 63-, 23-, and 21-MHz ripple periods that are characteristic of the cable lengths given in Figure 38.

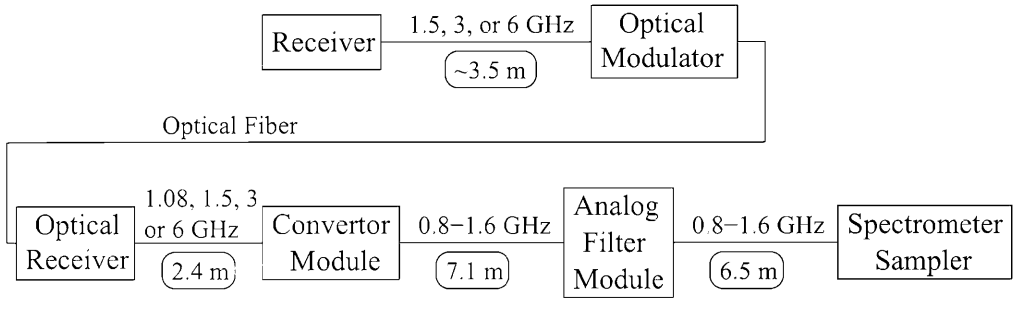

Figure 38: Schematic diagram of one GBT IF channel. The figures in rounded rectangles are cable electrical length in meters. and above each is the frequency range carried by this cable when using the 800 MHz spectrometer bandwidth.

4.3 Changing Cable Lengths

We performed tests on the GBT Equipment Room IF electronics in an attempt to isolate the source of near sinusoidal baseline ripples that show up from time-to-time. We injected a stable noise source into Converter Modules or into Sampler/Filter Modules, and simulated position switched observations by running a series of scans using the spectrometer's 200-MHz bandwidth. During the course of these tests, we induced small changes in the length of coaxial cables connecting various pieces of equipment by inserting short coaxial adapters. This introduced dramatic ripples in the baselines (Figure 39), calculated by the usual methods.

In order to understand this ripple-producing mechanism, it is helpful to revisit some two-port network theory. Figure 40 shows a signal-flow representation of two two-port networks, Net A and Net B, connected by a lossless, matched transmission line. The scattering parameters s_{11} and s_{22} are input and output reflection coefficients of the networks. Parameters s_{21} and s_{12} represent the forward and reverse transmission coefficients. The s-parameters are complex values that, in general, vary with frequency. The delay of the lossless, matched transmission line is represented by a transmission coefficient in phasor notation: $e^{j\beta l}$, where $\beta = 2\pi/\lambda$ and l is the electrical length of the transmission line. In Figure 40, complex voltage signals flowing toward the right are represented by a_i, and signals flowing toward the left by b_i.

We are interested in a_4/a_1. The square of the magnitude of this quantity is the transducer power gain of the cascaded networks. The signal-flow diagram allows us to write equations for the signals leaving and reflected from each port, and after some algebraic manipulation, we arrive at:

$$a_3 = a_1 s_{21A}(1 - s_{11A})e^{j\beta l} + a_3 s_{11B} s_{22A} e^{j2\beta l} \tag{11}$$

and,

$$\frac{a_4}{a_1} = \frac{s_{21A} s_{21B}(1 - s_{11A})(1 - s_{11B})e^{j\beta l}}{1 - s_{22A} s_{11B} e^{j2\beta l}} \tag{12}$$

Equation 11 shows that a_3, the input signal to Net B, consists of the input signal a_1 modified by Net A and delayed by the transmission line, plus a_3 (from an earlier time) reflected by s_{11B} and by s_{22A} and delayed by two passes through the transmission line. It may not be immediately obvious from equation 12, but this dual reflection sets up an interference pattern that introduces gain ripple in the cascaded network frequency response, a well-known result. Numerical evaluations of equation 12 show that:

- The transmission line embedded between non-zero reflection coefficients introduce passband ripple with characteristic frequency of $\frac{c}{2l}$, where c is the velocity of propagation in the line. The ripple amplitude is set by the product of $s22A$ and $s11B$.
- If the line length changes, the passband ripple shifts in frequency. If this happens, say, between (or during) two position-switched scans, the frequency shift in ripple pattern introduces ripple in the baseline obtained by the ratio of the two scans. The amplitude of the baseline ripple is proportional to the length change (for small changes), as a fraction of the wavelength of the signal on the line. For example, simulations show that in order to keep baseline ripple below 0.01% when the transmission line is operating between 20dB return losses, the line electrical length must be stable to better than 0.144° (λ/2500) at the highest passband frequency.

These results may be used to set specifications on the required phase stability of interconnecting cables, based on the return loss seen at each end and on the frequencies present on the

cable. Changes in electrical length of cables may be induced by temperature changes, by flexing, and by poor connections. We can see that the GBT system design has made these requirements quite challenging because of the relatively high frequencies and broad bandwidths used between various subsystems. The following section discusses the types of cables used for long signal runs on the GBT.

4.4 GBT Cables

Three types of coaxial cables are mainly used for IF and RF signals in the GBT receiving systems.

141 Semi-rigid The solid teflon dielectric in these cables exhibits a relatively strong negative temperature coefficient, giving cable assemblies a delay coefficient of about $\rho = 70ppm/C$ near room temperature. Cables made from this material are generally less than 1 meter long. To achieve $\lambda/2500$ stability at 8GHz and 1 meter length, the coefficient implies a temperature stability of just over 0.1°C. The equation for ΔC is:

$$\Delta C \leq \frac{\Delta l}{\rho l} \tag{13}$$

where Δl is the maximum change in cable length that will achieve the required baseline stability.

Heliax FSJ1-50A The polyethylene foam dielectric in this cable has a temperature coefficient much smaller than teflon. Cable assembly temperature coefficients are typically $7 - 12ppm/C$. This type is used in the GBT Receiver Room for IF cables between the front-ends and the IF Rack, and lengths can be 4 meters. To achieve $\lambda/2500$ stability at 8GHz on a 4 meter length of FSJ1-50A, temperature stability of just over 0.3°C is required.

Belden 1673A Conformable Coax This cable uses solid teflon dielectric, and we measure temperature coefficients of $50 - 70ppm/C$. This type is used for jumpers in the Equipment Room. For example, IF jumpers between the Analog Filter Rack and the Spectrometer Sampler Rack are of the 1673A type. These cables are about 6 meters long (electrical) and carry up to 1.6GHz signals. To achieve $\lambda/2500$ stability at 1.6GHz on a 6 meter length of 1673A, temperature stability of 0.09°C is required.

We have measured a few other cable types, and found that one must be cautious about accepting published manufacturer's specifications. For example, type LMR cables by Times Microwave are specified to achieve "less than $10ppm/C$", but our measurements on several samples obtained coefficients of $20 - 25ppm/C$. Tests of a relatively new type, F057A Heliax by Andrews, yielded promising results of -4 to $+5ppm/C$ near room temperature for several assemblies. This type is being adopted for use at several locations in the system.

4.5 IF Converter Rack Ripple

In light of the tight requirements for cable phase stability discussed above, there was expectation that the near 60MHz ripple often seen in the IF system was related to cable stability. In particular, it was found that the cables between the Optical Receivers and the Converter Modules exhibited characteristic ripple frequency near 60MHz. However, extensive testing has shown the situation to be much more subtle and complex. The following summarizes the findings to date:

- The dominant ripple is tightly correlated with the Equipment Room HVAC plenum temperature. By injecting noise sources at various points in the system, the instability has been isolated to the Converter Racks.

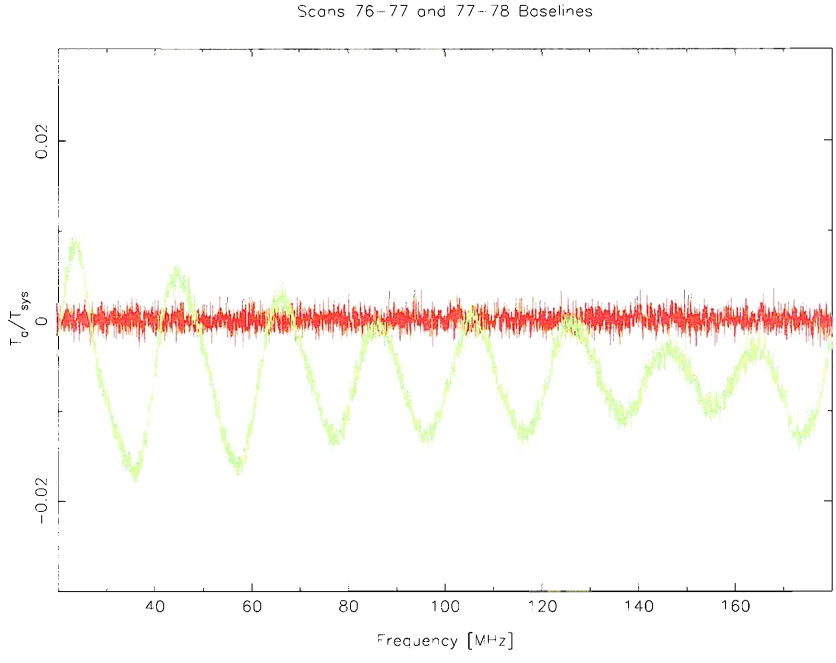

Figure 39: Data taken with the GBT Spectrometer. Baselines are shown for two pairs of scans. Between the scans used to generate the green trace. about 4cm was added to the cable between the Sampler Filter module in the Analog Filter rack and the input to the Spectrometer sampler rack.

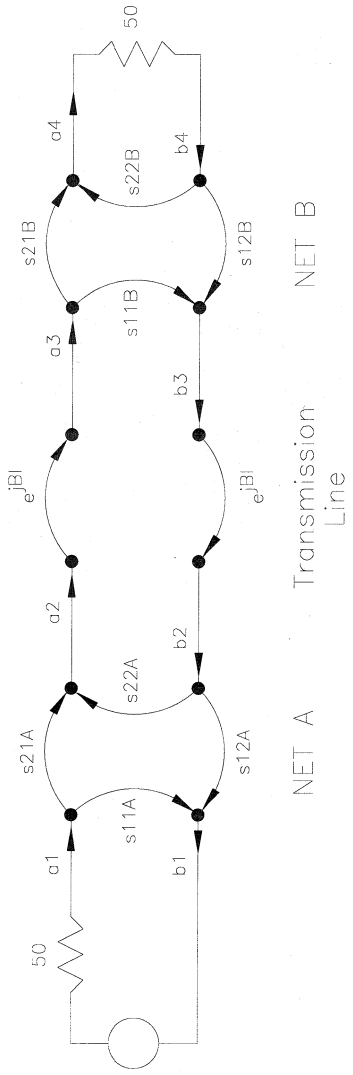

Figure 40: Schematic representation of two networks connected by a lossless, matched transmission line.

- The major ripple period varies by Converter Module between about 55MHz and 65MHz, but is quite stable with time. The ripple period does not exactly match that due to the length of the Optical Receiver to Converter Module cable length.
- The ripple is somehow tied to the 4-way power splitters within the Optical Receivers. We have found that if three of the four OR outputs are terminated, there is no evidence of the ripple for quite long periods. See Figure 41. The 4-way splitters have output-to-output isolation of about 20dB, so another fact is not surprising: a change in the cable length connected to any one of the four outputs, affects gain ripple in all four channels.

A feature of the Converter Module design that may also be a contributing factor has been identified. During lab testing, we found that a change in the LO2 cable length, connecting a Converter Module to the LO2 power splitter, perturbs the module gain response, and introduces a ripple when the gain responses before and after the cable change are ratioed. The ripple period, which in the system is near 60MHz, depends on the length of the LO2 cable. Figure 42 shows the input sections of the Converter Modules, and the associated LO2 connections, which will help explain the effect. MX1 is a triple-balanced broadband mixer which is used to up-convert the IF input signal. Note in this up-conversion application the module input signal is connected to the mixer I port, and the R port is used as the output. The mixer type used has I-L port isolation of only about 19dB at 3GHz. The apparent explanation for the observed behavior is that the module input signal leaks out the mixer L port, flows through the LO isolator (which has less than 10dB loss in both directions at 3GHz), down the LO2 cable, and is reflected at the LO2 power splitter with -7dB return loss. It then reverses the path, and interferes with the original signal. The round trip loss through the path is approximately -55dB. The magnitude of the gain ripple introduced by the small return signal can be calculated by noting that it does a voltage vector addition to the main signal, and the relative phase of the two vectors rotates with frequency. Therefore, the peak-peak gain ripple expressed as a fraction of the main signal is given by:

$$Ripple_{p-p} = 2 * (10^{\frac{RoundTripLoss}{20}}) \tag{14}$$

For -55dB round-trip loss this value becomes 0.4%, near the level seen in the system as the Equipment Room temperature varies.

While we have been successful in identifying several sensitivities in the Converter Racks which can induce ripple, it is still not apparent why the system is so sensitive to temperature. Measurements have failed to identify any of the passive or active components that are particularly sensitive to temperature. Nevertheless, the sensitivities are not good, and because of the channel-to-channel coupling, it is important to reduce the sensitivities in the whole Converter Rack in order to evaluate the effect of any improvement. The plan for proceeding at this point is to install phase stable cables in the Optical Receiver to Converter Module path, and to increase the isolation to the LO2 cables from the signal path. A different type of mixer is being sought, but high isolation and broad bandwidths are generally not mutually compatible. The best way may be to add a LO2 buffer amp near the mixer LO port which should add 30dB or so isolation at the signal frequency. A reasonably priced MMIC amplifier that should work has been identified and will be assembled for evaluation.

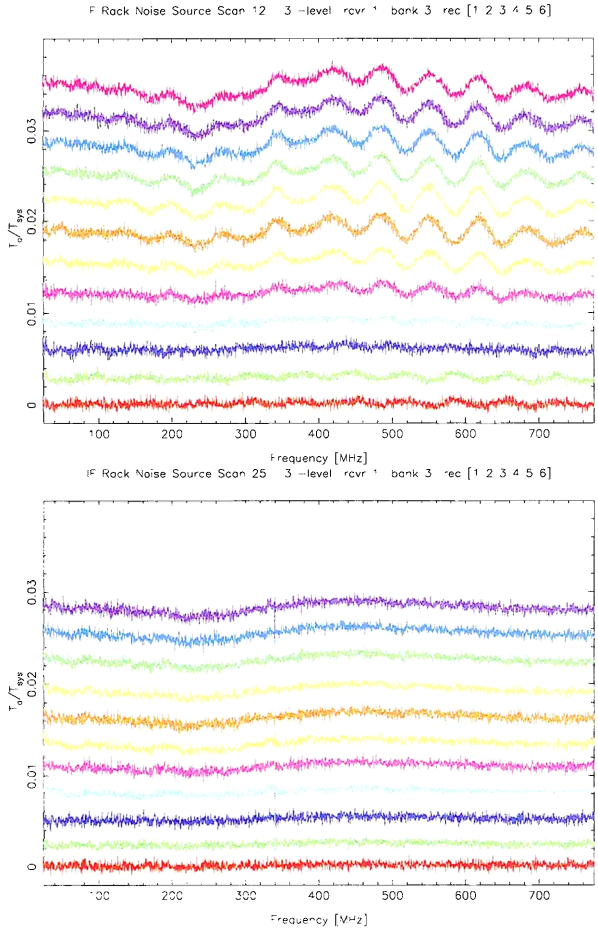

Figure 41: Baselines for two sets of one-minute scans, with the first of each set taken as the reference for the subsequent scans of that set. The IF Rack Noise Source and the OR1/CM3/SF3 IF path were used. The upper panel shows results with optical receiver module 1 (OR1) connected to four Converter Modules as normal. The lower panel shows results immediately afterward when three of the four OR1 outputs were terminated with 50 ohm loads.

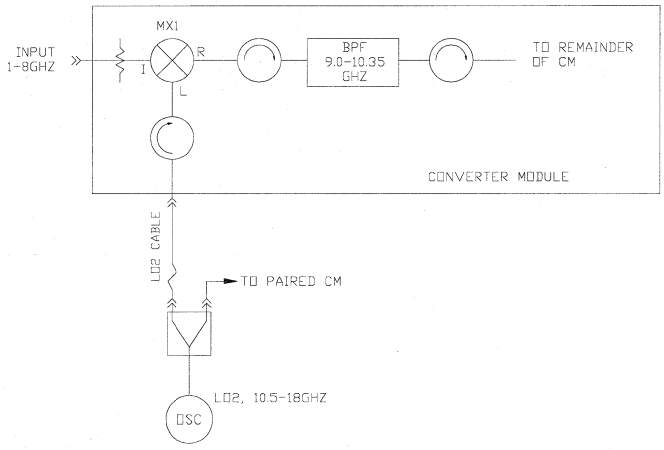

Figure 42: A block diagram of the input portion of the 1-8GHz Converter Modules, and the associated LO2 cabling.

5 Spectrometers

5.1 Spectral processor wide-bandwidth distortions

Initial commissioning observations of the C-band (4–6 GHz) receiver using the spectral processor back-end showed a variation in measured $T_{\rm sys}/T_{\rm cal}$ across the 40-MHz pass-bands which can appear to be a ripple in the $T_{\rm sys}/T_{\rm cal}$ spectrum of a receiver if spectra are concatenated (see Figure 43). The amplitude can be as large as 10% of the system temperature and the ripple appears in both polarizations. This ripple also exists in $(on - off)/off$ spectra. This probably colored some of the early baseline measurements made on several receivers. Using both the spectral processor and the autocorrelation spectrometer has revealed that this ripple resides in the spectral processor.

The magnitude of the ripple is a function of input power level which may indicate that this effect is related to sampler quantization. The wavelength of the ripple matches the spectral processor bandwidth and the amplitude appears to increase with bandwidth. Figure 44 shows spectra using the spectral processor with bandwidths of 40 and 10 MHz. For each panel several spectra are plotted with different input power levels. The narrower bandwidths produce flatter spectra and input power levels around -6 dBm appear to be optimum. This phenomena was probably not detected earlier in astronomical measurements since the spectral processor has primarily been used with narrow bandwidths in spectral line mode.

5.2 Autocorrelator linearity tests

Since the GBT autocorrelation spectrometer is the key measurement instrument for this spectral baseline investigation one would like to have a measure of its stability and linearity. Thus far we have no evidence that spectrometer instability (sampler level drift, for example) is contributing to the baseline distortions, but this needs to be revisited after some of the other system instabilities have been improved.

As a first-order check on spectrometer linearity we measured the ratio of T_{src}/T_{sys} for the continuum source 2052+3635 with sampler input levels that differed by 3 dB. The noise power into

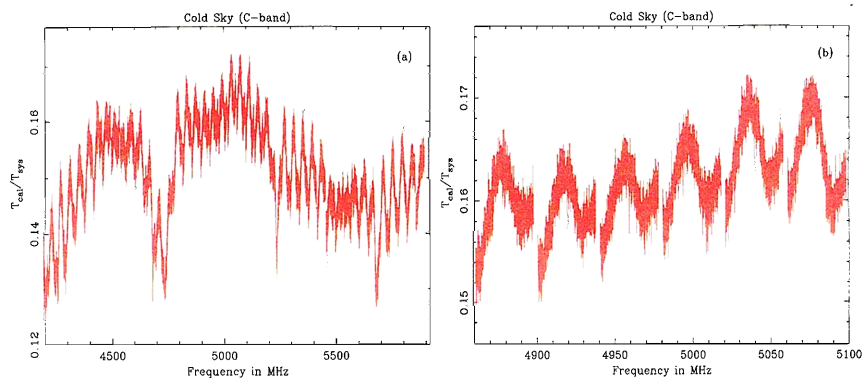

Figure 43: $T_{\rm cal}/T_{\rm sys}$ ratio toward cold sky across the C-band receiver. Only channel X is shown. The spectral processor was used in 2×1024 mode with a bandwidth of 40 MHz. Panel (a) plots the entire band, while panel (b) shows an expanded view.

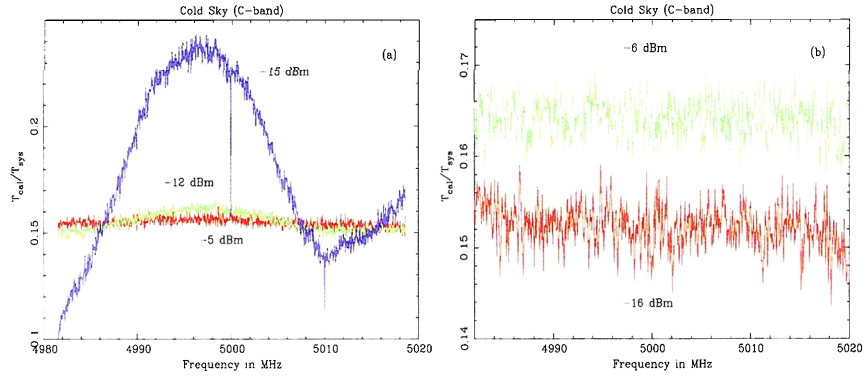

Figure 44: $T_{\rm cal}/T_{\rm sys}$ ratio toward cold sky for the C-band receiver. Only channel X is shown. Panel (a): the spectral processor was used in mode 2×1024 mode with a bandwidth of 40 MHz. The three curves compare different spectral processor attenuator settings. The labels in the plot are the measured power levels. Panel (b): the spectral processor was used in 2×1024 mode with a bandwidth of 10 MHz. The two curves compare different spectral processor attenuator settings. The labels in the plot are the measured power levels. The green or lighter line corresponding to -6 dBm has been offset by 0.01 for clarity.

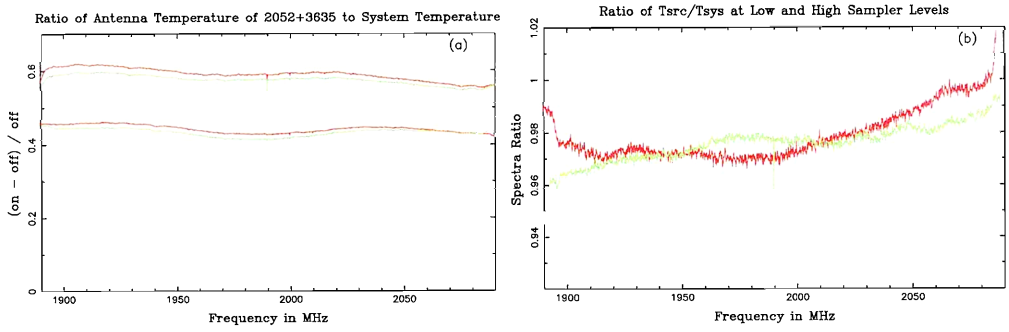

Figure 45: Panel (a): T_{src} / T_{sys} for continuum source 2052+3635 using different spectrometer sampler input levels. Each spectrum is 5 minutes on, 5 minutes off integrations. The red (dark) spectra are for normal sampler input levels and the green (light) spectra are for input levels 3 dB below normal. The lowest two spectra correspond to IF/receiver channel 1, and the top two spectra are for channel 2. Panel (b): ratio of T_{src} / T_{sys} spectra measured with 3 dB lower sampler input levels to spectra with normal sampler levels. The red (dark) curve is for channel 1, and the green (light) curve is for channel 2.

the sampler was changed by adding 3 dB to the computer-controlled attenuators in the converter module shown in Figure 38. The results of this measurement are shown in Figure 45. Simply changing the attenuator settings is enough to change the impedance match to the amplifiers attached to it so one expects some change in the noise spectrum presented to the spectrometer samplers. Nevertheless, the ripple and 2% level change seen in Figure 45 are larger than one would like. The level change could be due to an error in the sampler linearization done in processing the autocorrelation function, or it could indicate that the amplifiers following the changed attenuator are contributing more noise than expected. The ripple suggests that the components surrounding the attenuator are adding a bit of structure to the noise spectrum on frequency scales of 20 MHz and larger.

5.3 Offset problem in assembling composite receiver Tsrc/Tsys spectra

Composite receiver $T_{\rm src}/T_{\rm sys}$ spectra have been produced to investigate spectral baseline effects over the entire receiver bandwidth. The results of these tests are summarized in Figure 46 for L, S, C, and X-band. The spectrometer was used with bandwidths of 50 MHz (L-band), 200 MHz (S-band), and 800 MHz (C and X-band). Composite spectra were produced by overlapping the bandpasses over the receiver's frequency span. The spectra should be reasonably flat since they have been corrected for a measured source spectral index (with the exception of the observations of NGC7027 at C-band). There appear to be significant variations across the band, although this is complicated by the spectral baseline structure.

For all receivers there is an offset between adjacent bands as much as 10% of the system noise. Possible explanations include changes in the system temperature, gain drift, and pointing. Because the source intensity is being plotted in units of the system temperature, any changes in the system temperature would result in an offset between spectra. Typically the spectra were taken consecutively: although changes in the atmosphere could significantly alter the system temperatures at C and X-band this is unlikely at L and S-band. It seems unlikely that the gain would drift between successive observations. During these observations the pointing was not always carefully monitored. Again, while this might be significant at C and X-band, where the

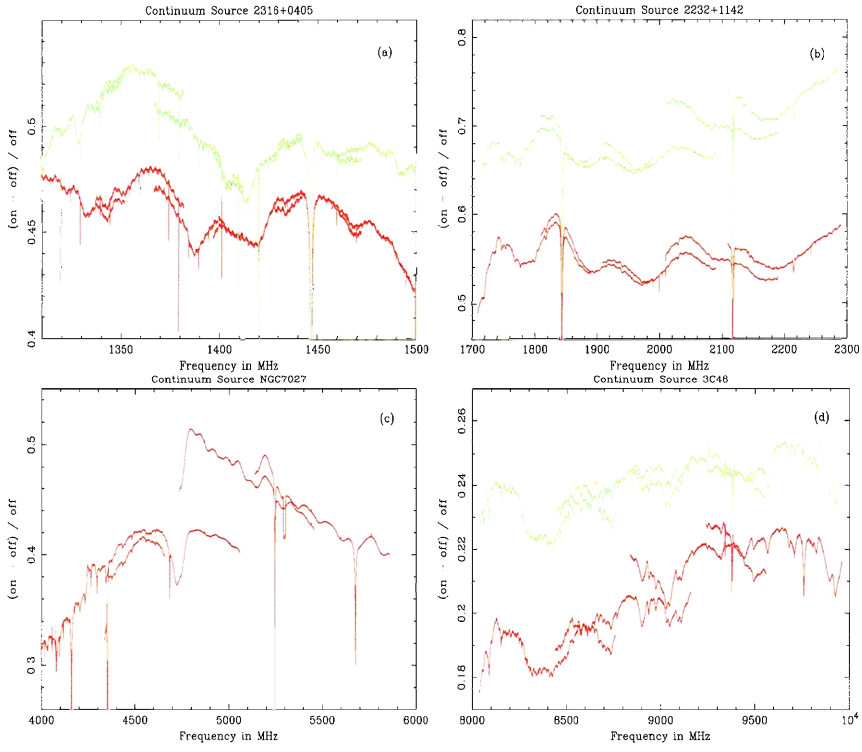

Figure 46: Composite receiver $T_{\rm src}/T_{\rm sys}$ spectra. The red, darker lines are channel X (LCP), while the green, lighter lines are channel Y (RCP). Panel (a): composite spectra for L-band with bandwidths of 50 MHz. Panel (b): composite spectra for S-band with bandwidths of 200 MHz. Panel (c): composite spectra for C-band with bandwidths of 800 MHz. Channel Y was was not usable. Panel (d): composite spectra for X-band with bandwidths of 800 MHz. Spectra in panels (a), (b), and (d) have been corrected for a source spectral indices of -1.006, -0.7, and -0.9, respectively. For the spectra in panel (c) the thermal spectrum of NGC7027 peaks between 5000 and 8000 MHz.

beam-size can be as small as 80 arcsec, it is unlikely to effect the observations at L and S-band. Further investigation is required.

6 RFI

Broadband RFI is another source of spectral baseline distortions. The RFI noise source itself may have a rough spectrum, and the path-loss through which it enters the GBT feed will usually be quite frequency dependent. Figure 47 shows two examples of RFI spectra recorded near 1.4 GHz in the course of observing HI in external galaxies. Figure 47a shows a burst that occurs irregularly about once per hour and lasts only a few seconds. A few of these bursts have been seen with the digital continuum receiver using a detector at the output of the IF Rack where the signal enters the optical fiber. Hence, this is not a problem in the IF electronics or spectrometer. The short duration and recurrence of these bursts suggest something like a thermostat contact arc. Figure 47b shows a burst that lasted about two minutes. In the five, 30-second integration

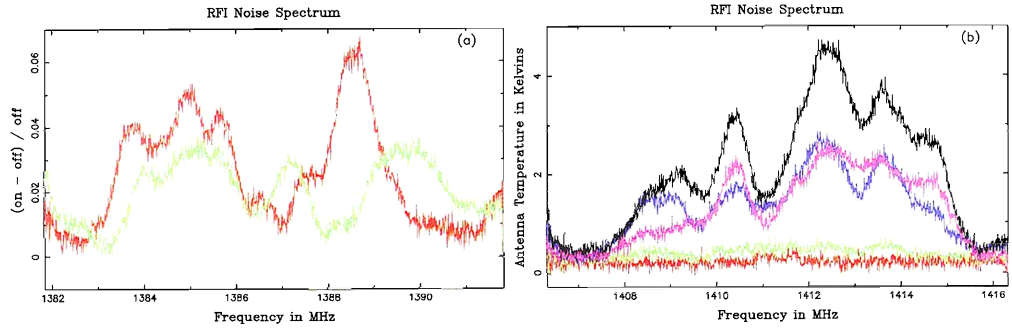

Figure 47: Broadband RFI spectra. Panel (a): (record2 - record1) / record1 for two adjacent 30-second records. This RFI burst lasted less than a few seconds. The red (dark) spectrum is for receiver channel X and green (light) is channel Y. Panel (b): Five successive channel X $T_{sys} * (on - off)/off$ 30-second spectra. The spectrum time sequence is red, green, dark-blue, black, and violet.

spectra one can see a gradual increase and decline in the RFI noise power and change in the spectrum shape. The origins of these two RFI signals remain to be determined.

7 Summary

The spectral baseline properties of the Green Bank Telescope (GBT) have been explored through a series of experiments with the goal of providing a guide to engineering improvements and calibration techniques. The individual reports can be found at:

`http://www.gb.nrao.edu/GBT/baseline/index.html`.

This memo summarizes the current status of the investigation of the GBT spectral baseline properties. The main results are discussed below.

• *Antenna:* The main culprit in producing poor spectral baselines for traditional on-axis single-dish telescopes is multi-path reflections between the feed, sub-reflector, and main reflector of the antenna. The off-axis design of the GBT was primarily motivated to minimize these effects, and, indeed, it does have significantly reduced multi-path interference. Nevertheless, several spectral baseline ripples were detected with the GBT involving the antenna. Quasi-sinusoidal ripples were observed toward cold sky with periods of $\sim$ 1.6 MHz and 9 MHz. The 1.6-MHz ripple was spread over a range of periods from 1.3–1.8 MHz and is consistent with noise in the telescope system entering the receiver through two paths: directly and after emission or reflection from the feed area and then scattered from the circumferential gaps between surface panels. The 9-MHz ripple is consistent with the distance between the sub-reflector and the Gregorian feed-horns involving a single reflection. Higher frequency observations have resolved the 9-MHz ripple into several components consistent with multi-path reflections from the sub-reflector to the Receiver Room roof or one of the L, S, or C-band feeds. The amplitude of these ripples vary from 5–50 mK rms at L-band to 2–8 mK rms at X-band. The 9-MHz ripple is roughly three times stronger than the 1.6-MHz ripple. Careful total power, position switching can reduce these amplitudes by a factor of 30.

The antenna response to a continuum radio source reveals a 2.3-MHz ripple period feature that is consistent with a reflection between the sub-reflector and the primary reflector near the axis of

the parent paraboloid. This phenomena is similar to the dominant baseline ripple of traditional on-axis telescopes but is reduced in amplitude for the GBT since the feed under-illuminates this region of the primary surface, and the center of the specular reflection point is off the edge of the reflectors. The ripple amplitude is a function of source continuum intensity and increases as λ^2.

• *Front-end Receiver:* When observing strong continuum sources quasi-periodic ripples are detected that are found to reside upstream of the first LO mixer and downstream of the optics; that is, in the front-end receiver components. The properties of these ripples are different for each receiver, although they appear relatively stable. Ripple periods range from 30–100 MHz with amplitudes as high as 5% of the system noise. Reflections within the feed and waveguide system of the GBT receivers, due to small impedance mismatches, produce ripples in the same way as multi-path interference in the antenna system. Models predict that at least part of the observed spectral baseline structure can be explained by these impedance mismatches.

The baseline ripple observed at C-band was more sinusoidal than for other receivers and had a period of 65 MHz. Experiments revealed that water on the C-band feed radome was the main source of these ripples. This was more prominent at C-band because of the radome design; nonetheless this effect will add a variable component to the baseline structure for all receivers. An effective blower/heater system is required.

In contrast, at X-band the spectral baselines exhibited irregular, narrow features that were more characteristic of resonances than ripples from reflections. Similar structures have been observed before in other receivers. EM modeling along with experiments in the lab indicated that leakage via the thermal gap can produce resonances in the dewar. However, for X-band only one spike near 9.7 GHz was identified with the thermal gap. Close inspection of the X-band feed-horn led to the discovery of several problems: a 0.015 inch gap in the waveguide wall of one joint; several metal chips in the feed-horn corrugations; a non-conductive finish on the aluminum feed-horn joint flange faces; and an oily film between flanges. Corrections to these problems significantly improved the X-band spectral baselines.

Since it is not practical to eliminate all of the distortions to continuum source spectra the remaining effects must be calibrated. One technique is to use an astronomical calibrator similar to the target source to measure the system response. Initial tests have been encouraging but more work is required.

• *IF System:* The IF system is common to all receivers and it is therefore critical to either remove or characterize any spectral baseline problems from this component of the GBT. During the early stages of the GBT commissioning a 2.4-MHz gain ripple was found in the external optical driver modules. The amplitude varied by 5 dB between the different units and was about 8 dB higher at an IF frequency of 1500 MHz than at 6000 MHz. A modified unit from the manufacturer has reduced the ripple amplitude by 17 dB. New units have been ordered.

During the initial baseline tests we frequently detected a ripple with a period between 60–80 MHz. The amplitude of this ripple varied irregularly with time-scales of minutes, and it was eventually correlated with small temperature changes in the racks housing the IF electronics in the GBT equipment room in the lab. Early investigations pointed to the GBT IF cables. Changes in cable length with temperature can induce ripples with periods similar to those observed. Tests of a relatively new cable, F057A Heliax by Andrews, yielded promising results and is being adopted for use at several locations in the system.

However, installation of the new cables did not significantly improve the spectral baselines. The dominant ripple has been isolated to the converter racks with a period between 55–65 MHz that does not exactly match the ripple due to changes in the optical receiver–converter module cable. The ripple is somehow tied to the four-way splitters within the optical receivers. If three of the four optical receiver outputs are terminated there is no evidence of the ripple for long periods of time. A contributing factor appears to be the LO2 cable whereby the input signal leaks out of the mixer port down the LO2 cable and is reflected at the LO2 power splitter. Methods of

providing higher isolation while retaining the required broad bandwidth are being explored.

• *Back-end Detectors:* Spectra taken with both the spectral processor and the spectrometer revealed a 40-MHz ripple in the spectral processor with an amplitude of 10% of the system temperature. The ripple was observed in $T_{\rm sys}/T_{\rm cal}$ and $(on - off)/off$ spectra. The ripple amplitude is a function of input power level and the ripple period matches the spectral processor bandwidth. This may indicate that the effect is related to the sampler quantization.

Since the autocorrelation spectrometer is a key measurement instrument for many of these spectral baselines tests it is important to measure its stability and linearity. There is no evidence that spectrometer instability is contributing to the baseline distortions. A 3 dB change in sampler input level does produce a ripple and a 2% change in level, however. The ripple suggests that the components surrounding the attenuator are adding a bit of structure to the noise spectrum on frequency scales of 20 MHz and larger. The level change could be due to an error in the sampler linearization or it could indicate that the amplifiers following the changed attenuator are contributing more noise than expected. The spectrometer stability and linearity need to be revisited after some of the other system baseline problems have been improved.

8 Attachments

The following memos are attached to this report:

• "A Note on a Possible Explanation of GBT S-Band Receiver Baseline Variability", Marian W. Pospieszalski, 28 January 2003.

• "A First-Order Noise Analyis of the GBT L-Band Receiver Front-End", Richard F. Bradley, 30 January 2003.

A Note on a Possible Explanation of GBT S-Band Receiver Baseline Variability

Marian W. Pospieszalski

28 January 2003

1. Introduction

This short note is to suggest a possible explanation of the baseline variation observed in GBT S-band receiver as reported by Rick Fisher in his memorandum titled "Second Baseline Test of the 2-3 GHz GBT receiver "[1] dated Dec.2, 2003.

The results presented here are not based on any actual measurement of the components of the receiver but only on reasonable assumptions concerning receiver behavior. Therefore, these results only point to a possible line of inquiry that would explain the measured results.

2. Discussion of Measured Results

Fig 11 of [1] presents the plots of ratio $(T_{on}-T_{off})/T_{off}$ versus sky frequency from 1.89 GHz to 2.09 GHz. There are two dominant features in that plot for channel 1. One is a steady decrease in the ratio from about .58 to about .53 with increasing frequency. The other is a sinusoid like variation with about 120 MHz separations between the peaks and the peak-to-peak variation of about .03. We shall discuses here only a possible explanation for the second pattern, although both pattern could be caused by similar phenomena.
It is reasonable to assume the difference in the sky noise in on and off positions not being dependent on the sky frequency in such a narrow frequency range. Consequently, the observed change in the ratio can only be explained by the variation in the system noise temperature T_{off}. Assuming the average system noise of 20 K, the peak–to-peak changes of 1.1 K (.03*20/.555) would explain the observed pattern. It is likely therefore the changes in the receiver noise temperature as referred to the input of the horn are the cause of the observed pattern. A possible explanation for this effect is offered in the next section.

3. Receiver Model

The S-band receiver does not employ isolator between the cryogenic amplifier and OMT. The amplifier is connected directly to the OMT, which in turn is connected to the horn. The question is how big of a discontinuity and how far from the amplifier input could cause the noise temperature variations with values changing by about 1.1 K for frequencies separated by 120 MHz. For the development of a good noise model of the receiver the knowledge of the input return loss (IRL) of the OMT connected to the horn is not sufficient as the location of the discontinuities causing a particular pattern in the IRL

is important. Also the knowledge of the amplifier noise temperature is not sufficient as the knowledge of all four noise parameters of the amplifier as a function of frequency is needed. The purpose of this note is only to show that indeed an interaction of the amplifier and discontinuities in the horn-OMT assembly can in principle produce the observed patterns.
The gain, noise temperature and input return exhibited by a test design of 1.9 to 3.1 GHz cryogenic amplifier using commercial HFET's is shown in Fig.1. The noise temperature of this design in 1.89 GHz to 2.09 GHz is indeed very flat as shown in Fig. 2. The noise temperature of the same amplifier disturbed by a small capacitive discontinuity producing about 20 dB ORL (as seen at amplifier input) placed 44 inches away from amplifier is also plotted in plotted in Fig.2. The schematic of this fictitious arrangement is shown in Fig.3. This small discontinuity, even in absence of any ohmic losses will produce a noise temperature pattern consistent with the one needed for an explanation of the pattern in the baseline.

3. Discussion.

It should be stressed again that the explanation of one of the patterns in the baseline is based on a fictitious model. A simple test whether the described scenario offers a plausible explanation for this particular receiver would be to measure the receiver noise temperature variation over similar bandwidth with sufficiently small IF bandwidth. Due to the size of the horn it may be a difficult task. Creating a good model would require the knowledge of four noise parameter of the amplifiers and the two–port parameters of the horn–OMT assembly. By the latter it is understood that one port should be defined at some reference plane in front of the horn for one polarization and the other at one of the outputs of the OMT. If there exist a dominant reflection in the horn-OMT assembly and the location of the cause of this reflection is known then again with the knowledge of four noise parameters of the amplifiers a good model can likely be developed. Certainly, the use of an isolator or balanced amplifier instead of an unbalanced version would in principle greatly reduce the sensitivity of the receiver noise temperature to residual reflections at the input [2], [3].

4. References

1.Rick Fisher "Second Baseline Test of the 2-3 GHz GBT receiver " Memorandum dated Dec.2, 2003.
2. M. W. Pospieszalski, "On the Noise Parameters of Isolator and Receiver with Isolator at the Input," *IEEE Trans. Microwave Theory & Tech.*, vol. MTT-34, pp. 451-453, April 1986.
3. A.R. Kerr, "On the Noise Properties of Balanced Amplifiers", *IEEE Microwave and Guided Wave Letters*, Vol. MGWL-8, pp.390-392, November 1998

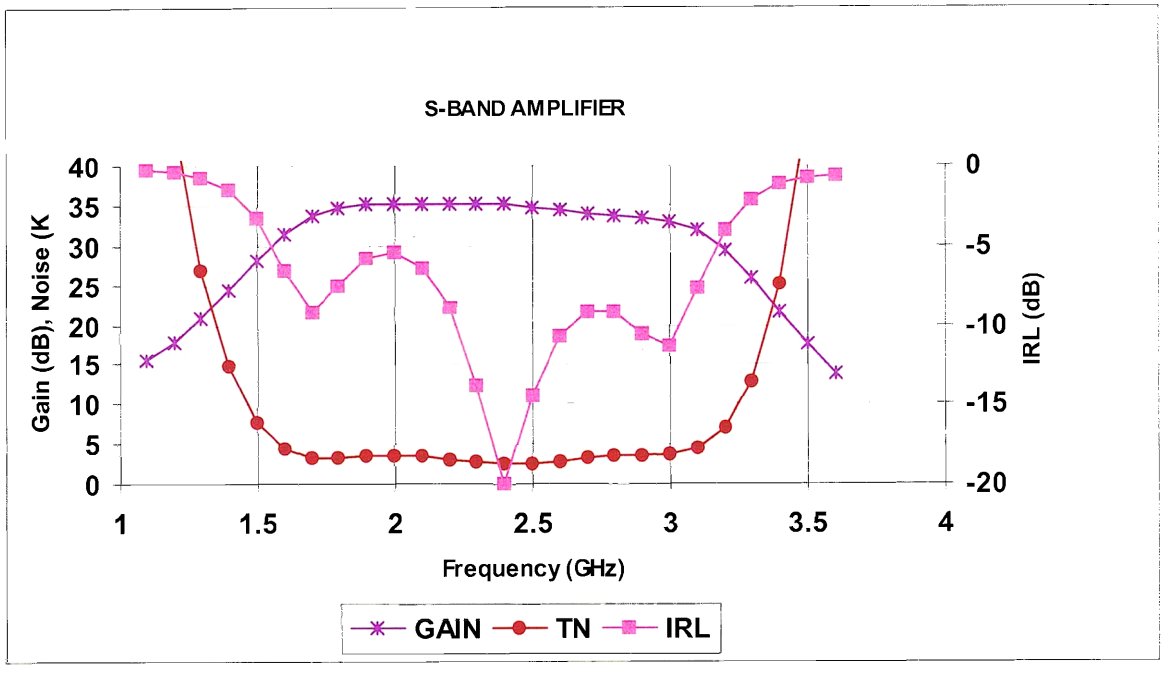

Fig. 1. Gain, noise temperature and input return exhibited by a test design of 1.9 to 3.1 GHz cryogenic amplifier using commercial HFET's.

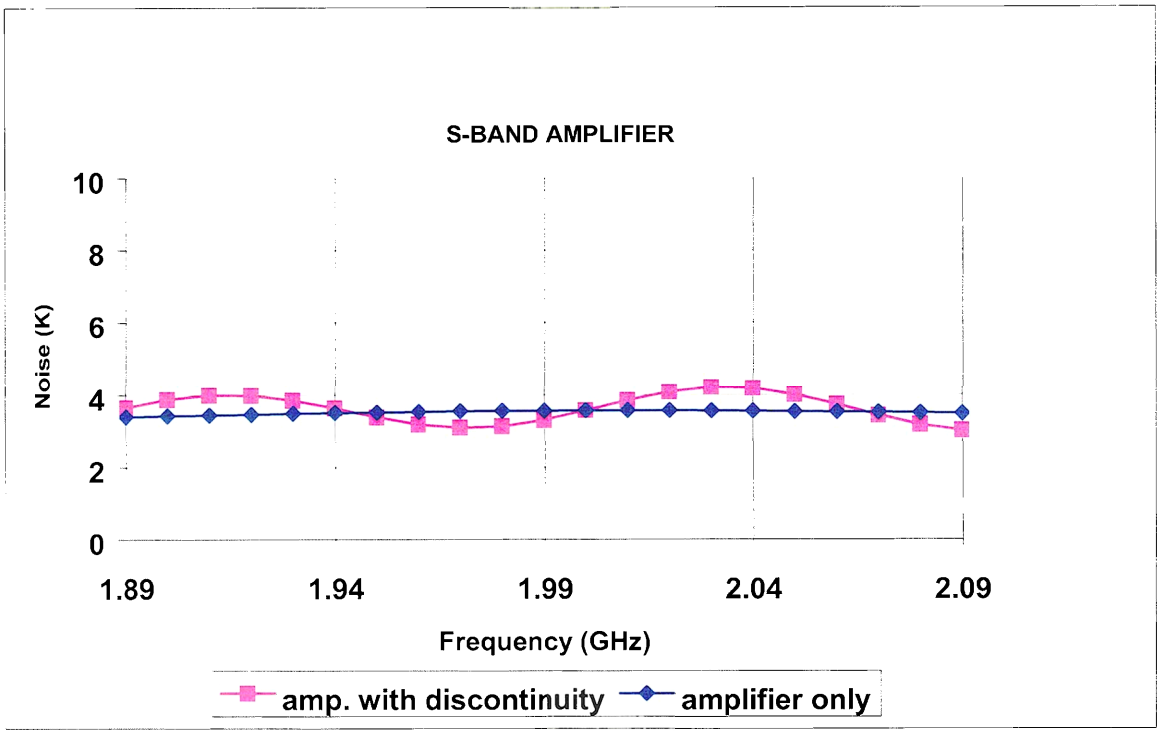

Fig.2. Noise temperature of the design of Fig.1 in 1.89 GHz to 2.09 GHz frequency range with and without a small capacitive discontinuity placed 44 inches (in air) away from the amplifier as shown in Fig 3.

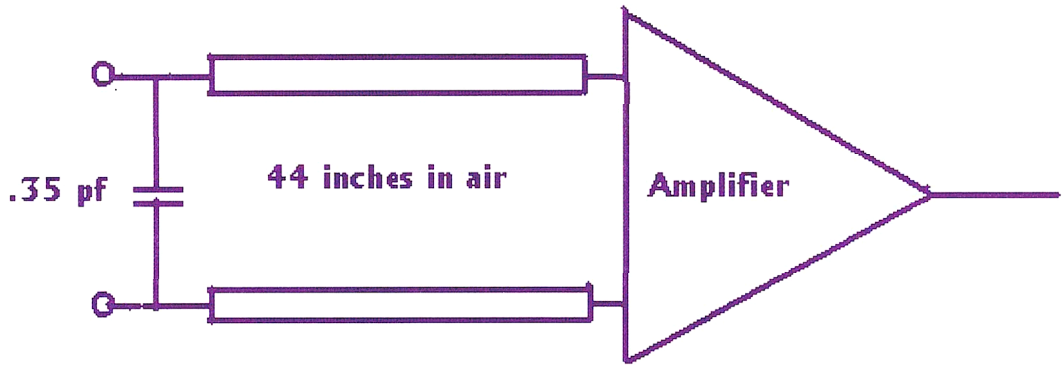

Fig.3 Schematic of the amplifier with capacitive discontinuity, which produces a pattern in noise temperature as shown in Fig 2. The characteristic impedance of the line connecting .35 pF capacitor with the amplifier is 50 ohms.

A First-Order Noise Analysis of the GBT L-Band Receiver Front-End

Richard F. Bradley

January 30, 2003

Introduction

Recent investigations of GBT baselines associated with observations of continuum radio sources have revealed the presence of several frequency dependent anomalies in the spectra produced by traditional calibration and normalization practices [1, 2, 3]. The (sig - ref) / ref formulation, where "sig" is the signal produced at the receiver's output when the telescope is pointing on source and "ref" is the corresponding signal when the telescope is pointing off source, indicates overall large-scale frequency structure as well as periodic, small-scale frequency structure. These structures are present in the L-, C-, and X-band receivers that were evaluated during the commissioning process, and it may well be present at other bands. Through a series of tests performed by R. Fisher and R. Norrod, the cause of this spectral anomaly within the GBT instrumentation has been localized to being ahead of the first mixer in the receiver's RF component chain. It was agreed that first-order modeling and simulation of this cascaded microwave network was necessary to begin to understand the origin of this phenomenon so that corrective action can be taken.

L-band was chosen for the simulation since a well-understood equivalent circuit model is available for the low-noise amplifier used in this band. A block diagram of the RF front-end components of the L-band receiver are shown in Fig. 1. The RF components at a physical temperature of 300 K include the feed, interconnecting waveguide, dewar vacuum seal, and a section of the thermal gap. At 15 K, there is another section of the thermal gap, the ortho-mode transition (OMT), calibration coupler, and low noise amplifier. The system noise temperature of this receiver on the GBT was measured to be approximately 18.5 K. A rough estimate of the noise budget [4] assigns 5 K for atmosphere and CMBR, 5 K for spillover, 4-5 K for the feed, window, OMT, and coupler cascade, and 3-4 K for the low nosie amplifier. The feed length is about 3.3 meters [4] yielding a total electrical length from amplifier to the feed aperture of about 4 meters [4].

A typical composite Tsource / Tsys spectra from 1300-1500 MHz for a continuum radio source taken with the GBT [3] is shown in Fig. 2. These spectra are illustrative of the typical frequency structure encountered in GBT baselines. There is an overall slope across this band together with a sinusoidal-like variation. It is these structures that will be addressed with the simulation and modeling described here. In addition, the spectra shows some very small-scale structure that is believed to be caused by the telescope's optics [5] along with know negative-going interference spikes [5]. Both of these structures reside outside the scope of this study.

Noise Theory

In order to obtain a rough estimate of the various noise contributions within a microwave network, it is common practice to model the loss as merely a perfectly matched attenuator that generates noise proportional to its physical temperature, as described by equation. 7-55a on p. 291 of Kraus [6]. This approach yields a quantity that is actually the *minimum* equivalent noise temperature, Tmin, of the matched lossy component. Implicit in this model is the assumption that the noise waves emanating from the two ports of the attenuator are statistically independent. This is usually not the case in practice.

The complex two-port noise model, which is defined by four noise parameters, is a more complete model of the noise properties of an RF component [7, 8]. A derivation of this noise model is given in Appendix A, but it can be summarized as

$$T_n = T_{MIN} + \frac{T_{REF} G_n}{R_S} \left| Z_S - Z_{opt} \right|^2 , \qquad \textbf{(1)}$$

where Tmin is the minimum noise temperature of the network, Gn is the noise conductance, Zopt=Ropt+jXopt is the optimum noise impedance, and Zs = Rs+jXs is the impedance presented to the input of the attenuator. Tref = 290 K. This equation shows that the amount of noise power as a function of frequency that flows out of the output port of the lossy two-port network will depend on the *complex circuit impedance* that terminates the component's input port. Note that the second term is a positive going quadratic function of the difference between the input impedance and the optimum noise impedance. This function is centered about the optimum noise impedance.

Component Models

The approach adopted here for modeling the frequency behavior of the L-band front-end is to first develop a suitable equivalent circuit and noise model for each of the critical components in the RF signal path that are thought to be contributing to the varying baseline phenomenon. A circuit simulator, namely Agilent's Advanced Design System (ADS), was used to determine the RF network behavior and calculate (sig - ref) / ref in order to emulate GBT observations. Three critical network element have been identified: 1) basic circuit loss, 2) the cascade comprised of the feed, dewar waveguide transition, and OMT, and 3) the low noise amplifier. Details of each component are given below.

Basic Circuit Loss

The noisy elements within the network are assumed to be generated by discrete losses that can be modeled by a pi-type attenuator pad made from individual ADS resistor models. A careful study of the behavior of the overall circuit model under various conditions confirmed that it was indeed functioning as a complex two-port noise model. Two attenuators were chosen to illustrate the differences between the perfectly matched model and the full complex two-port noise model. In both cases, the attenuators were designed for 0.1 dB power loss using the hyperbolic formulae

given in [9] and are at a physical temperature of 300 K. Attenuator #1 was designed to perfectly match the embedding network impedance of 50 ohms. Attenuator #2 was designed for 100 ohms but used in the same 50 ohm embedding network as attenuator #1. This situation could represent a loss element whose optimum noise resistance differs significantly from the network impedance. The results of the ADS simulations are summarized in Table 1.

Table 1 ADS simulation results for the two attenuators described in the text.

Zatt [ohms]	|S21| [dB]	|S11| [dB]	Tn [K]	Tmin [K]	Ropt [ohms]	Xopt [ohms]	Gn [mS]
50	-0.099	-125	6.991	6.99	50	0	0.238
100	-0.125	-41	8.719	6.99	100	0	0.119

Note that if |S21| is used to predict the noise contribution we would calculate 6.92 K for attenuator #1 and 8.76 K for attenuator #2 which is quite close to Tn. However, we completely miss the fact that Tn is not equal to Tmin for attenuator #2. The extra 1.73 K is actually coming from the second term in Eqn. 1.

In order to gauge the effect of the second term in Eqn. 1, an ADS simulation was carried out on the two attenuators for the condition of a varying input impedance, with Rs ranging from 45 - 55 ohms and Xs ranging from -5 to +5 ohms. The results are plotted in Fig. 3. The noise temperature of both attenuators is a relatively weak function of the input reactance since both have Xopt = 0 ohms. The -5 to +5 ohms variation about the optimum reactance produced only a 0.5% or less increase in the noise temperature. However, the effect of varying the input resistance is more pronounced. For Attenuator #1, the ± 5 ohm variation around 50 ohms (which is also Ropt in this case) produced only a 0.5% increase in Tn above Tmin. On the other hand, Attenuator #2, whose optimum noise resistance is 100 ohms, produced a ± 6% variation in Tn about the value at 50 ohms.

Feed, dewar transition, and OMT cascade

Reflectrometry measurements of the feed, dewar transition, and OMT cascade were made by S. Srikanth [10] and are reproduced in Fig. 4. These measurements indicate reflections at the -25 to -30 dB level across the mid portion of the band. It was decided that a detailed model of this network was unnecessary at this time in favor of a simplified network consisting of a cascade of several 50 ohm transmission lines with small-value capacitors placed in shunt at each of the junction points, as illustrated in Fig. 5. The lines were modeled as lossless components so that a given amount of circuit loss could be inserted at various locations along the line to study the effects. AST was used to calculate the level and periodicity of these reflections as a function of shunt capacitance and line length. These parameters were adjusted until a first-order fit at mid-band was obtained between the model and the measured data. The calculated |S11| and terminal impedances are shown in Fig. 6

This lossless network was then placed ahead of the an attenuator as shown in Fig. 7. The attenuator was modeled as described in the previous section with both types being considered. A plot of the noise temperature versus frequency for the cascaded network is shown in Fig. 8. Note that in both cases the impedance variation presented to the input of the attenuator translates to noise temperature fluctuations for the attenuator. These fluctuation are much more pronounced for attenuator #2 (Zopt = 100 ohms) which is consistent with the noise model.

Low noise amplifier

The amplifier used in the GBT L-band receiver is a three-stage, single-ended design created by Gallego and Pospieszalski [11]. The three HFET's are type FHR02X that were manufactured by Fujitsu. An equivalent circuit model for the HFET is shown in Fig. 9. A block diagram of the amplifier is given in Fig. 10. Basic capacitor models were used in place of the more complete equivalent circuit models for the chip capacitors for this simulation. ADS was used to simulate the performance of this amplifier with input and output ports terminated in 50 + j0 ohms. The calculated S-parameters are shown in Fig. 11. Calculated noise parameters are given in Fig. 12.

The input impedance presented to the amplifier was systematically varied over the range $45 < Rin < 55$ ohms and $-5 < Xin < +5$ ohms and the noise temperature at 1.4 and 1.7 GHz was calculated. The results are presented in Fig. 13.

Front-End Configurations and Simulation Results

Several ADS simulations were performed to gain an understanding of the frequency structure observed in [Ton - Toff] / Toff for continuum radio sources. In all simulations, the characteristic impedance of the network was 50 ohms and an ADS two-port noise source model, perfectly matched to 50 ohms, was used to emulate a frequency independent antenna temperature for both on and off source conditions. Two identical networks, one with Ta(on) and one with Ta(off) were analyzed simultaneously so that the [Ton - Toff] / Toff could be easily calculated. Details of the individual simulations together with their results are presented below. Note that receiver gain drifts are not modeled here and that a perfectly stable receiver is assumed.

Large Scale, Non-Periodic Frequency Structure

The first simulation was designed to examine the origins of the large-scale frequency structure. It was hypothesized that this structure was a consequence of amplifier noise. The network, a block diagram of which is shown in Fig. 14, consisted of the antenna temperature noise source followed by the amplifier model. Ta(off) was 5 K while Ta(on) was varied from 0 - 10 K in steps of 2 K. The results are shown in Fig. 15. These data are presented graphically in two columns. The left hand column shows the on-source noise temperature T(on), off-source noise temperature T(off), [T(on) - T(off)], and [T(on) - T(off)] / T(off) for the network operating over the 1.0 - 2.0 GHz band. The right hand column shows the same sequence for a bandwidth of 40 MHz near 1.4 GHz.

These plots clearly show the frequency structure of the amplifier noise is carried through to the [T(on) - T(off)] / T(off) due to the use of this frequency dependent normalizing factor, T(off). Its

effect is a function of antenna temperature. In addition, the narrow band formulation indicates just how such broad band structure could have been easily hidden in past observations. This effect is not indicative of an inherent receiver problem, but a calibration and normalization issue that will affect observing technique. Note that receiver gain drifts are not modeled here and that a perfectly stable receiver is assumed.

Small Scale, Periodic Frequency Structure

The second simulation was designed to examine the origins of the small-scale, periodic frequency structure. The network consisted on the antenna temperature noise source, followed by the shunt capacitor loaded transmission lines, and the amplifier. Transmission line length Len2 was increased to 1000 cm to enhance the frequency variation for visualization purposes only. The results are presented in Fig. 16. The left hand column shows the on-source noise temperature T(on), off-source noise temperature T(off), [T(on) - T(off)], and [T(on) - T(off)] / T(off) for the network operating over the 1.3 - 1.5 GHz band. The right hand column shows on-source noise temperature T(on), off-source noise temperature T(off), and [T(on) - T(off)] / T(off) for the same network operating over a 40 MHz bandwidth near 1.4 GHz. In addition, |S11| for the transmission line section only is shown. Note that in this case, 9.5 K had to be included into Ta for both on and off source to make [T(on) - T(off)] / T(off) comply with GBT observations. In addition, the variation in [T(on) - T(off)] / T(off) is much smaller in amplitude than observed on the GBT but is in agreement with that expected from the amplifier due to impedance variation of the loaded transmission line. The amplitude variation is about the same if we make Len3=1000 cm and Len2=10 cm. These simulations suggest that although the variation in amplifier noise is certainly one component of the noise, there remains another noise mechanism that dominates.

A clue to the other mechanism comes from the 9.5 K needed to artificially raise the system temperature to that of the GBT L-band receiver. The previous simulation suggests that this noise is probably not due to spillover since this component would simply raise the overall noise temperature of the receiver without enhancing the variation we have observed on the GBT. Therefore, the extra noise was removed from Ta, modeled as an attenuator, and placed between the loaded transmission line and the amplifier. Two attenuators were investigated: one designed for Zopt = 50 ohms and the other with Zopt=150 ohms. The physical temperature of the attenuator was set to 300 K since an attenuator at a cryogenic temperature of 15 K would need to have an attenuation of over 2 dB to produce 9.5 K of noise, a situation that doesn't represent the loss measurements. The simulation results are given in Fig. 17 for an 0.1 dB, Zopt = 50 ohms attenuator (Len2 = 1000 cm) and Fig. 18 for an 0.06 dB, Zopt = 150 ohms attenuator (Len2 = 1000 cm). Fig. 19 shows the results for the 0.06 dB, Zopt = 150 ohms attenuator with Len2 = 135 cm. To first order, the results in Fig. 19 are in agreement with the GBT measurements presented in Fig. 2.

Conclusions

As a word of caution, the simulations results and conclusions based on them as presented in this report should be taken as pure speculation until they can be verified through careful experimentation either on the bench or via GBT observations. With that said, there are several conclusions that may be drawn from the simulations:

- The frequency structure observed in the (sig - ref) / ref is not present in (sig – ref) but occurs as a result of the frequency dependence inherent in the ref signal. This effect is not indicative of an inherent receiver problem, but a calibration and normalization issue that will affect observing technique for wide bandwidth applications.

- The large scale, non-periodic structure is probably due to the frequency dependent noise temperature of the low noise amplifier.

- The small-scale, periodic frequency structure is primarily due to noise generated by an ohmic loss at a physical temperature of 300 K located near the OMT end of the microwave network consisting of the feed and the vacuum window / thermal gap. This noise is effected by reflections at the -25 to -30 dB level within the structure. The simulations indicate that the optimum noise impedance for this source differs significantly from the waveguide impedance which causes noise fluctuations with frequency that are on the same scale as that of the found in the GBT baselines. Hence, this mechanism appears tho be the root cause for the frequency structure observed.

- The reflections that occur within the feed, dewar window, thermal gap, and OMT will cause frequency dependent variations in the noise temperature of the low noise amplifier. *However, the amplitude of these variations appear to be too small to account for the size of the variations observed in the GBT baselines.*

- Based on bench measurements and GBT baseline data, the reflections within the feed and vacuum window / thermal gap structure appear to be a result of two or more reflections, with one pair spaced about 135 cm apart.

- The use of an isolator or a balanced amplifier will not affect the primary source of the baseline structure. However, such devices will reduce the gain variations in the amplifier which are a direct result of the multiple reflections. Smoothing the gain variation with frequency should help to improve receiver stability by reducing the receiver's sensitivity to the physical characteristics of the front-end network.

References

[1] Fisher, J.R. “Sample of Baseline Stability of the 2-3 GHz GBT Receiver,” Project TAST_SB_02119, November 19, 2002, NRAO, Dec. 3, 2002.

[2] Fisher, J.R. “Second Baseline Test of the 2-3 GHz GBT Receiver,” Project TBASEJRF021202, December 2, 2002, NRAO, Dec. 3, 2002.

[3] Fisher, J.R. “Further Investigation of L-Band Baselines on Continuum Sources,” Project TBASEDSB021217, December 17, 2002, NRAO, Dec. 23, 2001.

[4] Norrod, R., Private Communication, Jan. 2003.

[5] Fisher, J. R. Private Communication, Jan. 2003.

[6] Kraus, J.D. Radio Astronomy, McGraw-Hill, New York, 1966, p. 291.

[7] Penfield P. and R. P. Rafuse, Varactor Applications, M.I.T. Press, Cambridge, MA. 1962, pp. 21 - 25.

[8] Collin, R. E. Foundations for Microwave Engineering, 2nd Ed. McGraw-Hill, New York, 1992, pp. 766-772.

[9] ITT , Reference Data for Radio Engineers, 6th Ed., Howard W. Sams, Indianapolis, IN, 1975, Ch. 11.

[10] Srikanth, S. Private Communication, Jan, 2003.

[11] Gallego, J. D. and M. W. Pospieszalski, “Design and Performance of Cryogenically-Coolable, Ultra Low-Noise, L-Band Amplifier,” NRAO Electronic Division Internal Report, No. 286, Mar. 1990.

Appendix A

Adopted from lecture notes - Bradley & Fisher, ASTR 535 Introduction to Radio Astronomy Instrumentation, University of Virginia, Spring 2001.

A.1 The Noise Temperature of a Two-Port Network as a Function of its Source Impedance

Consider the noisy two-port network having a complex source impedance, Z_S, at the input as shown in Fig. A.1a. Let's assume for the moment that this impedance has no noise associated with it. Fig. A.1b shows the same network with all of the noise generated within the network represented by its equivalent noise temperature, T_N , which is now associated with the source impedance, Z_S. There is a value of Z_S which minimizes the total noise out of a two-port network. We refer to this optimum value of Z_S as Z_{opt}.

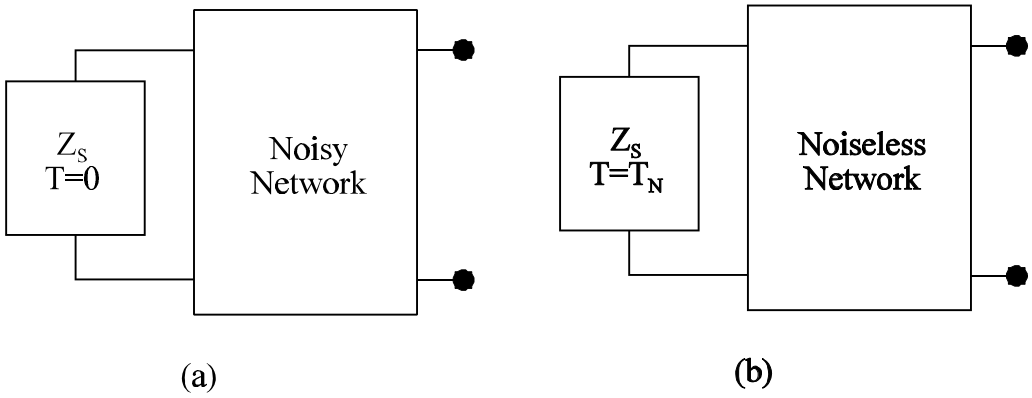

Figure A.1 Noisy network with source impedance Z_S (a) Noisy network. (b) Equivalent noise temperature representation.

Let us compute T_N and Z_{opt} in terms of the parameters of an *equivalent noise model* for the network. We choose the *Rothe-Dahlke Noise Model*, which represents the network of Fig. A.1 by the equivalent circuit shown in Fig. A.2a. This circuit consists of two noise sources: a voltage source, v_n , and a current source, i_n .

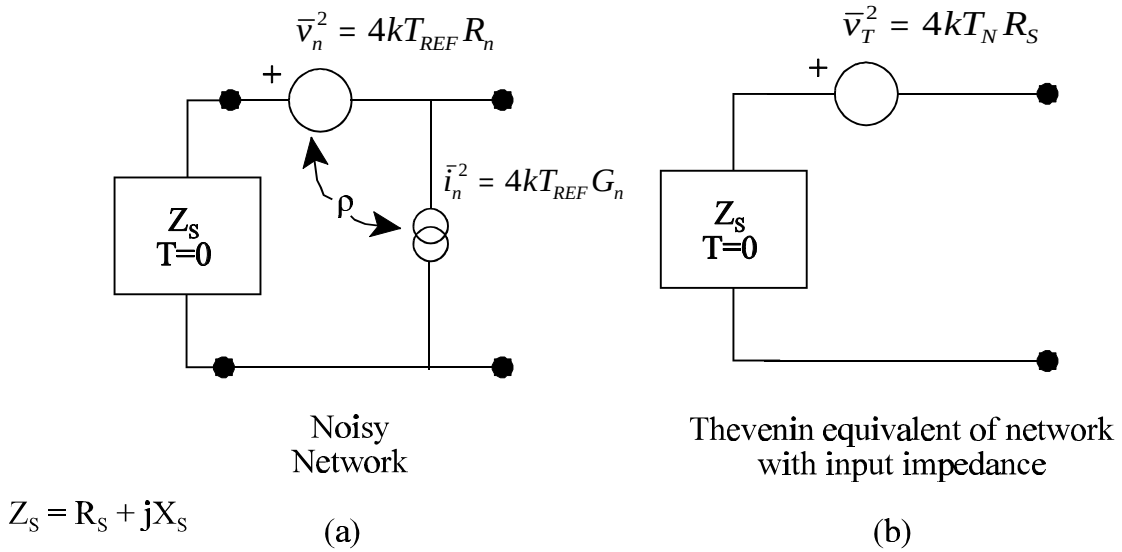

Figure A.2 (a) Noise model of network. (b) Thevenin equivalent circuit.

Two parameters, a resistance and a conductance, associated with these sources may be defined as

$$R_n = \frac{\bar{v}_n^2}{4kT_{REF}} \qquad \textbf{(A.1)}$$

and

$$G_n = \frac{\bar{i}_n^2}{4kT_{REF}}, \qquad \textbf{(A.2)}$$

where T_{REF} = 290 K.

We can treat the noise sources as random variables, and recall that the variance of a random variable is

$$Var[X] = \mathsf{E}[(X - m_X)^2] = \int_{-\infty}^{+\infty} (x - m_X)^2 f_X(x)dx\,. \qquad \textbf{(A.3)}$$

Similarly, we can define the *covariance* of two random variables, in this case v_n and i_n, as

$$\mathrm{cov}[v_n, i_n] = \mathsf{E}\left[(v_n - m_{v_n})(i_n - m_{i_n})\right] \qquad \textbf{(A.4)}$$

Since we can interchange the expected value and summation, and noting that our random variables have zero mean, we can expand Eq. A.4 as

$$\begin{aligned} \mathsf{E}\left[(v_n - m_{v_n})(i_n - m_{i_n})\right] &= \mathsf{E}\left[v_n i_n\right] - m_{v_n}\mathsf{E}\left[i_n\right] - m_{i_n}\mathsf{E}\left[v_n\right] + m_{v_n} m_{i_n} \ , \\ \mathrm{cov}[v_n, i_n] &= \mathsf{E}\left[v_n i_n\right] . \end{aligned} \tag{A.5}$$

Given two random variables, the ratio of the covariance to the product of the standard deviations is the *correlation coefficient, ñ,* such that

$$r = \frac{\mathrm{cov}\left[v_n, i_n\right]}{s_{v_n} s_{i_n}} = \frac{\mathsf{E}\left[v_n i_n\right]}{\sqrt{\mathsf{E}\left[v_n^2\right]\mathsf{E}\left[i_n^2\right]}} \ , \tag{A.6}$$

where we have made use of the fact that both v_n and i_n have zero mean. Note that the correlation coefficient is complex: $\tilde{n} = \tilde{n}_R + j\tilde{n}_I$.

The objective of the calculations that follow is to find T_n as a function of R_n, G_n, $\tilde{n}$, and Z_S that gives identical mean square voltage from both equivalent circuits,

$$\overline{v}_T^2 = \left(v_n + i_n Z_S\right)^2 = \left|\overline{v}_n\right|^2 + \left|\overline{i}_n\right|^2 \left|\overline{Z}_S\right|^2 + 2\,\mathrm{Re}\left\{i_n v_n Z_S\right\} . \tag{A.7}$$

We now substitute the expressions for the voltage and current into Eq. A.7 and solve for T_n / T_{REF} giving

$$\frac{T_n}{T_{REF}} = \frac{R_n}{R_S} + \frac{G_n}{R_S}\left(R_S^2 + X_S^2\right) + \frac{2\sqrt{R_n G_n}}{R_S}\left[r_R R_S - r_I X_S\right] . \tag{A.8}$$

The function $T_n / T_{REF}\,(R_S, X_S)$ is real-valued and the minimum point on the surface defined by this function can be found by setting the gradient equal to zero,

$$\nabla \frac{T_n}{T_{REF}}(R_S, X_S) = \left[\frac{\partial\, T_n/T_{REF}\,(R_S, X_S)}{\partial\, R_S}, \frac{\partial\, T_n/T_{REF}\,(R_S, X_S)}{\partial\, X_S}\right] = \vec{0} . \tag{A.9}$$

First, we begin by taking the partial derivative of Eq. A.8 with respect to X_S giving

$$\frac{\partial\ T_n/T_{REF}\,(R_S, X_S)}{\partial\ X_S} = \frac{2G_n X_S}{R_S} - \frac{2\sqrt{R_n G_n}\, r_I}{R_S} = 0 . \tag{A.10}$$

Solving for $X_S = X_{opt}$ yielding the equation for X_{opt} as

$$X_{opt} = \sqrt{\frac{R_n}{G_n}} r_I \ . \qquad \textbf{(A.11)}$$

Next, we take the partial derivative of Eq. A.8 with respect to R_S giving

$$\frac{\partial \, T_n / T_{REF} \, (R_S, X_S)}{\partial \, R_S} = -\frac{R_n}{R_S^2} + G_n - \frac{G_n X_S^2}{R_S^2} + \frac{2\sqrt{R_n G_n}\, r_I X_S}{R_S^2} = 0 \qquad \textbf{(A.12)}$$

Solving for $R_S^2 = R_{opt}^2$ gives

$$R_{opt}^2 = \frac{R_n}{G_n} + X_S^2 - 2\sqrt{\frac{R_n}{G_n}} r_I X_S \ . \qquad \textbf{(A.13)}$$

Substituting $X_S = X_{opt}$ from Eq. A.11 gives

$$R_{opt}^2 = \frac{R_n}{G_n}\left[1 - r_I^2\right]. \qquad \textbf{(A.14)}$$

We can now determine Z_{opt} from Eqs. A.14 and A.11 as

$$\left|Z_{opt}\right|^2 = \left|R_{opt}\right|^2 + \left|X_{opt}\right|^2 = \frac{R_n}{G_n}\left[1 - r_I^2\right] + \frac{R_n}{G_n} r_I^2 \ ,$$
$$\left|Z_{opt}\right|^2 = \frac{R_n}{G_n} \ . \qquad \textbf{(A.15)}$$

The minimum noise temperature, T_{min}, can be found by substituting R_{opt} and X_{opt} into Eq. A8 giving

$$\frac{T_{MIN}}{T_{REF}} = \frac{R_n}{R_{opt}} + \frac{G_n}{R_{opt}}(R_{opt}^2 + X_{opt}^2) + \frac{2\sqrt{R_n G_n}}{R_{opt}}(r_R R_{opt} - r_I X_{opt}) \ . \qquad \textbf{(A.16)}$$

With a little algebra we can simplify this equation to the following form:

$$T_{MIN} = 2\sqrt{R_n G_n}\left[\sqrt{1 - r_I^2} + r_R\right]T_{REF} \ . \qquad \textbf{(A.17)}$$

Since the function T_n (Z_S) is analytic around the minimum, we can find a compact expression for T_n near T_{MIN} by Taylor series expansion of T_n about the point T_{MIN},

$$\begin{aligned} T_n(Z_S) = {} & T_n(Z_S)\Big|_{Z_S = Z_{opt}} \\ & + \frac{dT_n(Z_S)}{dZ_S}\Bigg|_{Z_S = Z_{opt}} \left|Z_S - Z_{opt}\right| \\ & + \tfrac{1}{2}\frac{d^2T_n(Z_S)}{dZ_S}\Bigg|_{Z_S = Z_{opt}} \left|Z_S - Z_{opt}\right|^2 . \end{aligned} \qquad \textbf{(A.18)}$$

The first term is simply T_{MIN} . The second term is zero since the expansion is about the minimum point. The third term yields,

$$\begin{aligned} \frac{dT_n(Z_S)}{d(Z_S)} &= \frac{2T_{REF}G_n|Z_S|}{R_S} + \frac{2\sqrt{G_n R_n}T_{REF}\,r_R}{R_S}, \\ \frac{d^2T_n(Z_S)}{dZ_S^2} &= \frac{2T_{REF}G_n}{R_S}, \\ \therefore\ \tfrac{1}{2}\frac{d^2T_n(Z_S)}{dZ_S^2}\Bigg|_{Z_S = Z_{opt}} \left|Z_S - Z_{opt}\right|^2 &= \frac{T_{REF}G_n}{R_S}\left|Z_S - Z_{opt}\right|^2 , \end{aligned} \qquad \textbf{(A.19)}$$

or

$$T_n = T_{MIN} + \frac{T_{REF}G_n}{R_S}\left|Z_S - Z_{opt}\right|^2 . \qquad \textbf{(A.20)}$$

If we define the parameter $N = G_n R_{opt}$ then,

$$T_n = T_{MIN} + \frac{NT_{REF}\left|Z_S - Z_{opt}\right|^2}{R_S R_{opt}} . \qquad \textbf{(A.21)}$$

There are a couple of important points to make regarding Eq. A.21. We can now define four parameters associated which the noise generated within any two-port network: T_{MIN}, R_{opt}, X_{opt}, and N. When the source impedance is equal to the optimum noise impedance, the noise temperature of the network is equal to the minimum noise temperature, T_{MIN}. However, if there is a mismatch between Z_S and Z_{opt}, then the noise temperature will always be higher then T_{MIN} and related to the square of the difference between these impedances.

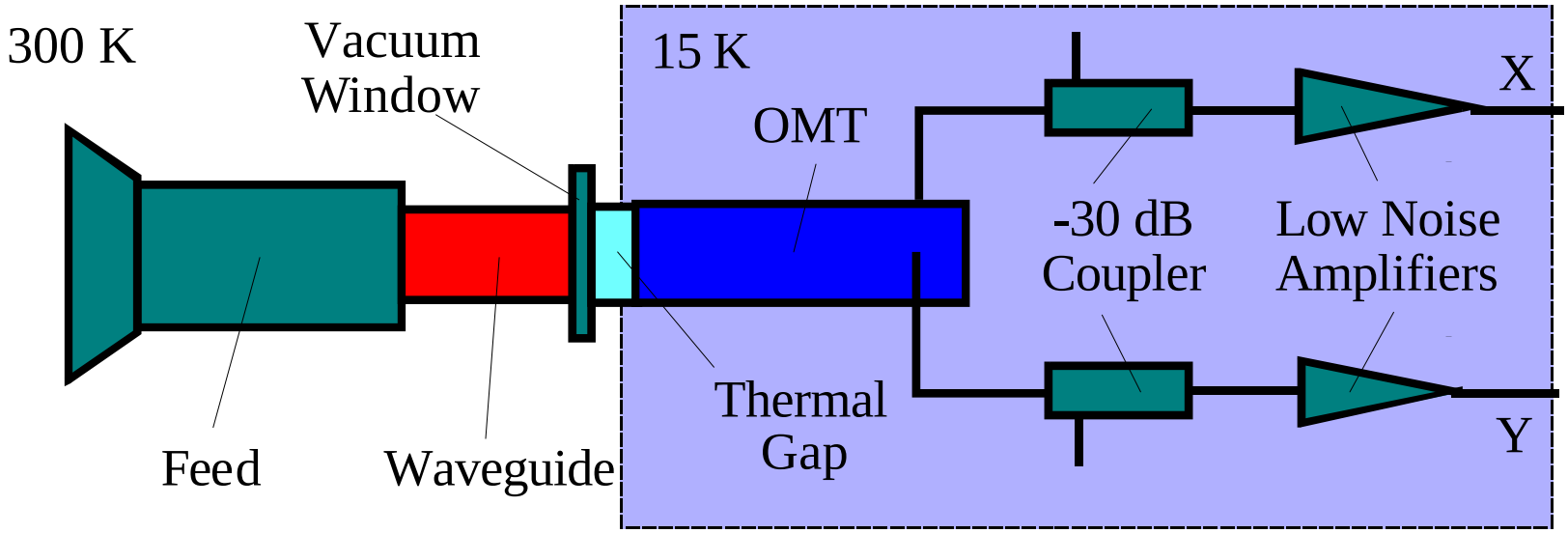

Figure 1 Block diagram of the GBT L-band receiver front-end.

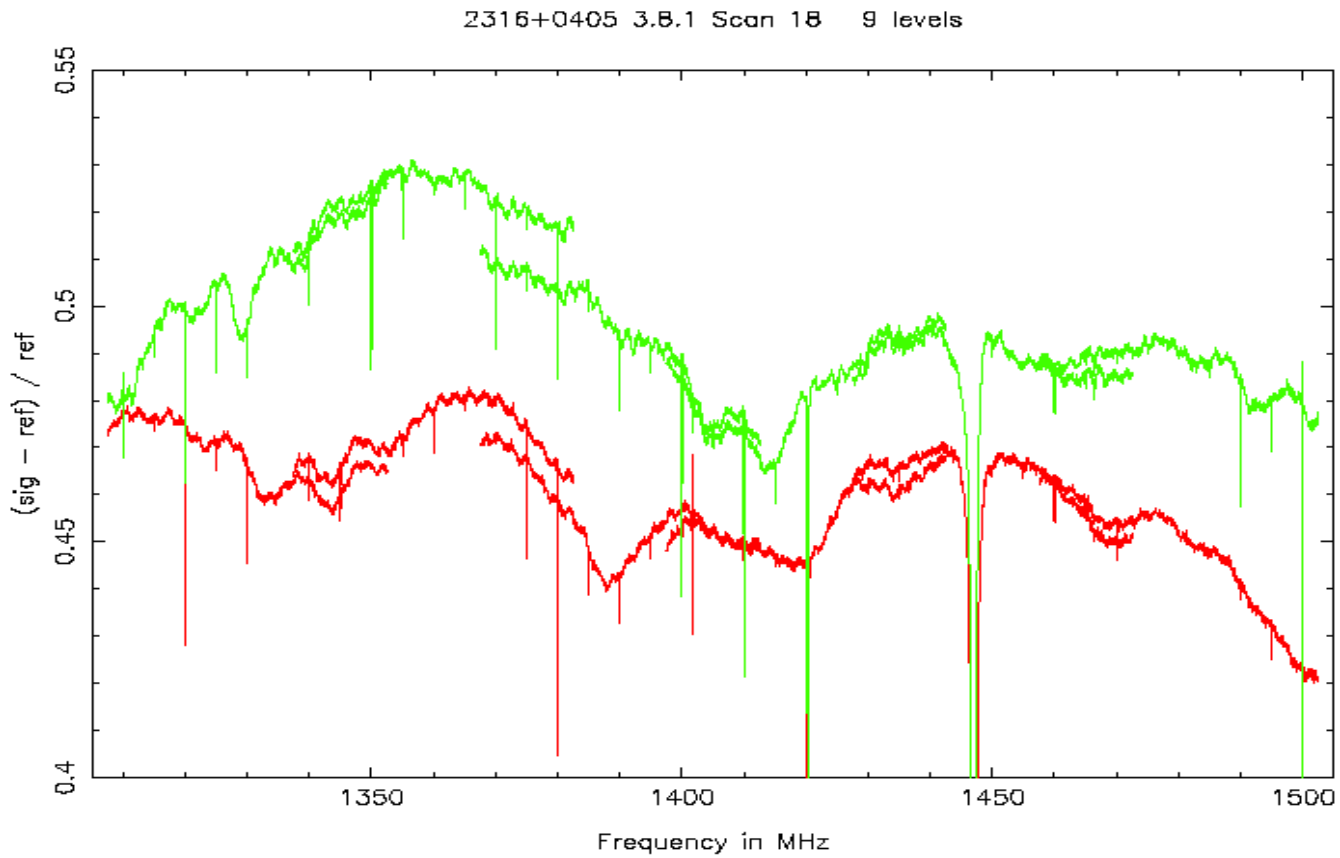

Figure 2 Scans 17-28, composite Tsource / Tsys spectra for the continuum radio source 2316+0405 (S = 4.68 Jy @ 1.4 GHz). Red curves are for receiver channel X and green curves are for channel Y [3].

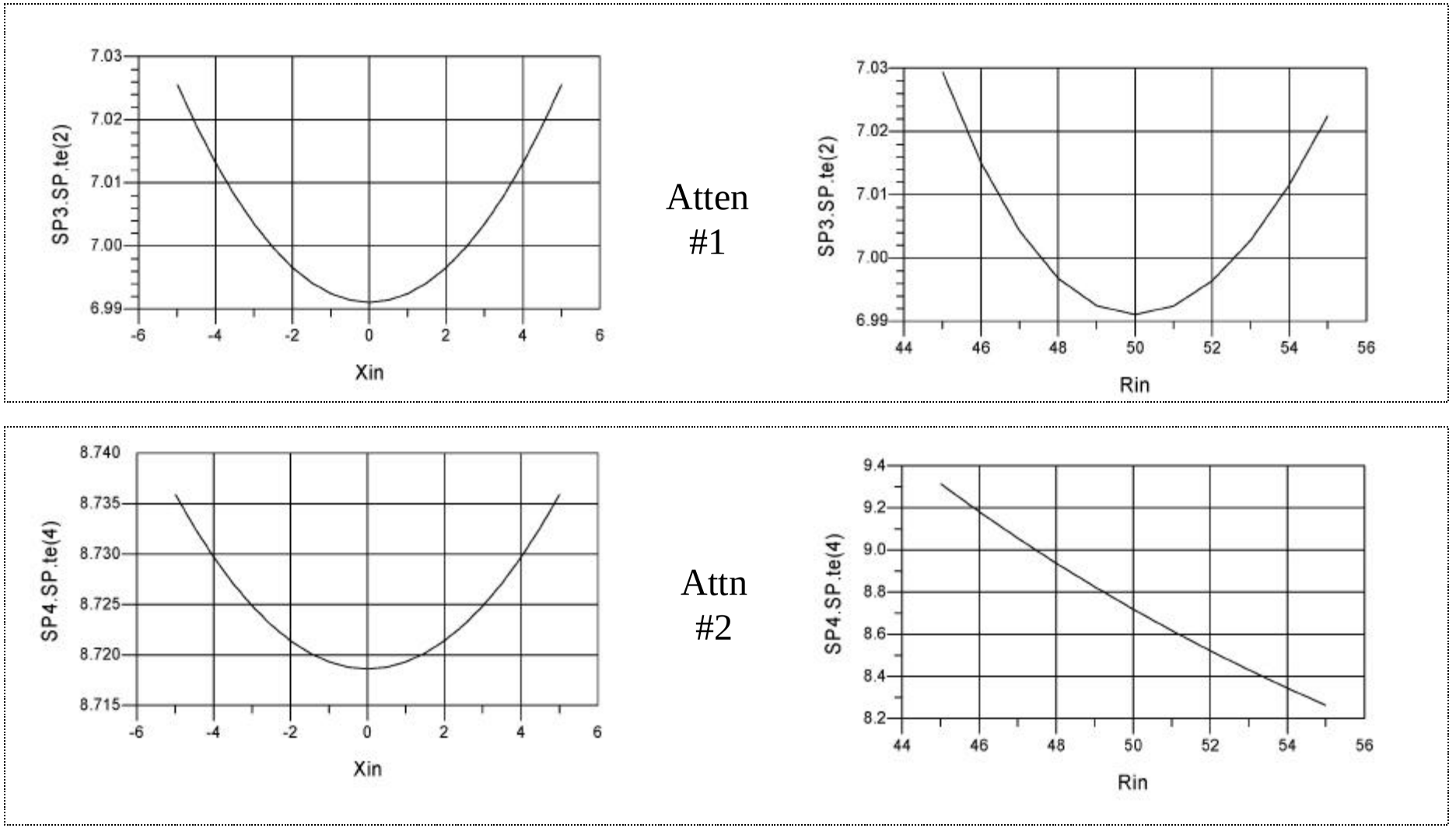

Figure 3 ADS simulation showing noise temperature of the two attenuators for varying input impedance. Upper panel is for Attenuator #1 and the lower panel is for Attenuator #2.

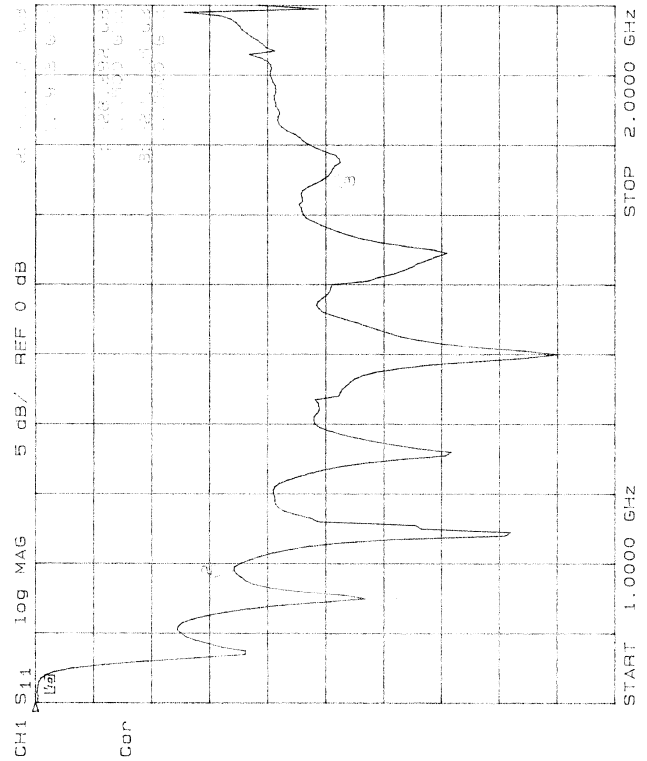

Figure 4 Reflectometry measurements of GBT L-band feed, dewar transition, and OMT made by S. Shrikanth [8].

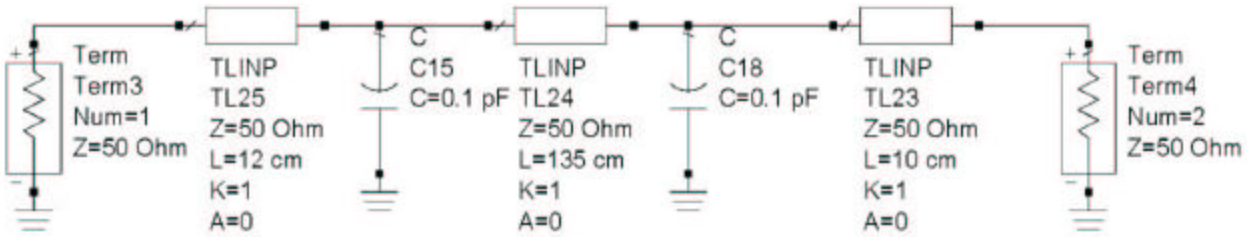

Figure 5 Block diagram of transmission line cascade with capacitance loading between sections.

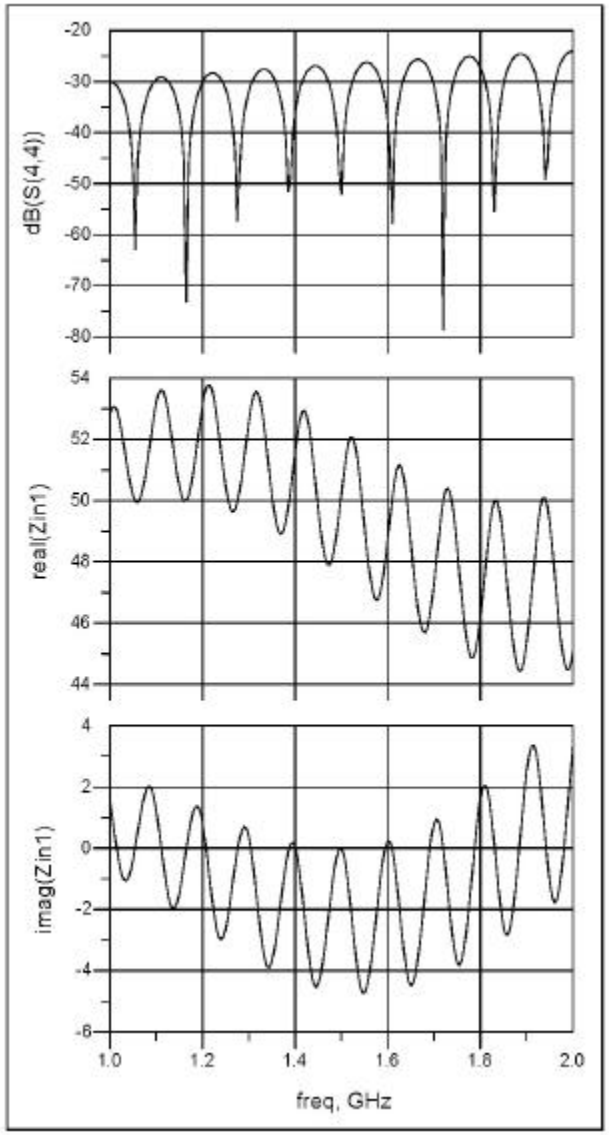

Figure 6 ADS simulation results showing |S22| (shown here as S44) and the complex input impedance for the loaded transmission line cascade shown in Fig. 5.

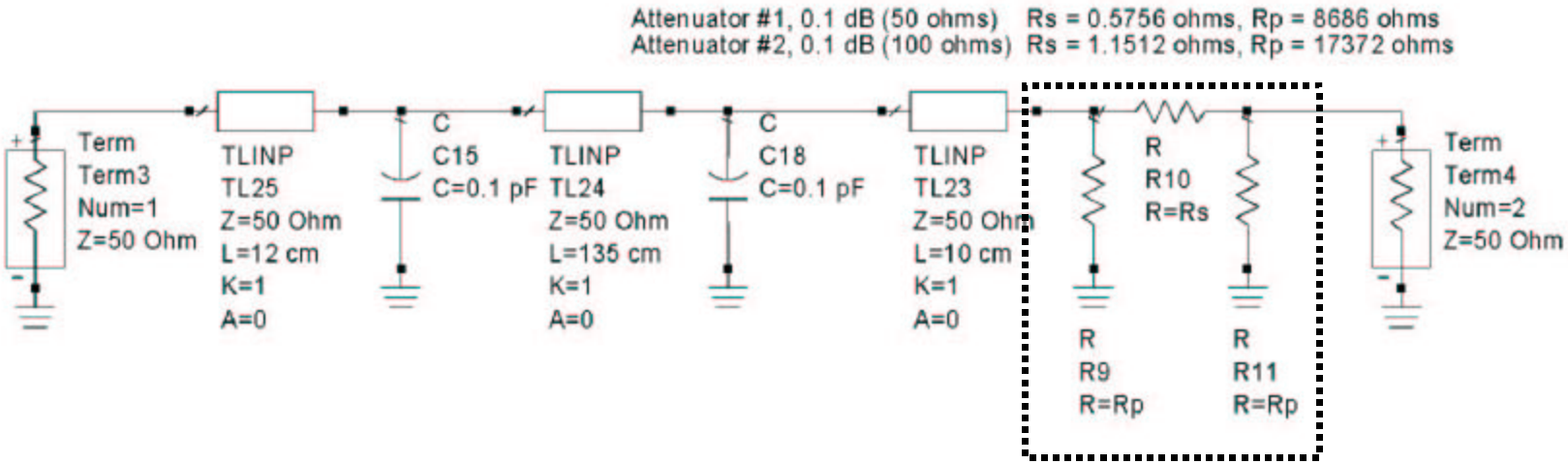

Figure 7 Block diagram of attenuator with the loaded transmission line at its input.

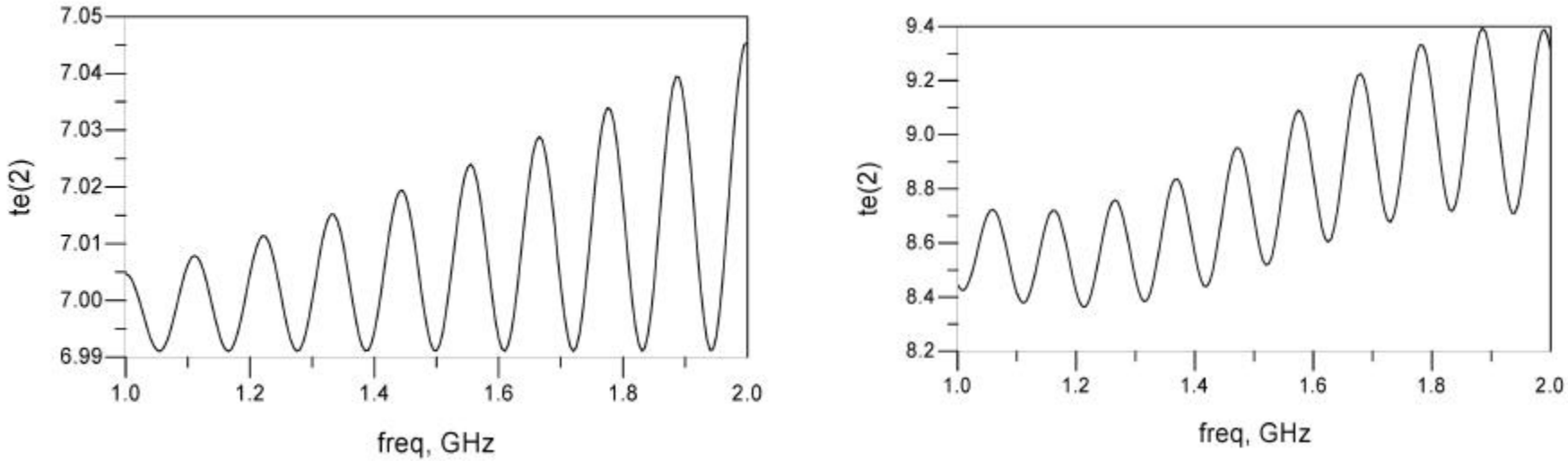

Figure 8 ADS simulation of the circuit shown in Fig. 7. The noise temperature of the circuit versus frequency for Attenuator #1 is displayed on the left and that of Attenuator #2 is shown on the right.

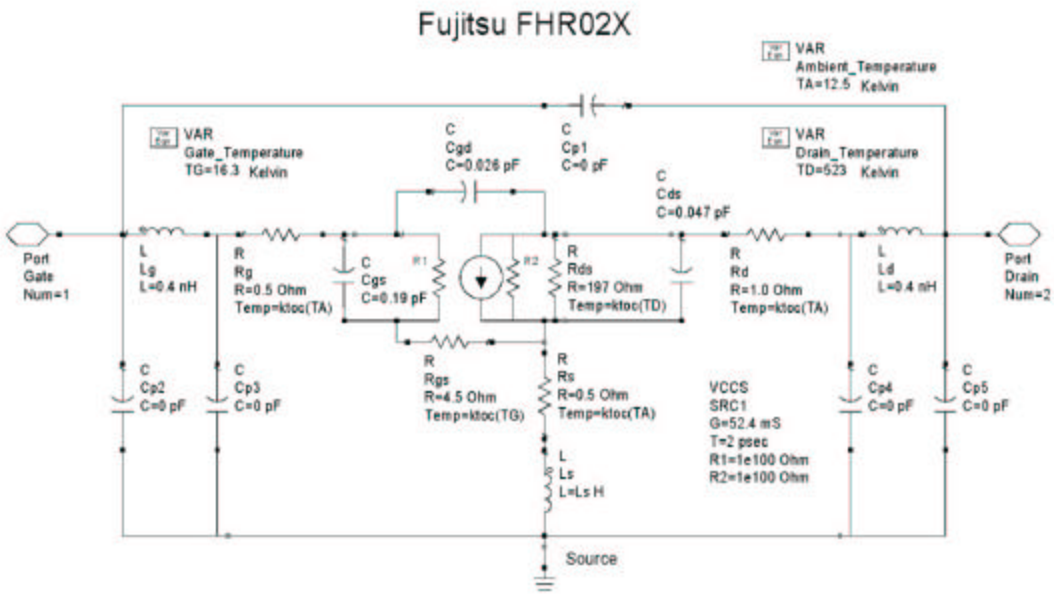

Figure 9 Schematic diagram of the HFET model used in the ADS simulations [9].

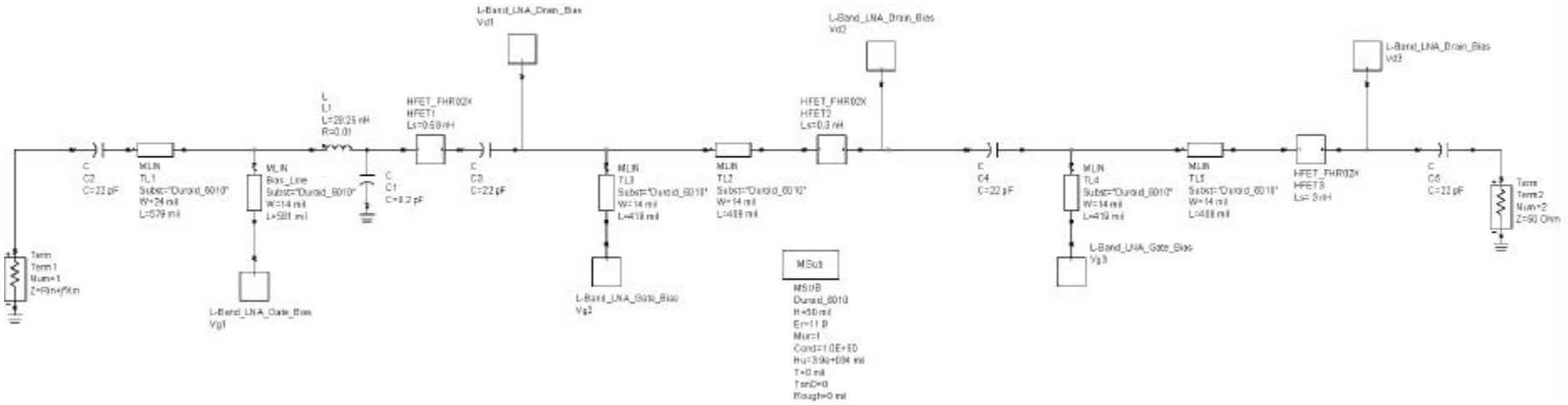

Figure 10 Block diagram of the three-stage, single-ended low noise amplifier used in the ADS simulations.

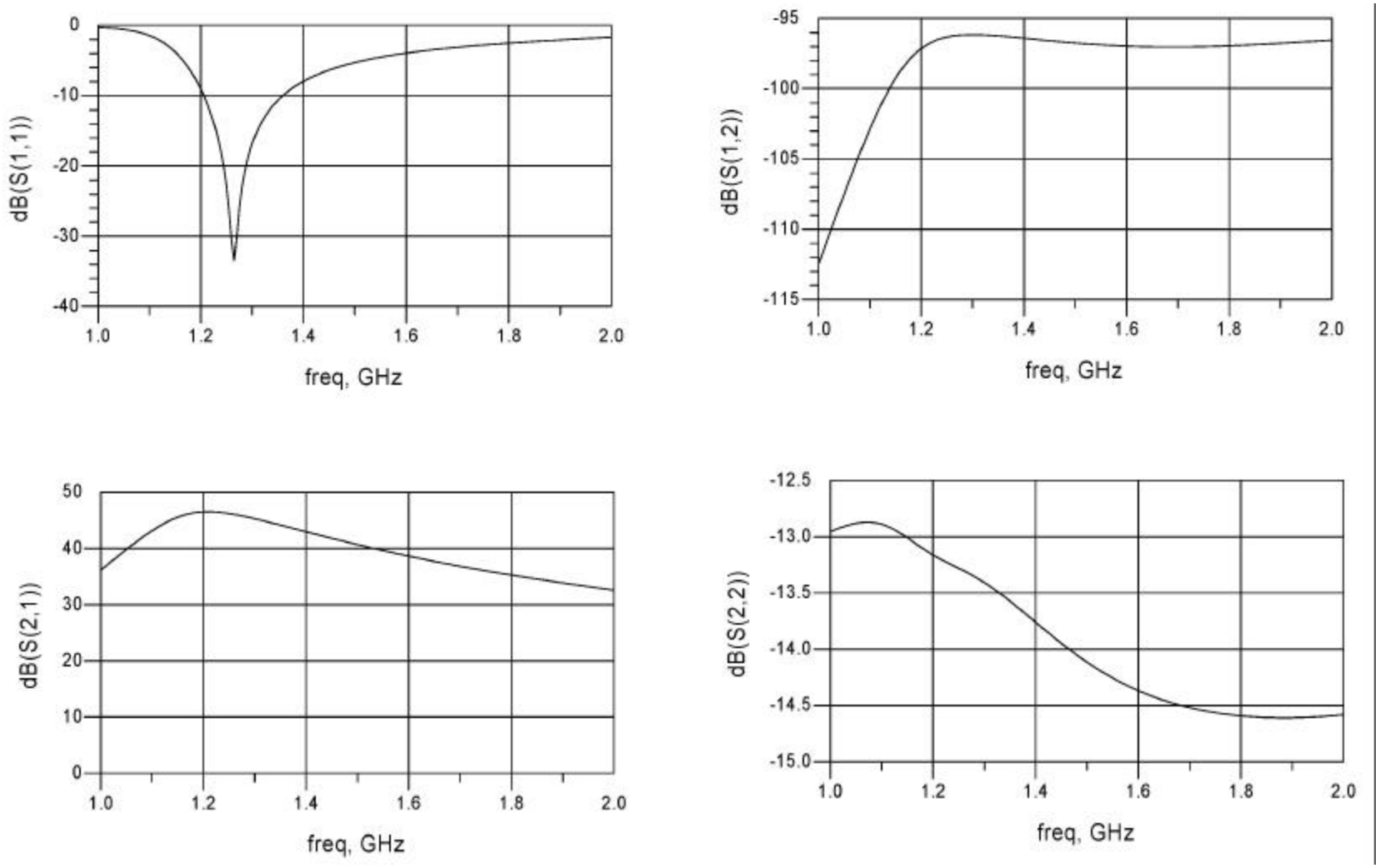

Figure 11 Calculated S-parameters for the three-stage low noise amplifier model.

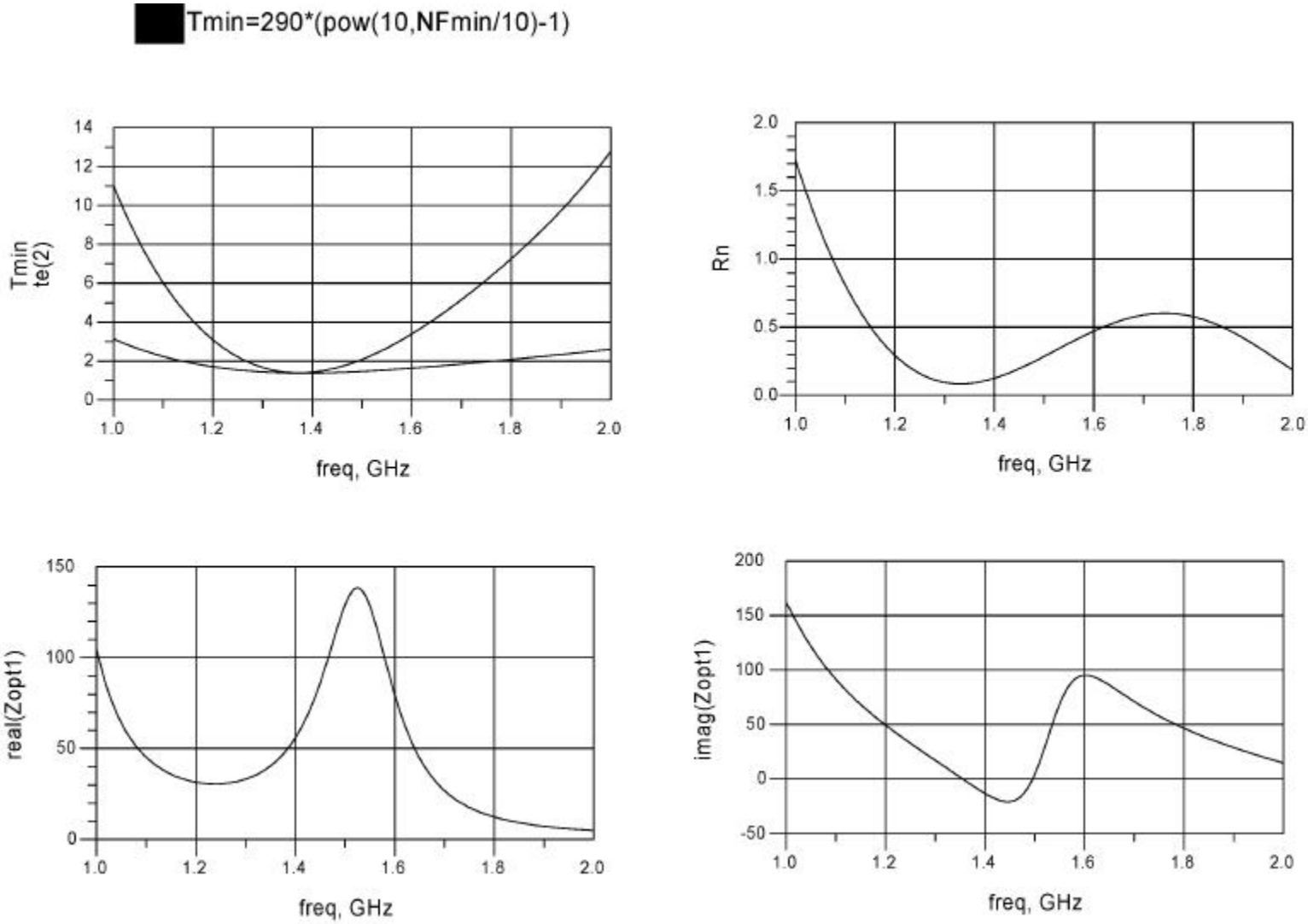

Figure 12 Calculated noise parameters and noise temperature of the three-stage low noise amplifier used in the ADS simulations.

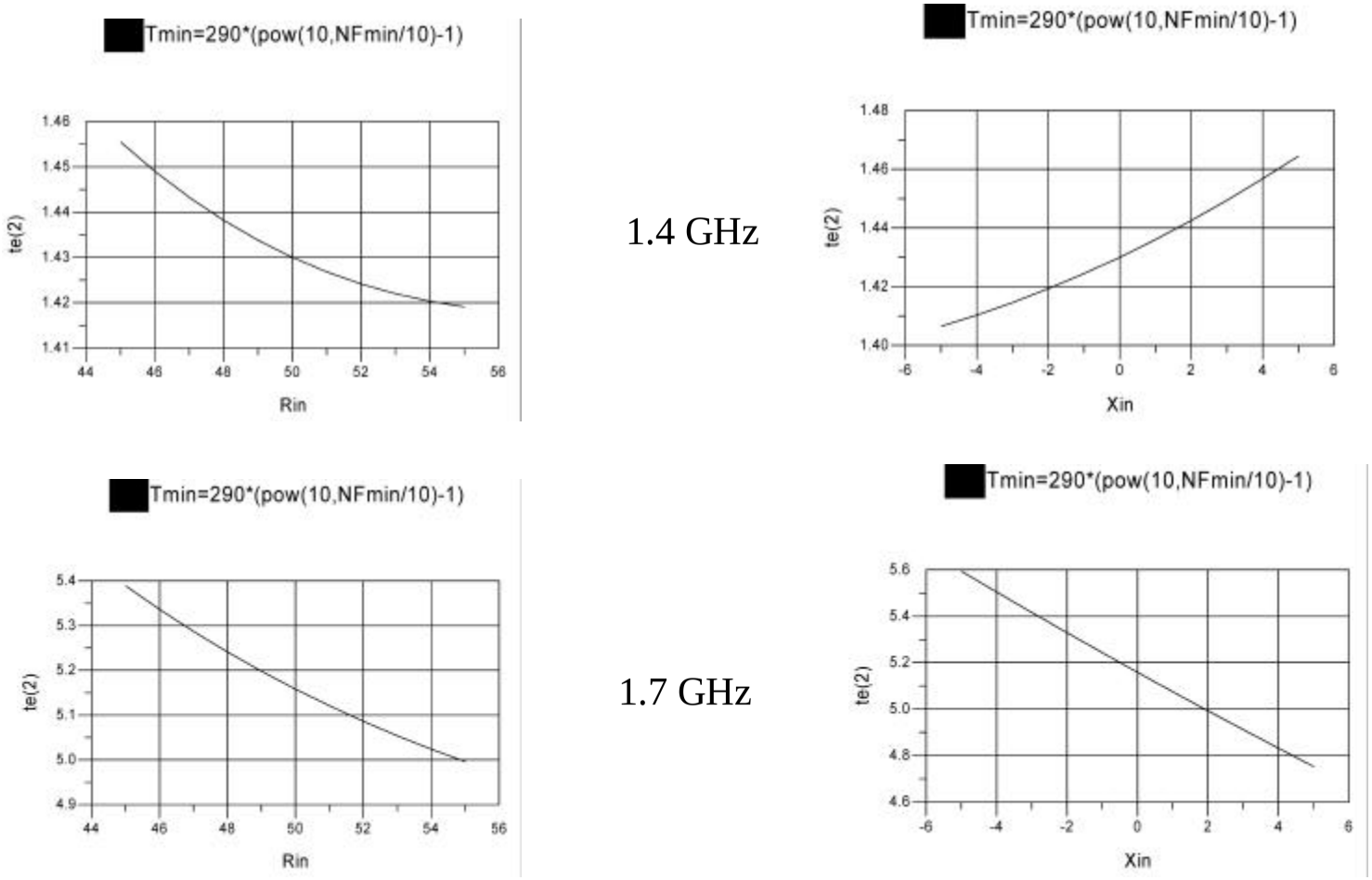

Figure 13 Calculated noise temperature of the three-stage low noise amplifier as a function of input resistance (left) and input reactance (right) at 1.4 and 1.7 GHz.

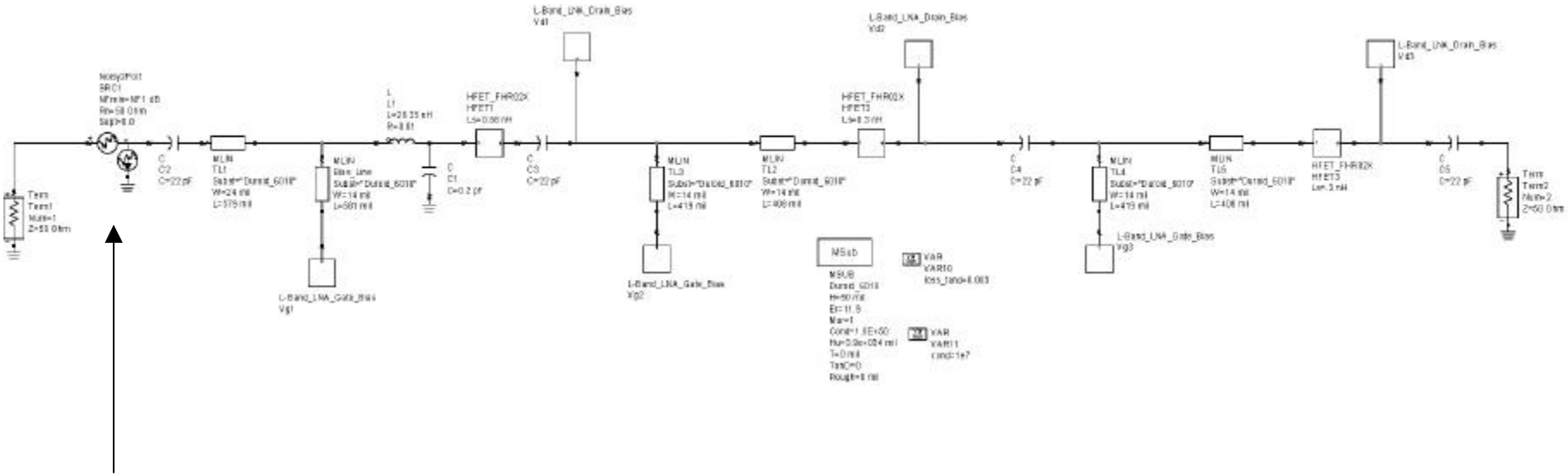

Figure 14 Low noise amplifier model with a noise source at the input to simulate an antenna temperature that is constant with frequency.

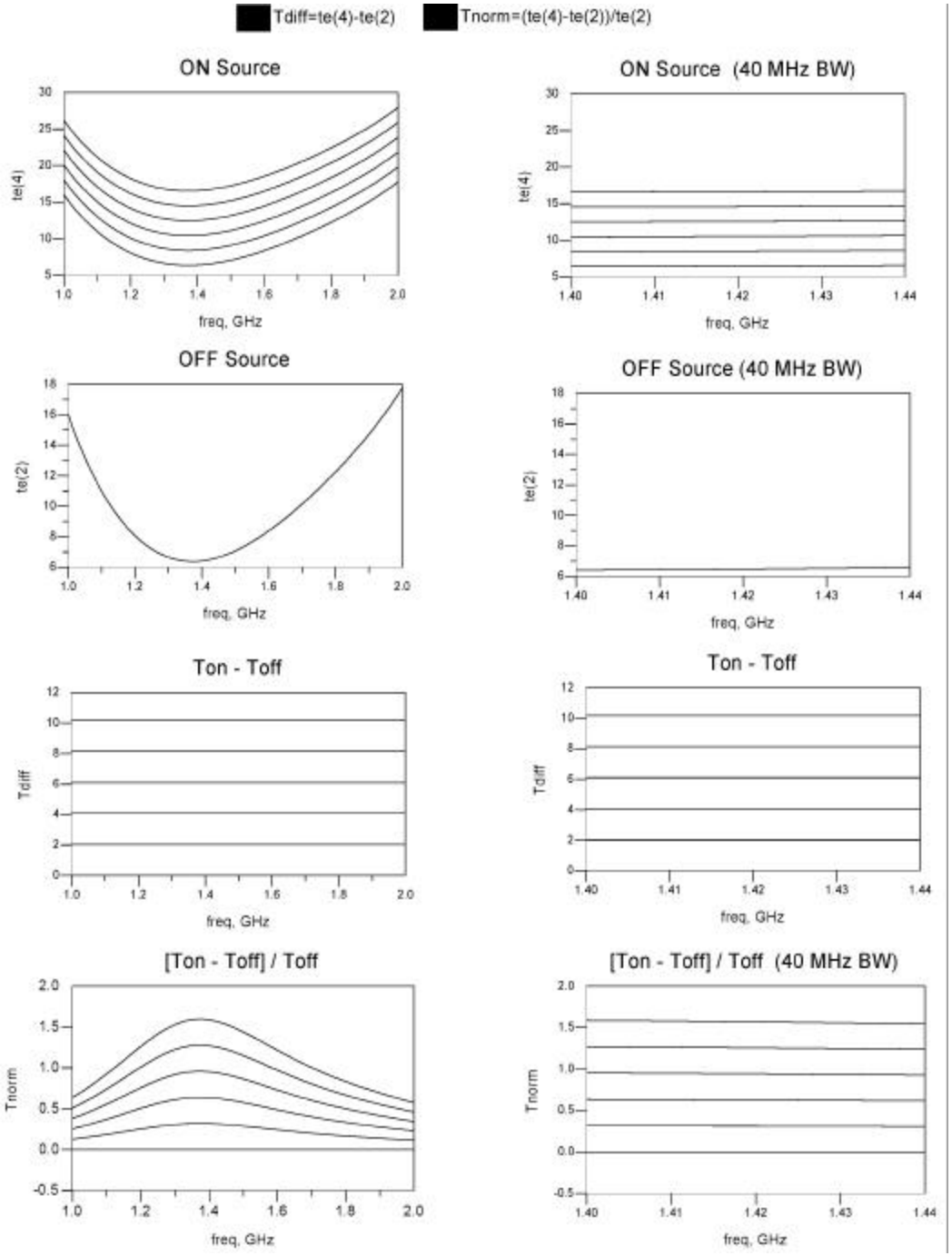

Figure 15 On/Off sequence involving only the low noise amplifier.

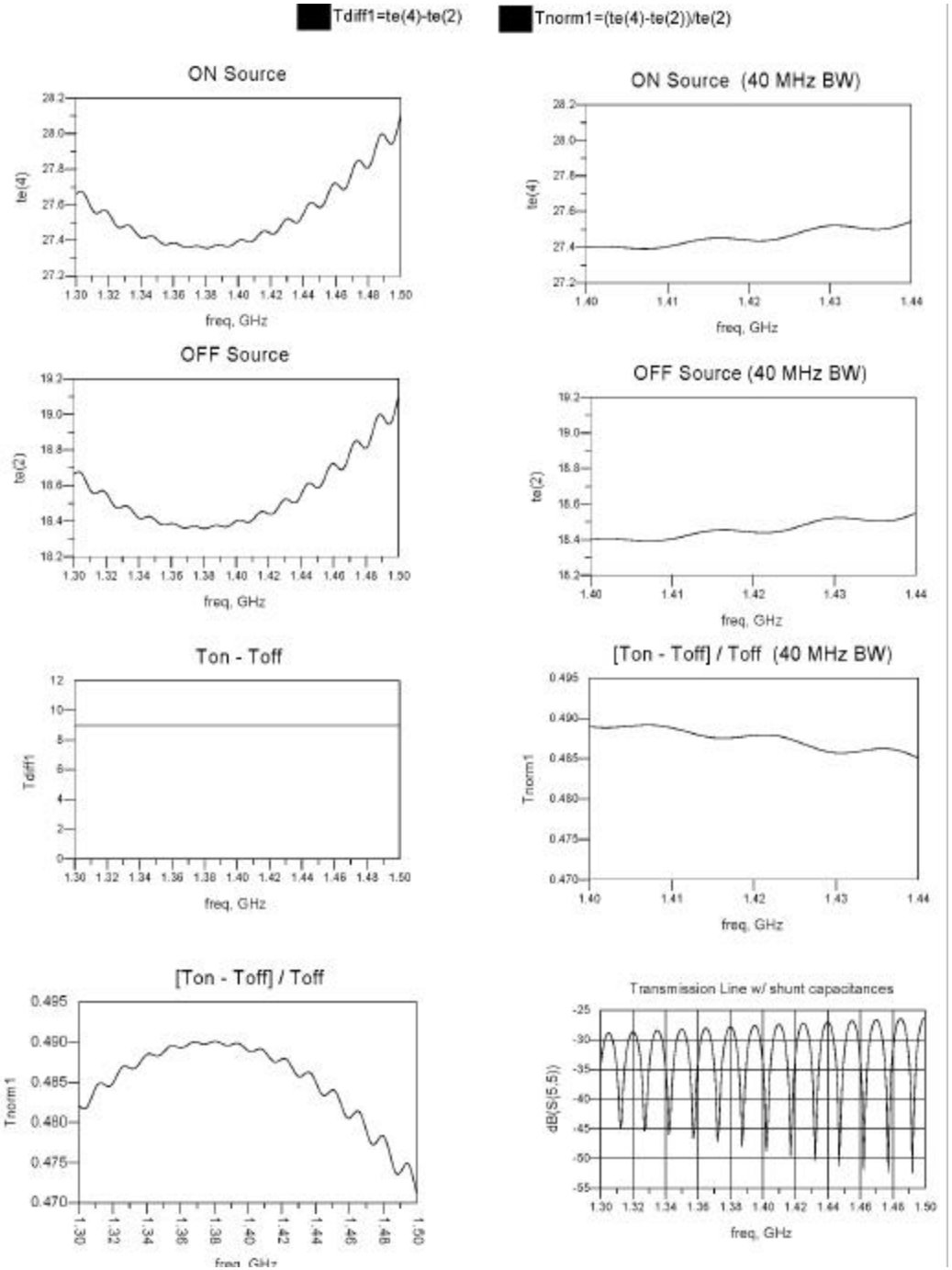

Figure 16 On/off sequence for low noise amplifier and loaded transmission line.

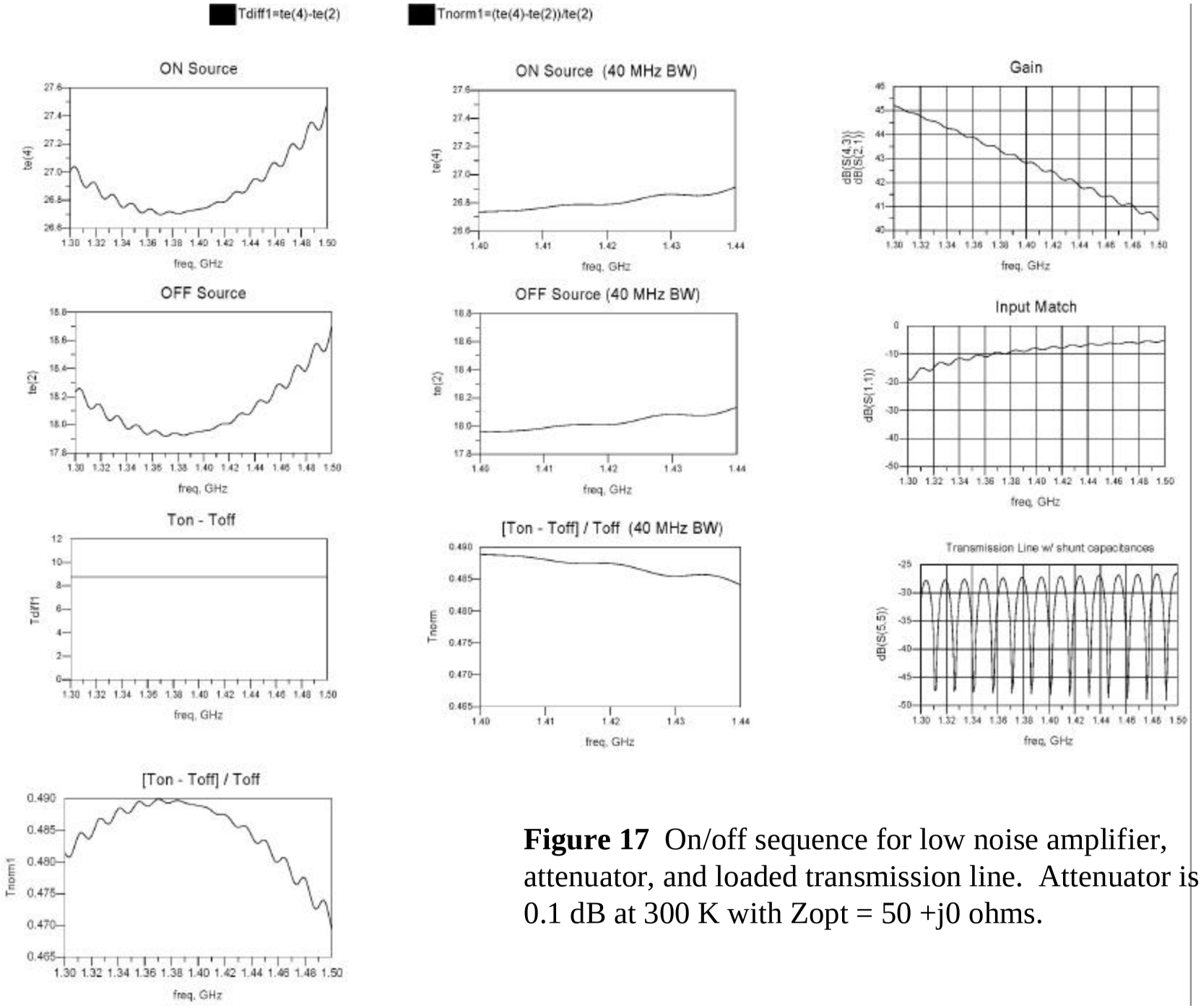

Figure 17 On/off sequence for low noise amplifier, attenuator, and loaded transmission line. Attenuator is 0.1 dB at 300 K with Zopt = 50 +j0 ohms.

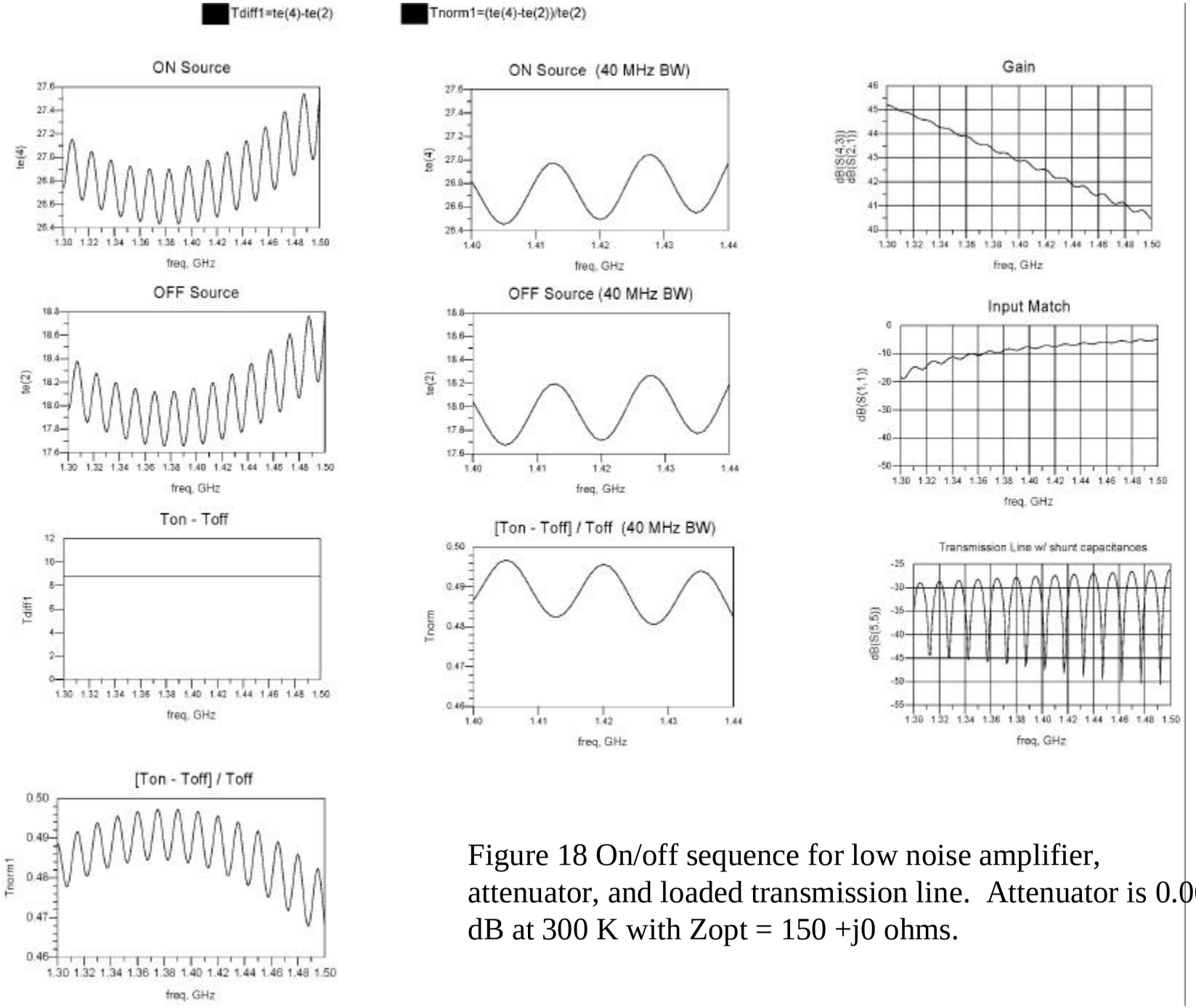

Figure 18 On/off sequence for low noise amplifier, attenuator, and loaded transmission line. Attenuator is 0.06 dB at 300 K with Zopt = 150 +j0 ohms.

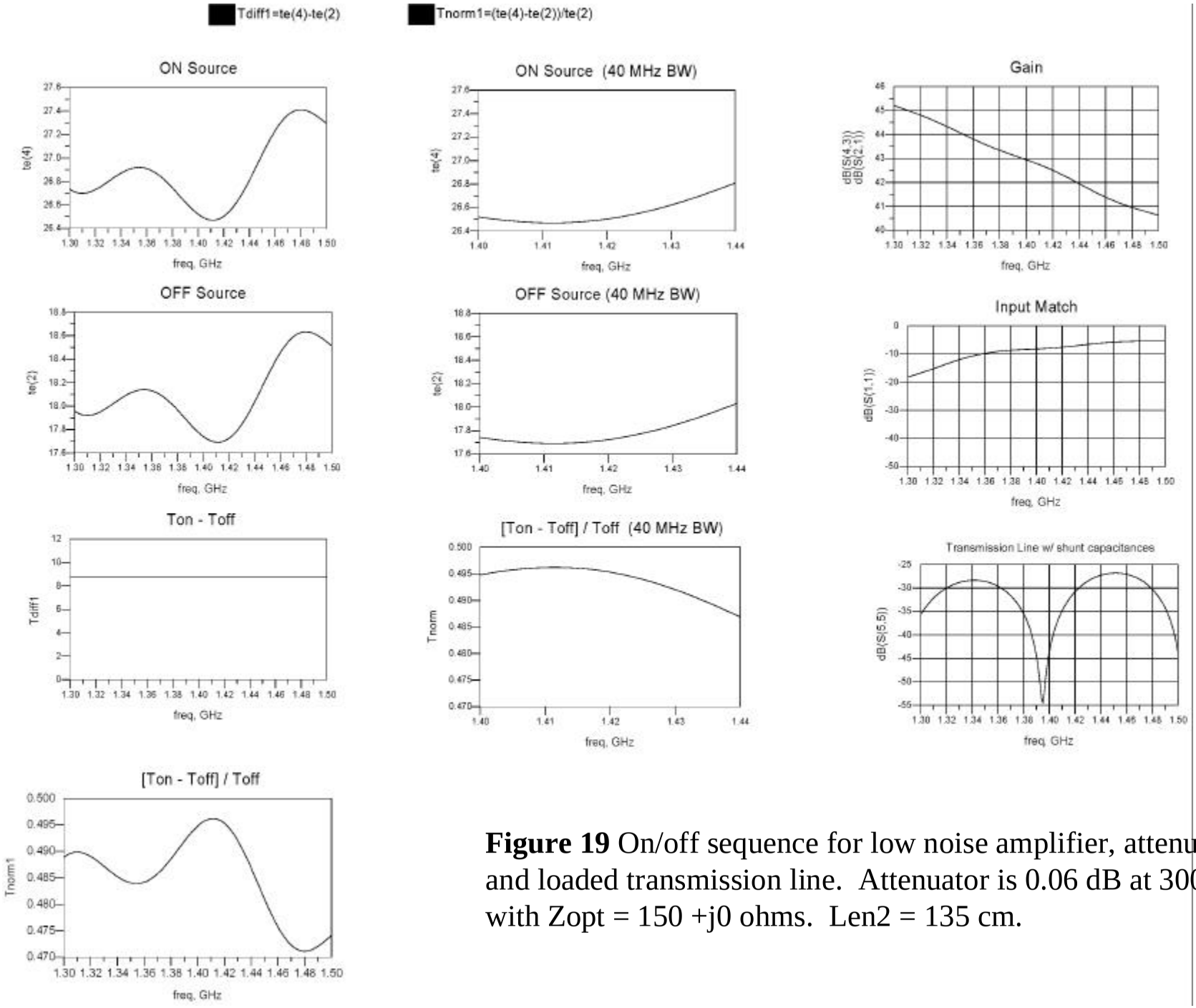

Figure 19 On/off sequence for low noise amplifier, attenuator, and loaded transmission line. Attenuator is 0.06 dB at 300 K with Zopt = 150 +j0 ohms. Len2 = 135 cm.

Addendum
Electronics Division Internal Report
No. 312

October 20, 2004

Abstract

NRAO Electronics Division Internal Report 312, published September 2, 2003, described investigations into the character and causes of the Green Bank Telescope spectral baselines. Since publication, several steps have been taken to further understand and mitigate some of the causes of unsatisfactory baselines. This Addendum to EDIR 312 will review the steps taken and additional knowledge obtained to date, and describe future plans.

1 Review

Spectroscopy in radio astronomy is generally done by measuring the system output spectra under two conditions: one (S_r) with the beam on a reference position, and a second (S_s) on the source of interest. On the GBT, the switching is accomplished by position switching (moving the antenna position), and/or by beam switching (available at frequencies above 12GHz). To understand the analysis of position switched data, it is useful to model the receiver chain with a power gain transfer function $G(f)$ and noise temperature $T_{rx}(f)$. As indicated, both of these quantities are functions of frequency and summarize the cascade of many active and passive components. Our system consists of the antenna, the receiver chain, and a spectrometer used to measure the output power spectrum. The equation for the system output power spectrum may be written as:

$$S_o(f) = (T_{sor}(f) + T_{ant}(f) + T_{rx}(f))k_B G(f) \tag{1}$$

where T_{sor} represents the effective temperature of the antenna main beam, T_{ant} the amalgamation of noise due to atmosphere, background, spillover, etc., T_{rx} is the noise temperature of the receiver and feed, and k_B is the product of Boltzmann's constant and the effective bandwidth of each spectrometer frequency channel. (Note that each noise component is or may be a function of frequency, but from this point on we will omit the (f) except when it seems important to emphasize the frequency variation.) We can now write equations for output spectra S_s and S_r. The receiver gain and noise temperature are in general functions of time, if not signal level, so we will also distinguish the gain and noise values during the respective spectral measurements with s and r subscripts.

$$S_r = (T_{ref} + T_{ant,r} + T_{rx,r})k_B G_r \tag{2}$$

$$S_s = (T_{sig} + T_{ant,s} + T_{rx,s})k_B G_s \tag{3}$$

Because the system gain function has relatively large variations with frequency, we calculate the ratio of the two scans which under certain conditions will cancel the gain function:

$$\frac{S_s}{S_r} - 1 = \frac{S_s - S_r}{S_r} = \frac{(T_{sig} + T_{ant,s} + T_{rx,s})G_s - (T_{ref} + T_{ant,r} + T_{rx,r})G_r}{(T_{ref} + T_{ant,r} + T_{rx,r})G_r} \tag{4}$$

regrouping we obtain,

$$\frac{S_s - S_r}{S_r} = \frac{(T_{sig}G_s - T_{ref}G_r) + (T_{ant,s}G_s - T_{ant,r}G_r) + (T_{rx,s}G_s - T_{rx,r}G_r)}{(T_{ref} + T_{ant,r} + T_{rx,r})G_r} \tag{5}$$

The quantity of interest is $T_{sig}(f) - T_{ref}(f)$, and to pluck this value from equation 5, it is first necessary that the system gain and noise temperature are

completely stable over the measurement period. That is $G_s = G_r$, $T_{ant,s} = T_{ant,r}$, and $T_{rx,s} = T_{rx,r}$. Then equation 5 becomes:

$$\frac{S_s - S_r}{S_r} = \frac{T_{sig} - T_{ref}}{T_{ref} + T_{ant,r} + T_{rx,r}} \tag{6}$$

This equation shows that, even with perfect system stability during the measurement, the quantity $(S_s - S_r)/S_r$ will only be flat with frequency if $T_{ref} + T_{ant,r} + T_{rx,r}$ is flat, or $T_{sig} - T_{ref}$ is very small over most of the frequency range. The denominator of equation 6 is just $T_{sys}(f)$ during the reference scan, so multiplying by that value will retrieve the desired quantity $T_{sig} - T_{ref}$. $T_{sys,r}$ is usually determined by using a small injected noise cal, but for flat baselines $T_{sys,r}$, and hence T_{cal}, must be determined to a high accuracy at every frequency in the passband. The importance of this increases as the average difference between T_{sig} and T_{ref} gets larger (spectroscopy on continuum sources). In the past, spectral data analysis has generally assumed a constant T_{cal} and/or T_{sys} across the spectrum, or at most a fit to a few points, but with the broad bandwidths available from the GBT spectrometer, in many cases that turns out to be an unsatisfactory approach.

It is clear from this discussion that gain or noise temperature changes during a measurement will prevent the cancellation of quantities in equation 5. And, ripple in $Tsys$ must be minimized or measured accurately in order to cancel the denominator of equation 6.

The past year's work on GBT baselines has focused on three broad areas:

Gain Stability The degree of stability required is challenging. Most of the identified problems were related to coaxial interconnections, and were addressed by improved testing and assembly procedures.

Standing Waves As discussed in the body of EDIR 312, standing waves impact the system by producing frequency structure in both gain and noise temperature. The standing wave stability is affected by changes in mismatch magnitude or phase, and by changes in the electrical length of transmission paths. The effects can be attacked by reducing the magnitude of mismatches, stabilizing the electrical length of transmission lines, or shortening transmission lines (which increases the period of the ripple and may make it easier to tolerate).

Receiver Noise Ripple Extensive testing has shown that frequency structure in receiver noise temperature is a major source of difficulties in observing strong continuum sources. Little progress beyond what was described in the body of EDIR 312 has been made in reducing the structure, but some progress has been made in the understanding and in calibration methods.

Discussion of specific areas of work follow.

2 Coaxial Cables

PTFE (Teflon), the most common dielectric found in microwave cables, has an unfortunate transition in its physical properties near room temperature. That leads to high sensitivity of electrical length to temperature (about 100ppm/$^\circ C$). As described in EDIR 312, section 4.4, a couple of varieties of Andrews Heliax type cables using polyethylene dielectric have significantly better temperature coefficients, and have been installed in several critical locations. Occasional problems with the FSJ1-50A Heliax developed due to shearing of the copper jacket at the SMA connector clamp-on backshell. These failures caused gain instabilities that were intermittant and position dependent. An assembly procedure was developed that supplemented the clamp with epoxy potting, and has largely eliminated cable failures due to this cause. Connector problems with other Heliax cable types have occurred, and one must be careful in their use, despite the attractive performance of the cable itself.

Longer PTFE cables in the Equipment Room between the Converter Racks and the Spectrometer were placed in conduits to buffer air temperature fluctuations. These cables carry lower frequencies and the cost of retrofitting to Heliax does not yet seem necessary. Ripple components consistent with the cable lengths have not been observed in baselines since the buffering was installed.

3 Feed Radomes

The Gregorian feeds have woven PTFE sheets over the feed apertures, and water on this surface leads to reflections that are unstable as the water moves around. The radome blower system was upgraded to increase the air flow, significantly improving the removal of water beads.

The original radome designs used flat metal rings to clamp the PTFE sheets to the feed horns. That led to a recess in which water tended to puddle. All the feeds at X-band and above have now been retrofitted to use a wrap-around design for radome attachment, eliminating the recess.

4 Converter Rack

EDIR 312 section 4.5 described a persistant baseline ripple component with period near 60MHz, whose origin had been isolated to the Converter Racks and was closely related to the Equipment Room temperature. The magnitude of this ripple ranged up to about 0.5% of the total power. The generating mechanism was not well understood however, and effort was spent both to improve the temperature stability, and to understand how the ripple was generated.

Figure 1 shows a simplified view of the interface between the IF Optical Receiver and the 1-8 GHz Converter modules. The IF signal is amplified and split four ways in the Optical Receiver,and then goes to four Converter modules (only two of the four Converter modules are shown in the figure). The baseline ripple generating mechanism is understood by tracing a signal through the

diagram: A signal leaves the amplifier and is split four ways in the power divider, which has electrical delay Θ_d. The one-fourth signal that exits the lower port travels through a fairly long coaxial cable with delay Θ_2 and enters the Converter module input switch and mixer. However, a portion of the signal is reflected by reflection coefficient ρ_2, back thru the cable delay Θ_2 and the power divider and into the amplifier output port. At the amplifier output, a portion is reflected, ρ_a, and reenters the splitter input. So, the total signal that enters the top converter module mixer is the vector sum of one-fourth of the amplifier output signal, and a smaller component which has travelled through Θ_d and Θ_2 twice. (And two other components off the other two converter modules not shown.) These reflected signals cause standing waves and hence gain ripples with frequency. Note that if the phase of the reflected signals change due to, say, change in the electrical phase of the cable delay Θ_2, or reflection coefficients ρ_2 or ρ_a, the gain ripple will change resulting in baseline ripples. Early on, the mechanism of change in the cable delay was recognized and phase stable cables were installed. However, the ripples were still apparent and the search began for other causitive mechanisms. In the end, the problems were found to be dominated by a few highly sensitive, defective components - RF switches, pads, etc. Because a defective component affects the response of four channels and the effects tend to be too small to detect with common test equipment, isolating the problems proved to be difficult.

Figure 2 shows a series of two-minute off/on baselines taken through the system illustrating the improvements that have been achieved. Although significant improvements have been made, some ripple is still apparent. This ripple does tend to average out over many off/on pairs. The final solution however probably lies in repackaging of this area of the system to greatly shorten the pathlengths involved and to provide improved thermal buffering.

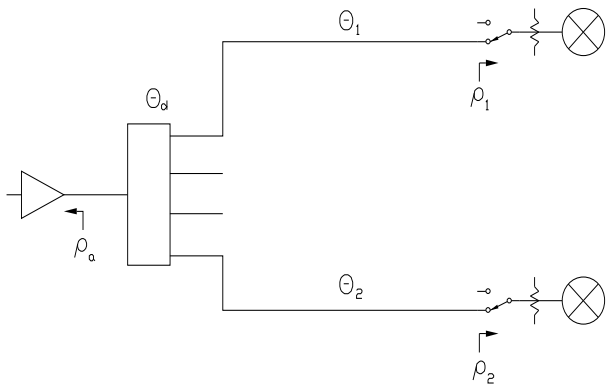

Figure 1: A simplified block diagram of the Optical Receiver - Converter Module interface.

5 Receiver Noise

5.1 Introduction

Section 3 of EDIR 312 discussed spectral baselines on continuum sources. It was recognized that receiver noise which varies with frequency is a potential source of baseline problems because usual data analysis techniques assumed a constant $T_{sys}(f)$. The search for causes of ripple in receiver noise focused on the receiver input area - between the feed aperture and the first LNA - and in fact a few specific problems were identified and corrected as discussed in the original report. However, it became clear that this was not the whole story - the shape of the baselines were too irregular and the period of ripples did not match physical lengths that could set up standing waves. One difficultity in understanding the problem was because our normal laboratory equipment and methods of measuring noise temperature provided frequency resolution too coarse to be of much use. However, the GBT spectrometer obviously provides a means to obtain high-resolution spectra, and as long as the total power does not change by more than 3dB or so, we felt it could be used to perform a hot-cold noise temperature measurement. We put together an experiment using components taken from the GBT 40-52 GHz Q-band receiver, with care taken to eliminate the possibility of input mismatch or resonances affecting the results.

A test arrangement consisting of a cooled LNA and mixer, IF filter, and IF amplifier were taken from the Q-band receiver and placed in one of our test dewars. The LNA input port was connected to a cooled rectangular waveguide load. The load was thermally separated from the LNA with a 1 cm stainless steel waveguide shim. A small heater and temperature sensor allowed the load

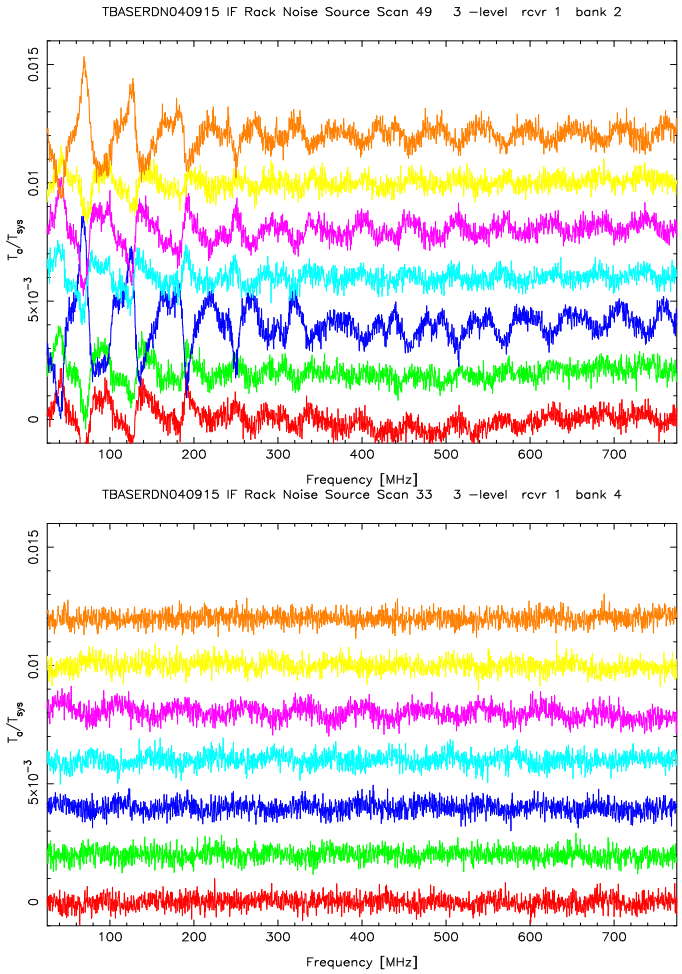

Figure 2: IF system baseline ripples due to Equipment Room temperature before (top panel) and after (bottom panel) improvements to the Converter Rack equipment.

temperature to be adjusted by 10-15K. Measurements on the stainless shim and the load show that the combination has a return loss of 32 dB or better.

The test dewar was located in the Equipment Room and the IF output (centered at 6 GHz) was connected into the GBT IF system via heliax cable. The system and the spectrometer were then configured for 800 MHz bandwidth measurements of the spectrum.

5.2 The Y-factor Method

The most common engineering method of determining a receiver's noise temperature is to measure its output power with two known input source temperatures. The ratio of the two powers is termed the Y-factor. Since a spectrometer measures the spectral power versus frequency, we can use two measurements taken with two source temperatures to obtain $Y(f)$:

$$Y(f) = \frac{S_{hot}}{S_{cold}} = \frac{(T_{hot} + T_{rx,hot}(f))k_B G_s}{(T_{cold} + T_{rx,cold}(f))k_B G_r} \tag{7}$$

Again assuming receiver stability, and solving for T_{rx}, we obtain a familiar equation:

$$T_{rx}(f) = \frac{T_{hot} - Y(f)T_{cold}}{Y(f) - 1} \tag{8}$$

5.3 Q-band Laboratory Data

Spectra were measured with two load temperatures differing by about 15K, and the data used to calculate $T_{rx}(f)$ using equations 7 and 8. Figure 3 plots typical T_{rx} using this method. To check linearity and stability of the data, several subsequent scans taken at a variety of load temperatures were processed through the baseline equations using this measured T_{rx}. Figure 4 shows the effect on spectral baselines when the measured T_{rx} is used in equation 6.

The fact the input load return loss was quite low makes a strong case that the source match seen by the LNA can not explain the noise structure seen in these measurements. Subsequent work indicates that in this receiver mixer noise is a significant contributor to the total receiver noise structure, and can perhaps be mitigated by increasing the gain before the mixer and by terminating the image and other sideband frequencies with low VSWR. Work along these lines is on-going, and may lead to similar investigations in other receivers.

5.4 X-band Astronomical Data

Because of the laboratory results, it seemed possible that the T_{rx} variations have been a major source of baseline structure when observing continuum sources. And, it might be possible to use astronomical observations to measure T_{rx} for subsequent use in baseline data analysis.

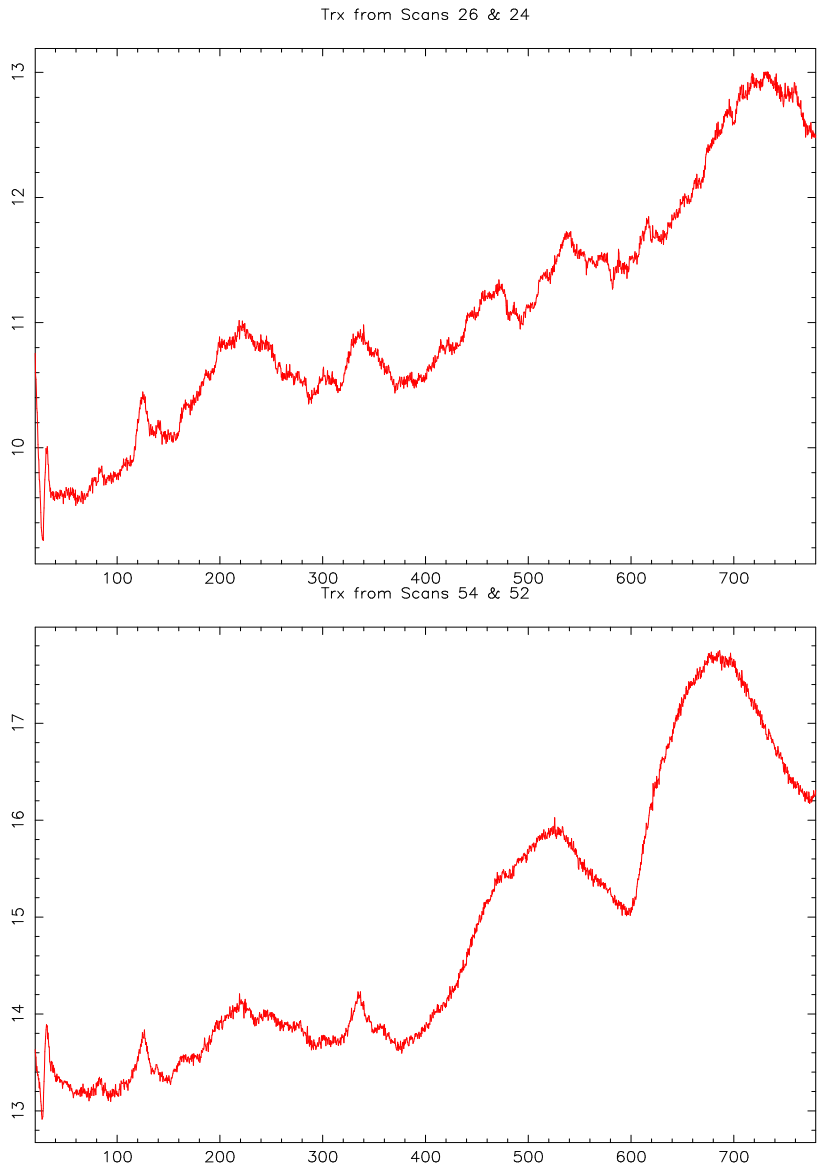

Figure 3: T_{rx} at 42 GHz (upper panel)and 43 GHz (lower panel), obtained from a test dewar containing a Q-band LNA and cooled mixer, calculated with equations 7 and 8. A heated waveguide termination was used to vary the LNA input load temperature.

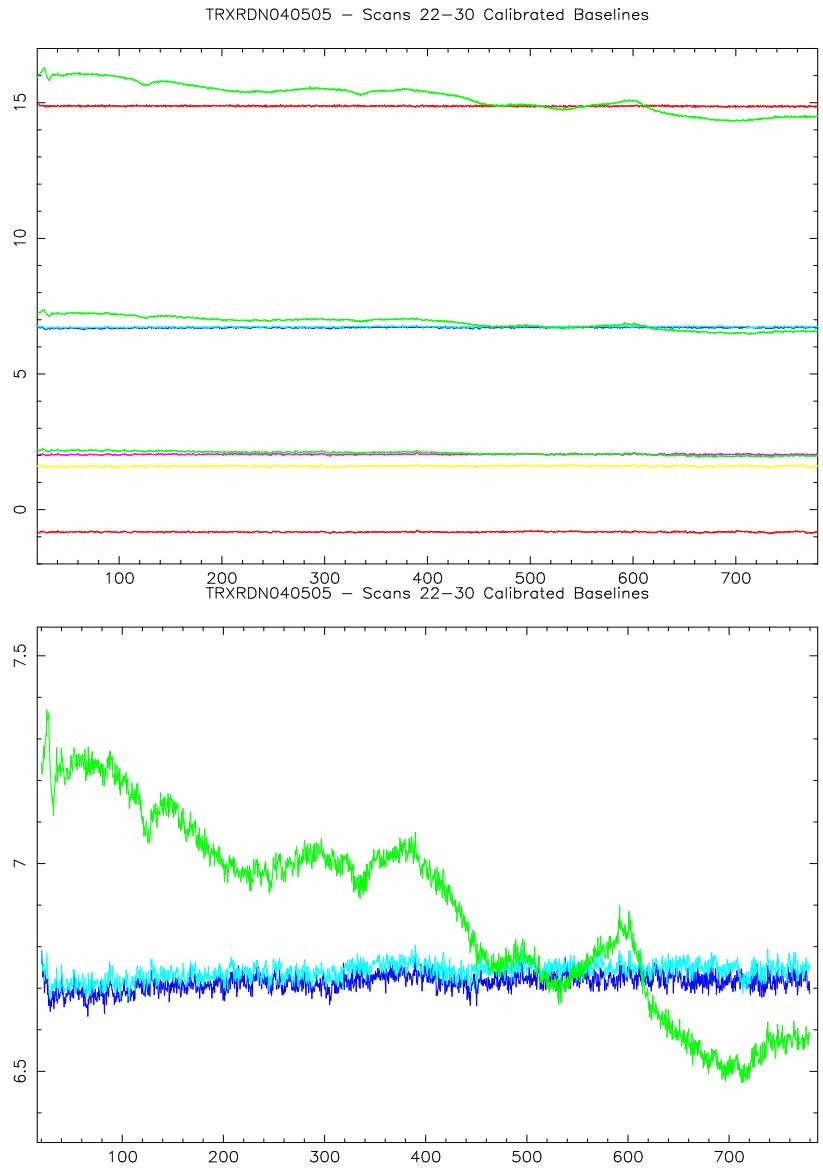

Figure 4: The upper plot shows the spectral baselines on the Q-band test dewar setup for several signal scans taken at various load temperatures. The green traces were calculated using a mean T_{rx} of 15.5K, and the other (flatter) traces used measured $T_{rx}(f)$. The lower panel zooms into the region around 7 K.

To see how the Y-factor measurement of $T_{rx}(f)$ behaves with a front-end operating on the GBT, astronomical data previously taken with the X-band receiver was analyzed. The first data set consisted of a sequence of on-off observations of NGC 7027. One observation was used to calculate T_{rx}, and that value used to analyze subsequent observations. Only one source was observed, but the data can provide an indication of the stability of the analysis. Examples from this dataset are shown in Figures 5 and 6.

The second X-band data set analyzed was a sequence of on-off observations of three sources. By coincidence, one of the sources was NGC 7027, and that source was used to determine T_{rx} applied to analysis of the other sources. The results are shown in Figures 7 and 8.

It is clear from these figures that the technique used here has promise in removing major portions of the baseline structure on continuum sources. However, other uncertainties are introduced by the need to understand well the spectral signature of calibrator sources. Work continues to develop the best and most practical observing and analysis procedures.

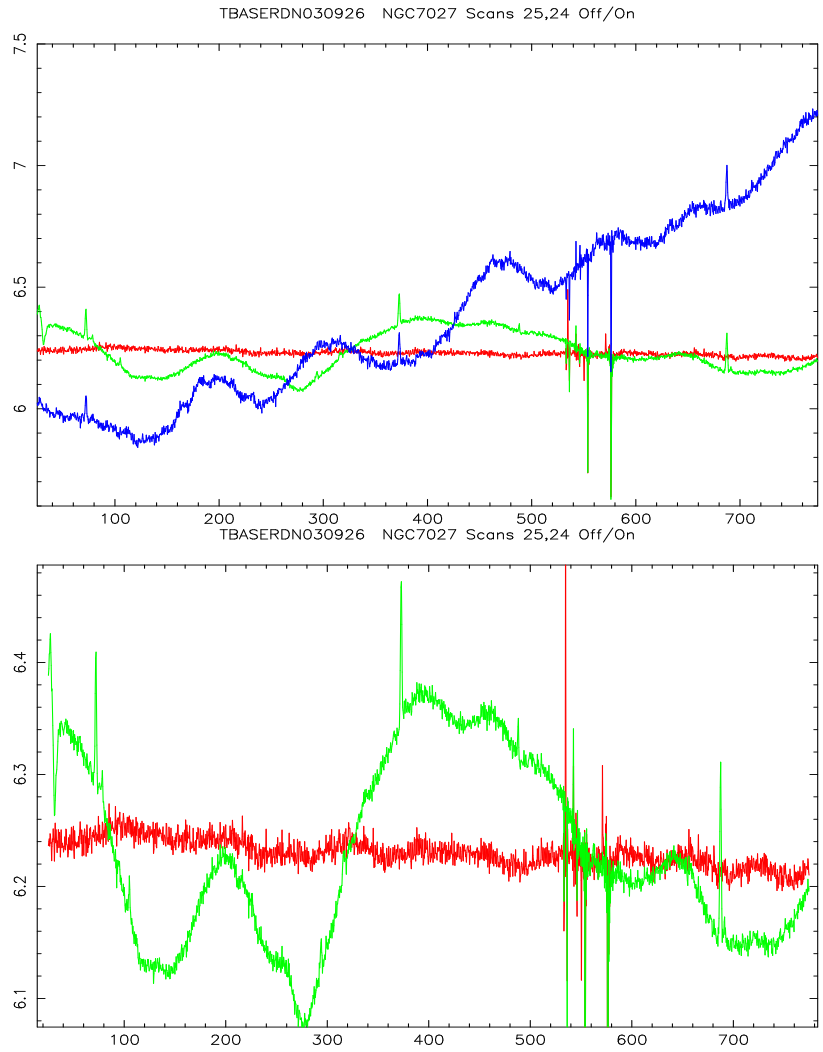

Figure 5: X-band spectral baselines calculated for TBASERDN030926 scan pair 24 and 25, ACS Bank A. The red trace was calculated using T_{rx} measured using scan pair 22 and 23 data as a Hot/Cold measurement. The green trace was calculated using a constant T_{sys}, and the blue trace used a T_{sys} derived from Cal On - Cal Off data in scan 25. The vertical scale corresponds to $T_{On} - T_{Off}$ in Kelvin. The lower panel shows the red and green traces in more detail. For these plots 400MHz on the horizontal axis corresponds to a sky frequency of 9000MHz, and sky frequency increases to the right. The data was from the RCP polarization.

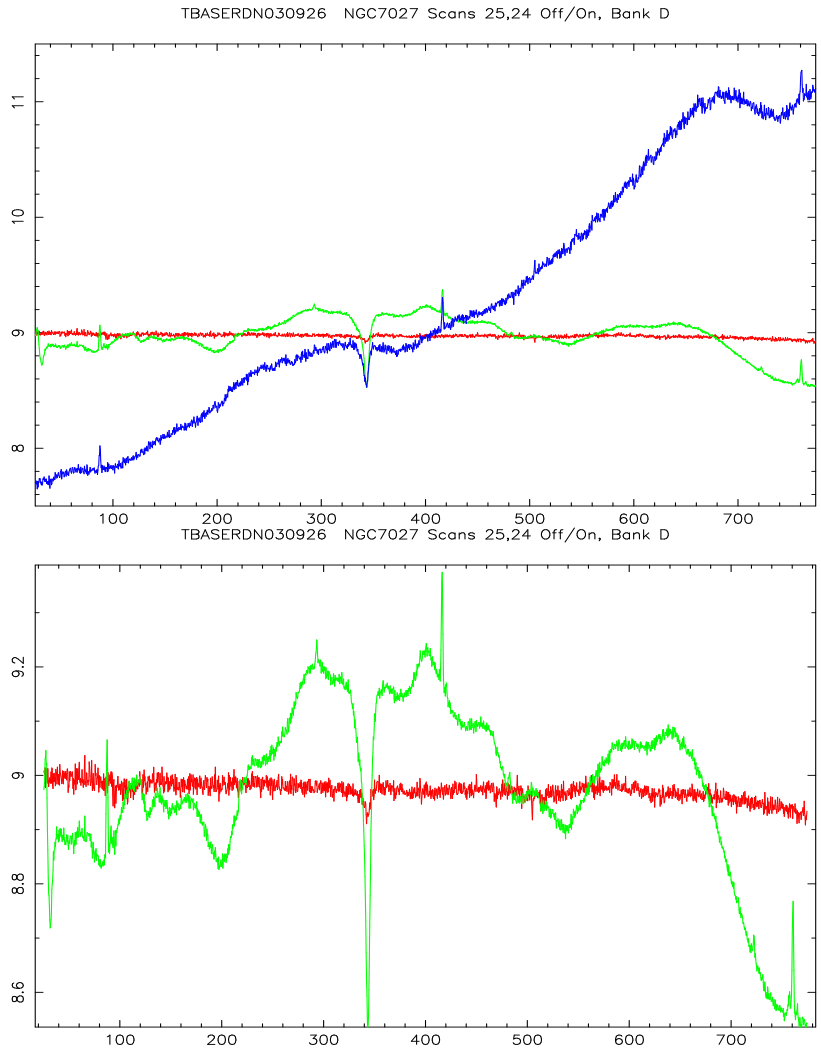

Figure 6: X-band spectral baselines calculated for TBASERDN030926 scan pair 24 and 25, ACS Bank D, calculated in three ways. The red trace was calculated using T_{rx} measured using scan pair 22 and 23 data as a Hot/Cold measurement. The green trace was calculated using a constant T_{sys}, and the blue trace used a T_{sys} derived from Cal On - Cal Off data in scan 25. The vertical scale corresponds to $T_{On} - T_{Off}$ in Kelvin. The lower panel shows the red and green traces in more detail. For these plots 400MHz on the horizontal axis corresponds to a sky frequency of 9600MHz, and sky frequency increases to the right. The data was from the RCP polarization.

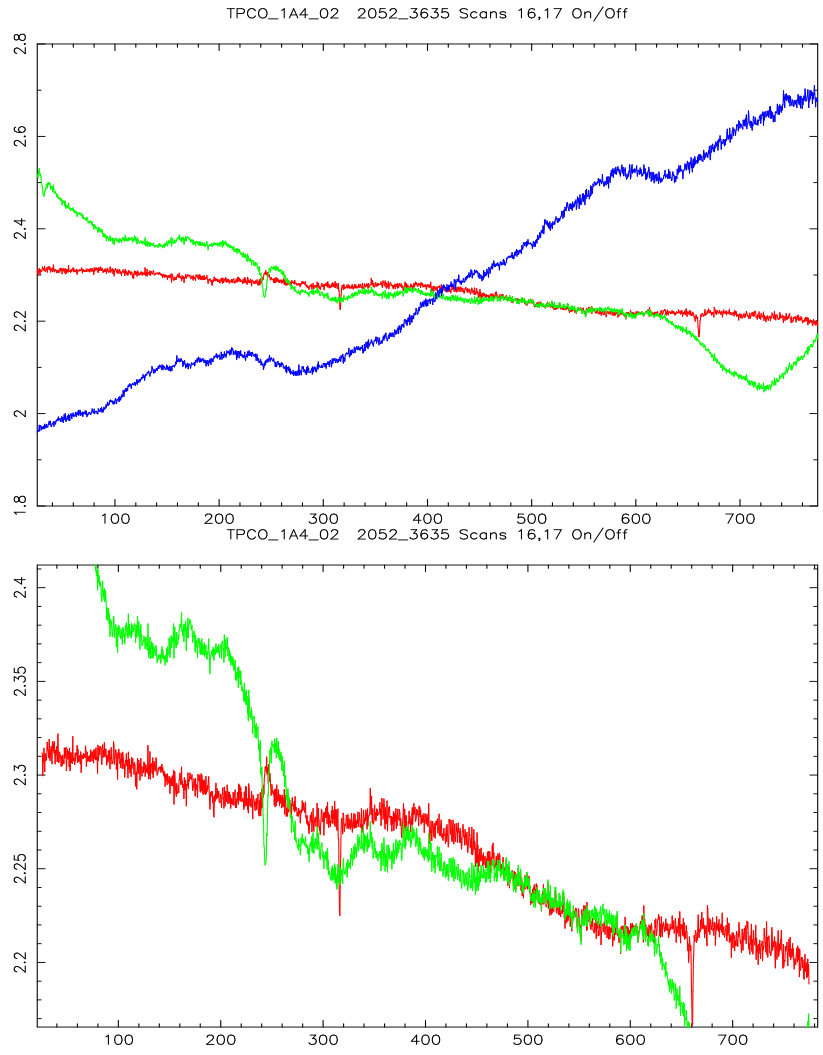

Figure 7: X-band spectral baselines for TPCO1A402 scan pair 16 and 17, on 2052−3635, calculated in three ways. The red trace was calculated using T_{rx} measured using scan pair 14 and 15, NGC 7027 data, as a Hot/Cold measurement. The green trace was calculated using a constant T_{sys}, and the blue trace used a T_{sys} derived from Cal On - Cal Off data in scan 17. The vertical scale corresponds to $T_{On} - T_{Off}$ in Kelvin. The lower panel shows the red and green traces in more detail. For these plots 400MHz on the horizontal axis corresponds to a sky frequency of 9900MHz, and sky frequency increases to the right. The data was from the RCP polarization.

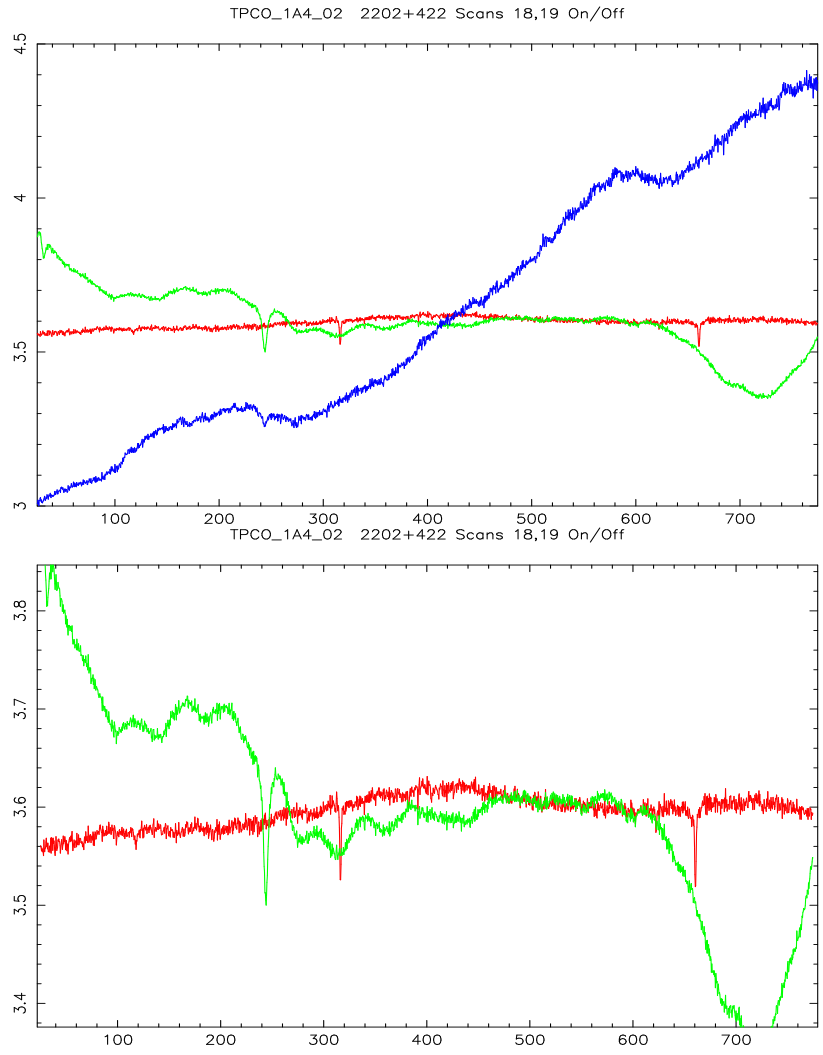

Figure 8: X-band spectral baselines for TPCO1A402 scan pair 18 and 19, on 2202+422, calculated in three ways. The red trace was calculated using T_{rx} measured using scan pair 14 and 15, NGC 7027 data, as a Hot/Cold measurement. The green trace was calculated using a constant T_{sys}, and the blue trace used a T_{sys} derived from Cal On - Cal Off data in scan 19. The vertical scale corresponds to $T_{On} - T_{Off}$ in Kelvin. The lower panel shows the red and green traces in more detail. For these plots 400MHz on the horizontal axis corresponds to a sky frequency of 9900MHz, and sky frequency increases to the right. The data was from the RCP polarization.

6 Conclusions

The understanding of GBT spectral baseline characteristics has significantly improved since the onset of observations. Baseline improvements have been incremental, but significant. The requirements on the GBT hardware are stringent, as in all radio astronomy systems, particularly due to the relatively high intermediate frequencies and broad bandwidths used, and the system complexity caused by the need to support multiple backends and multiple simultaneous spectral observations.

The frequency structure in receiver noise which has a serious impact on continuum source observations requires more research until the causes are well understood. However, in the meantime there is promise in improvements to observing and analysis procedures.

The understanding gained in the course of the baseline investigations could be applied to the design of an "ideal" spectral line receiver. The approach would likely evolve toward a highly integrated design, using quite short transmission lines and a minimum of coaxial interconnections, in an isothermal package. The integration of digital samplers with the microwave front-end should be investigated. It is likely that an improved receiver design would make observations for broad spectral lines much more feasible with the GBT.